Investigation of AuNiGe-based superconducting ohmic contacts and hydrodynamic transport effects in GaAs/AlGaAs-based two-dimensional electron gases

Terje Bjørge Theisen

Supervisor: Dr James Nicholls

Thesis submitted in part fulfilment of the requirement for the degree of Doctor of Philosophy from Royal Holloway, University of London

Declaration of Authorship

I, Terje Bjørge Theisen, hereby declare that this thesis and the work presented in it is entirely my own. Where I have consulted the work of others, this is always clearly stated.

Terje Bjørge Theisen — 01/10/2023

Terje Bjørge Theisen — Date

Acknowledgements

I gratefully acknowledge everyone who has helped make this thesis a reality, and of course the UKRI and Royal Holloway for their support. This PhD has been an incredibly difficult but rewarding experience for me both personally and professionally. I am not the same person that I was before starting this PhD and I feel that it has helped me understand myself better. That being said I feel like I would do myself a disservice if I did not mention COVID; which alongside the subsequent lock-downs made every facet of my life more difficult during its reign.

There are however some people that I would like to thank by name. Firstly a huge thank you goes to my supervisor Dr. James Nicholls, without whom this PhD would never have happened. I am indebted to him for all the time he has spent helping me over the last 4 years in a myriad of ways. I would also like to thank Dr. Aditya Kumar Jain for all the help he has provided whether that is by helping me set up experiments or via discussions. Additionally I would also like to thank Dr. Chris Beauchamp for motivating me to do a PhD in the first place, without his input during the last year of my MSci I would probably never have applied to begin with. Penultimately I would also like to thank my parents for shaping me into the person that I am today and their support. Lastly, but by no means least, I would like to thank my wife Paula for all her support throughout the years and for making me a better person.

Abstract

This thesis describes an investigation of AuNiGe-based ohmic contacts as well as a series of differential resistance and magnetic field measurements performed on GaAs/AlGaAs-based two-dimensional electron gases (2DEGs) alongside all the required background information. The aim of the AuNiGe ohmic contact study was to discover the cause of the superconductivity occurring below 1 K. The result is a list of the most probable superconducting compounds, likely AuAl or AuGe-based but there could be a combination of several compounds. The main compound identified, Au_7Ga_2, is not a superconductor and no other compound was found in sufficient amounts to cause bulk superconductivity. As a result, it is possible that the observed superconductivity could be the result of a percolating network existing throughout the ohmic contact. If true, then a much more granular TEM study is required. The interface between the ohmic contact and the semiconductor was also found to be very inhomogeneous and the existence of the 2DEG below it is questionable.

The differential resistance and magnetic field measurements performed on 2DEG Hall bars of various widths showed that applying a magnetic field to a narrow Hall bar recovers the Bloch-Grüneisen transition observed in wider Hall bars. Without a magnetic field the behaviour is hidden by hydrodynamic effects which only occur in narrow Hall bars due to the interplay between the width of the Hall bar and the electron-electron scattering length. Primary thermometry based on cross-correlated Johnson noise was also performed to establish that the transition was the Bloch Grüneisen transition; with all wide Hall bars measured having a transition temperature in line with the Bloch Grüneisen temperature.

Publications

Levitin LV, van der Vliet H, Theisen T, Dimitriadis S, Lucas M, Corcoles AD, et al. Cooling low-dimensional electron systems into the microkelvin regime. Nature Communications. 2022;13(1):1-8

Contents

List of Figures

List of Tables

Chapter 1

Introduction

1.1 Superconductivity in AuNiGe-based ohmic contacts

The ability to cool down systems to temperatures not naturally observed on Earth is one of the cornerstones of modern condensed matter physics. Low temperatures are responsible for many modern advancements such as the redefinition of current via the electron pump [2]. One popular system used to study different fundamental physical phenomena such as fractional quantum Hall states [3] or Tomonaga-Luttinger liquids [4] is the two dimensional electron gas (2DEG). By lowering the temperature, these phenomena not only become possible, but also cleaner and more robust.

Lowering the temperature comes with new and growing challenges such as the falling heat capacity of the electron [5], but more importantly at around 1 K the electrons and phonons begin to thermally decouple. The rate at which electrons lose their excess energy is given by

$$P = \dot{Q}(T_e) - \dot{Q}(T_L), \tag{1.1}$$

where $\dot{Q}$ is the rate of heat transfer for the electrons or lattice respectively, T_e is the electron temperature and T_L is the lattice temperature. According to Ref. [6] the heat transfer $\dot{Q}(T)$ is given by

$$\dot{Q}(T) = aT^5 - bT^2, \tag{1.2}$$

where the first term is electron-phonon cooling and the second term is cooling via the ohmic contacts. With decreasing temperatures the cooling provided through the ohmic contacts become a greater proportion of the overall cooling provided. Consequently it is important to thermally couple the 2DEG and the source of cooling as strongly as possible by minimising the resistance of the ohmic contacts [7]. However, this model of cooling relies on ohmic contacts being able to cool at these temperatures. It has recently been discovered that this is not the case [1] and that common AuNiGe ohmic contacts [8, 9, 10] based on different types of ohmic recipes experience partial superconductivity below approximately 1 K. This puts constraints on the ability to cool, which in turn puts further constraints on the ability to observe more robust or even new phenomena in these types of systems. As a result, it becomes important to identify the source of the superconductivity in order to find a solution. This thesis will provide proof of the superconductivity and present the results of a transmission electron microscopy (TEM) study on the AuNiGe-based ohmic contacts.

1.2 Electron-phonon interactions and narrow Hall bars

The interaction of electrons and phonons has long been a given in the study of semiconductors and metals; in fact they take up chapters in many books on the subject [11, 12].

However in the last few decades theories have been developed on real two-dimensional systems where the electrons and phonons are decoupled [13]. One of the consequences of electron-phonon (e-ph) decoupling is the jump in current-voltage characteristics in sufficiently disordered systems at low temperature caused by the creation of a bistability in the electron temperature [14]. The bistability consists of hot and cold channels of electrons which briefly coexist in the current voltage characteristics [15].

While some success has been had in experimentally realising e-ph decoupling [16, 17], there has been an emphasis on the requirement of suspended structures in two dimensional electron gases such as InGaAs and AlGaAs [18]. The suspension of the system, usually a Hall bar, is believed to reduce the e-ph coupling by physically separating the Hall bar from the substrate below [19], leading to the creation of standing waves. It has been reported [20] that the suspension of the Hall bar causes an observable difference in the measured thermopower given by

$$S = S_d + S_{ph} = aT + bT^6, \tag{1.3}$$

where S_d is the diffusion thermopower, S_{ph} is the phonon drag thermopower, and a/b are constants. The observed difference, caused by a reduction in S_{ph}, was seen at temperatures as high as 7 K. The high temperature is noteworthy because it means a difference might be observed using a 4.2 K dewar. A drawback of using suspended structures, however, is that it limits the feature size that may be used due the risk of structural collapse [21].

This thesis will show the results of cooling down narrow suspended and non-suspended Hall bars to approximately 1 K and performing differential resistance measurements in order to raise the temperature alongside similar measurements for wider non-suspended Hall bars. It will also develop a cross-correlated Johnson noise thermometry technique in order to calculate the electron temperature. Finally this will lead to some observed differences between suspended and non-suspended narrow Hall bars, but will also reveal the complex interaction of length scales which occur in this regime alongside the Bloch Grüneisen transition.

1.3 Thesis outline

The chapter structure, alongside a brief overview of what each chapter contains, is as follows:

- **2. Two-Dimensional Electron Gases**: Presents the underlying physics and key properties of the GaAs/AlGaAs-based two-dimensional electron gas as well as how these systems are created. Afterwards there is a wafer overview outlining the key properties of all the samples used throughout the thesis. The chapter finishes with sections on transport properties, a basic synopsis of the scattering mechanisms involved, and motivations for the research conducted.

- **3. Electron Microscopy Techniques**: Discusses the main types of microscopy techniques used for the later chapter on the transmission electron microscopy study of AuNiGe-based ohmic contacts.

- **4. Low-temperature experimental techniques**: Provides background on the experimental techniques used, such as four-terminal measurements, and on the equipment used.

- **5. Cross-correlation measurement of electronic noise**: Discusses the types of electronic noise present in semiconductors, what processing techniques were utilised, and how this all came together in order to perform cross-correlation measurements.

- **6. Magnetohydrodynamics**: Investigates and discusses the complex picture of interacting length scales using differential resistance measurements in narrow and wide Hall bars. The chapter then goes on to introduce a magnetic field and cross-correlated noise measurements in order to calculate the electron temperature with an increasing DC current.

- **7. Transmission Electron Microscopy study of AuNiGe-based ohmic contacts**: Shows the results of the study on AuNiGe-based ohmic contacts in both a layered eutectic and a eutectic slug sample which has previously been observed to go superconducting at 1 K. The chapter then goes on to discuss the potential superconductors as well as the health of the two-dimensional electron gas immediately below the bulk of the ohmic contact.

- **8. Conclusion and further work**: Reiterates the main results of the thesis and to what extent the initial aims were accomplished. The chapter finishes with a section on the requirements and ideas for future work on the topics.

Chapter 2

Two-Dimensional Electron Gases

2.1 Introduction

The two-dimensional electron gas (2DEG) is a marvel of modern semiconductor engineering; enabling the creation of incredibly clean systems where novel physics can be studied at two, one, or even zero dimensions [22]. There are many types of 2DEGs, but the only type studied in this thesis is in the GaAs/AlGaAs heterostructure. As a result the aim of this chapter is to describe the GaAs/AlGaAs-based 2DEG. Specifically this chapter explains the key properties of the 2DEG, provides a summary of all the samples used, and reviews the transport properties of these systems.

2.2 GaAs/AlGaAs heterojunctions

GaAs/AlGaAs heterojunctions may on the surface appear similar to thin metallic films, but offer several advantages including higher mobility and an easily adjustable carrier density, either through doping or applying an electric field. The density of these heterojunctions remains much lower than that of metals, but this is actually an advantage as the Fermi wavelength can be comparable to the fabricated structures, allowing the study of ballistic [23], quasi ballistic [24], and diffusive transport regimes [25].

Formally electron transport in a system is considered two-dimensional when the motion of the electrons is restricted in the third direction by a potential barrier. In order to quantise this motion the confining potential must have a width of approximately the de Broglie wavelength $\lambda = h/p$, where h is Planck's constant and p is the momentum. To confine electrons in one or more directions the kinetic energy of the electrons needs to be less than the confining potential energy, which is accomplished using Molecular Beam Epitaxy (MBE).

The conduction in these semiconductors can be understood in terms of the Drude model. At these low temperatures all the conducting electrons are very close to the Fermi energy E_F, resulting in the de Broglie wavelength being determined by electrons of momentum $k_F = \sqrt{2\pi n}$, where n is the carrier concentration in two dimensions, therefore

$$\lambda_F = \sqrt{\frac{2\pi}{n}}. \tag{2.1}$$

Using typical values, which are typically in the order of 10^{11} cm^{-2} for the carrier concentration the de Broglie wavelength for a GaAs/AlGaAs heterojunction is approximately $\lambda \sim 10$ nm [26].

2.3 Growth

GaAs/AlGaAs heterostructures are grown using molecular beam epitaxy, which is capable of growing these systems with atomic layer precision [27], enabling the engineering of band structure. A schematic of an MBE chamber is shown in Fig. 2.1. In order to grow these crystals the starting point is an ultra-pure GaAs crystal mounted on a rotating heated substrate holder in an ultra high vacuum chamber, typically at $10^{-10} - 10^{-12}$ Torr [28]. As a result the deposition of material, due to effusion of Si, Al, Ga, As, and Al from Knudsen cells, occurs in the ballistic regime ensuring a uniform distribution. In order to accurately measure and control this deposition the Knudsen cells are controlled using shutters and heaters, and the layers grown are measured in situ using reflection high energy electron diffraction (RHEED).

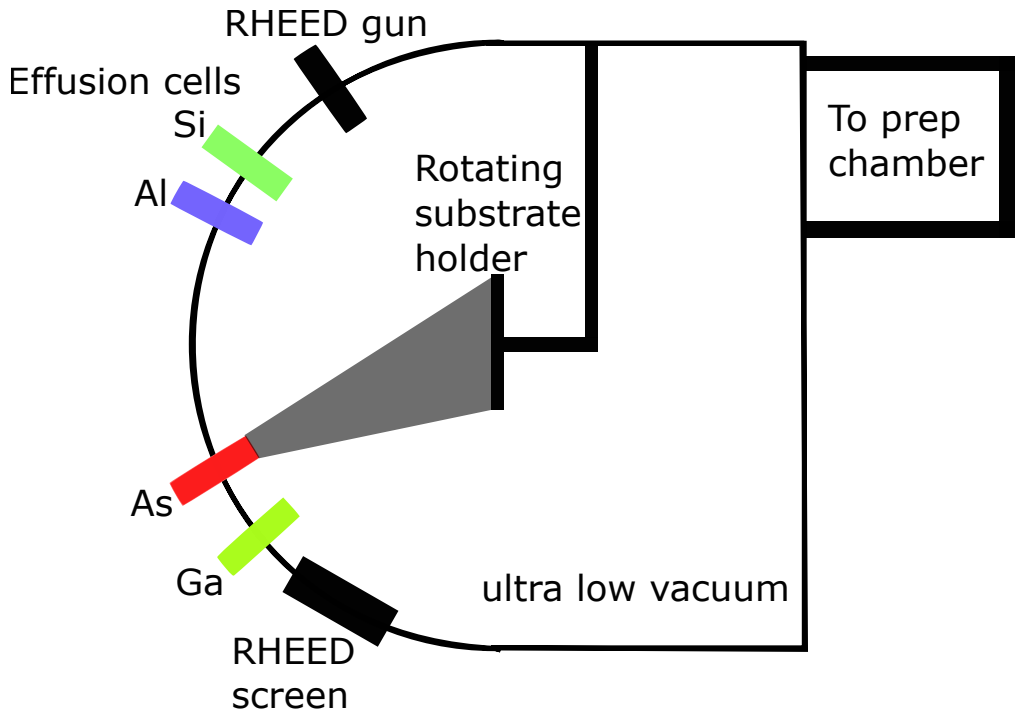

Figure 2.1: Schematic of a molecular beam epitaxy chamber used for growing GaAs/AlGaAs 2DEGs; starting with clean GaAs substrate aligned in the (001) direction. The GaAs substrate is mounted on the rotating substrate holder, which ensures uniform deposition. The different effusion cells, in this case Si, Al, As, and Ga, are then applied in various combinations by heating the cells. The deposition combined with the $10^{-10} - 10^{-12}$ Torr pressure creates a ballistic beam aimed towards the substrate, which is then regulated using high speed shutters, and monitored using RHEED to ensure atomic layer precision.

2.4 Modulation doping & persistent photoconductivity

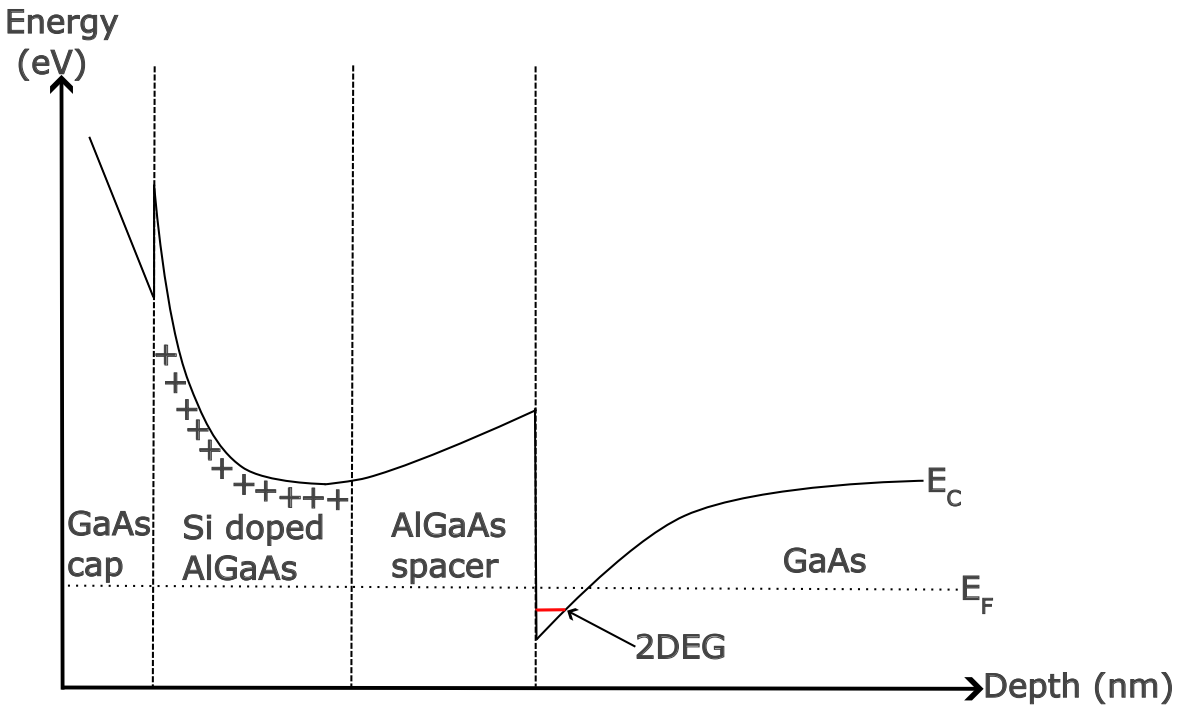

Figure 2.2: Conduction band profile of a GaAs/AlGaAs 2DEG consisting of four different layers going from the top surface of the wafer to the bottom. The first layer is a GaAs cap layer which is there to protect the layers below. The next layer is the Si doped AlGaAs layer, which has a positive net charge due to the donation of its excess electrons. The doping causes curvature which decreases the conduction band and depending on the extent of the doping the conduction layer can go below the Fermi energy E_F causing another 2DEG to be created. The next layer is an undoped AlGaAs spacer layer whose purpose is to keep the Si doped layer and the GaAs layer separated and provide a sharp edge on the conduction band by increasing it. Finally there is the GaAs layer; the sudden change from the AlGaAs layer to the GaAs layer causes a sharp drop in the conduction band below E_F, creating an approximately triangular potential well [29].

GaAs/AlGaAs crystals have very little strain and few dislocations due to GaAs and AlAs having very similar lattice parameters, 565.6 and 566.17 pm respectively [30, 31]. Lattice matching is very useful in this case as the band-gap of GaAs and AlGaAs are different [32]; enabling band-gap engineering, where by randomly replacing some of the Ga atoms with Al the band-gap is modified. Defining x as the fraction of Ga atoms replaced with Al the resulting band-gap at room temperature is given by [33]

$$E_g(Al_xGa_{1-x}As) = (1.424 + 1.247x)\ eV; \tag{2.2}$$

in this thesis x = 0.33. As a result of the close lattice matching it is possible to create clean interfaces between AlGaAs and GaAs without creating significant scattering sources. At the same time, due to the shifted band offsets in AlGaAs, this interface creates a quantum well where electrons and holes are trapped in the z direction as shown in Fig 2.2.

In order to provide the electron density, modulation doping, in the form of adding Si to the top AlGaAs layer as shown in Fig. 2.3, is introduced. The n-type dopant provides additional electrons, which are mostly trapped in the quantum well. However not all dopants are ionised, leaving their extra electron stuck in DX centres [34]. At low temperatures the thermal energy of the system is insufficient to excite the electrons. In order to overcome the potential barrier the confined electrons need energy equivalent to the band-gap, which in this case is 1.834 eV corresponding to a wavelength λ of 676 nm [35]. By shining an LED of this wavelength or shorter the confined electrons are excited sufficiently to escape the DX centres and reach the heterojunction, increasing the electron density of the 2DEG [36]. This phenomenon is known as persistent photoconductivity, or 'illumination' as this increased density is persistent until the sample is thermally cycled. Experimentally full illumination is realised by driving a voltage through the LED corresponding to a current between 10 and 50 mA until the measured resistivity reaches equilibrium. The time taken to reach full illumination varies depending on the system, for example if the Hall bar is covered with a thin gate it can take minutes, but usually only takes a few seconds. The intensity of illumination can be fine tuned by limiting the driving voltage on the LED and the duration of illumination, allowing the mobility and density to be controlled. In order to do so the current is kept below 0.1 mA and the duration of illumination between 100 and 300 ms, however the exact parameters depend on how many intermediate stages of illumination are required.

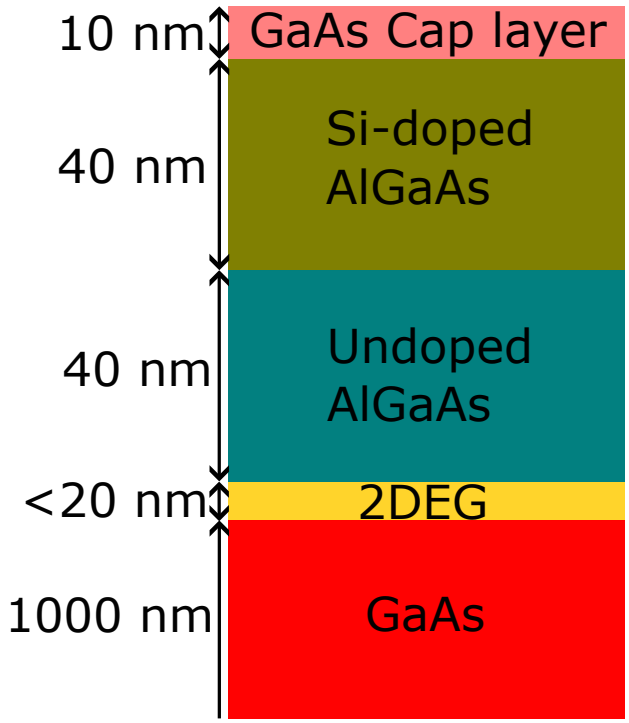

Figure 2.3: MBE-grown GaAs/AlGaAs heterojunction showing typical values for all the layers. The 2DEG is created between the undoped AlGaAs spacer and the GaAs by the sharp drop in the conduction band below the Fermi energy E_F which occurs at this interface. The exact width of the layer below E_F varies but needs to be less than 20 nm.

2.5 2DEG chip overview

The following table contains an overview of all the different chips used throughout the thesis. There are a couple of aspects worth noting. First of all, I have not taken all the data seen here myself, some have been provided by others working on the same grant, mainly Dr Stuart Holmes as shown in bold. Secondly, dark numbers can be unreliable and vary from cooldown to cooldown so there can be inconsistencies between the numbers seen here and ones stated later. In some cases values were not used in any way and have therefore not been recorded/ stated in Table 2.1 below.

Wafer	Chip num	width μm	μ dark $\times 10^6 \frac{cm^2}{Vs}$	n dark $\times 10^{11} cm^{-2}$	μ illum. $\times 10^6 \frac{cm^2}{Vs}$	n illum. $\times 10^{11} cm^{-2}$	Depth (nm)	Special feature	Abbr. name
W1501	1	10	**0.05**	**1.2**	1.8	3.4	90		N1
W1501	2	10	**0.03**	**1.6**	2.0	3.3	90	suspended	S1
W1501	3	10	**0.07**	**1.4**	1.7	3.3	90		N2
W1501	4	10	**0.52**	**1.1**	1.9	3.3	90	suspended	S2
W1501	*	80	1.65	1.28	3.7	3.4	90	assessment	A1
T636	12	80			2.0 (0.25)	3.8 (3.7)	90	(Ion damage)	D1
T636	13	80			2.4 (0.19)	3.8(3.5)	90	(Ion damage)	D2
T636	15	80			2.0 (0.13)	3.8(3.4)	90	(Ion damage)	D3

Table 2.1: Sample overview with key properties and features. Note that for the ion-beam-damaged devices the μ and n in brackets are for the ion-beam damaged regions. The W1501 wafer was grown by Dr Chong Chen. The T636 wafer was grown by Dr MY Simmons. All chips were fabricated by Dr Stuart Holmes, who also provided the data in bold.

2.6 Transport properties

The aim of this section is to better understand electron transport in the two-dimensional electron gas beginning with how electrons are confined in one of three dimensions, how some of the key parameters are defined, and finally the effect of perpendicular magnetic fields.

2.6.1 Electron Confinement

The main characteristic of a 2DEG is unsurprisingly that it is two-dimensional, which is useful for a variety of reasons, one being the reduced complexity of having fewer dimensions. In order to understand how a 2DEG is 2D consider a 3D hard-walled box with volume $V = L_x L_y L_z$ of non-interacting electrons given by the 3D time-independent Schrödinger equation

$$E\Psi(x,y,z) = \left(-\frac{\hbar^2}{2m}\nabla^2 + V(x,y,z)\right)\Psi(x,y,z), \tag{2.3}$$

where ∇^2 is the Laplacian operator, $\Psi(x,y,z)$ is the wave function, and $V(x,y,z)$ is the potential within the box, which can in this case be written as $V(x,y,z) = V_x(x) + V_y(y) + V_z(z)$. In order to solve this, separation of variables is employed by substituting in $\Psi(x,y,z) = X(x)Y(y)Z(z)$ and dividing by $X(x)Y(y)Z(z)$, giving

$$\frac{1}{X}\frac{d^2X}{dx^2} + \frac{1}{Y}\frac{d^2Y}{dy^2} + \frac{1}{Z}\frac{d^2Z}{dz^2} = \frac{-2mE}{\hbar^2}, \tag{2.4}$$

where each term must be equal to a constant, e.g. $\frac{1}{X}\frac{d^2X}{dx^2} = -{k_x}^2$ and $X = e^{ik_x x}$. The method is equivalent in the other two dimensions. The final equations for a 3D system is then

$$E = \frac{\hbar^2}{2m^*}(k_x^2 + k_y^2 + k_z^2), \tag{2.5}$$

where

$$m^* = 0.067m_e, \tag{2.6}$$

the effective electron mass in GaAs[37], given in terms of the rest mass of the electron m_e, and

$$\Psi(r) = \frac{1}{\sqrt[3]{V}}e^{i\vec{k}\vec{r}}, \tag{2.7}$$

where $\vec{r} = (x,y,z)$ and $\vec{k} = (k_x, k_y, k_z)$. The system then becomes 2D as long as the energy levels in the z potential are widely separated causing electrons to be confined, regardless of

the exact shape of the potential. When this is the case then the equation for the energy can be simplified to

$$E_{n,k} = E_n + \frac{\hbar^2}{2m^*}(k_x^2 + k_y^2), \tag{2.8}$$

where $E_n = \frac{{n_z}^2\pi^2}{{L_z}^2}$ is the quantised energy in the confined direction, in this case the z direction. For each of these quantised energy levels there will be a near continuum of associated free states for the electron in the xy plane.

2.6.2 Density of States

Electron occupation in any system follows the Pauli exclusion principle, which states that two or more identical particles with half integer spin cannot occupy the same state. Due to spin degeneracy of 2, this means that two electrons can occupy every k state. As the number of electrons in a system increases then so does the total energy $E = \frac{\hbar^2\vec{k}^2}{2m}$. In $\vec{k}$-space the quantised states can be represented as a grid of dots, each of which can hold two electrons. For a 2D system of N electrons this means that a circle up to a radius, k_F, is occupied by electrons. If the separation of each point on this grid is given by $\frac{2\pi}{L}$ then the total number of electrons in the system can then be given by

$$N = \frac{2\pi {k_F}^2}{(2\pi/L)^2}, \tag{2.9}$$

where k_F is known as the Fermi wavevector, and relating the electron density n to the total number of electrons via $n = N/L^2$ gives the Fermi wavevector as

$$k_F = \sqrt{2\pi n}. \tag{2.10}$$

The importance of k_F cannot be understated, as it is only the electrons near the edge of the Fermi circle (or sphere in 3D) that contribute to the system, as all the lower states are trapped. Together with the density of states $g(E)$, which is defined as the number of available states per unit energy per unit volume, the physical properties of any metal is determined [11]. Mathematically the density of states is given by

$$g(E) = \frac{dn}{dE}, \tag{2.11}$$

which can be rewritten as

$$g(E) = \frac{dn}{dk} \times \frac{dk}{dE}. \tag{2.12}$$

In 2D at $k = k_F$, $\frac{dn}{dk} = \frac{k}{\pi}$ and $\frac{dE}{dk} = \frac{\hbar^2 k}{m^*}$, which simplifies the equation to

$$g(E) = \frac{m^*}{\pi\hbar^2}, \tag{2.13}$$

which, as shown in Fig. 2.4, is independent of k_F, a result which is unique for 2D systems.

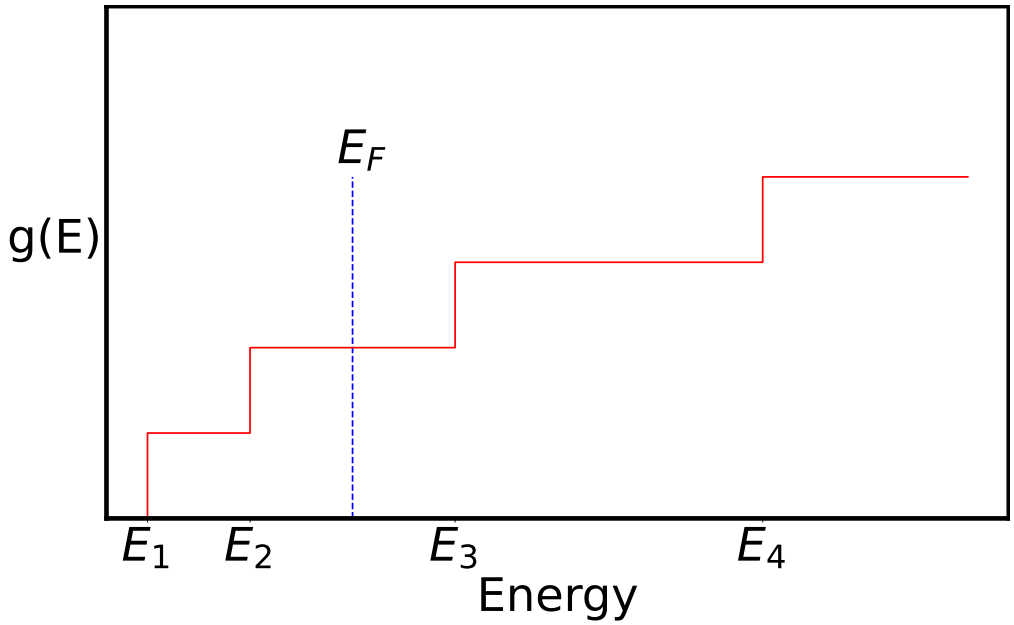

Figure 2.4: Density of states for a 2D system as a function of energy. E_i are the different energy bands with each step referred to as a 'subband'. If the Fermi energy E_F is between E_2 and E_3 then the two lowest subbands are occupied.

2.6.3 Drude Transport

The transport of electrons through a metal can be described using the Drude model. Since applying a voltage is the same as applying an electric field $\vec{E}$ then from Newton's second law

$$F = ma, \tag{2.14}$$

where the applied force is $\vec{E}e$, the mass is given by m^*, and the acceleration can be considered the average drift velocity $\vec{v}_d$ divided by the mean free time between momentum-relaxing collisions in the metal τ_{mr}, then mathematically

$$\vec{E}e = m^* \frac{\vec{v}_d}{\tau_{mr}}. \tag{2.15}$$

This equation can then easily be rearranged and we can define the mobility μ as the coefficient between the drift velocity $\vec{v_d}$ and the applied electric field

$$\vec{v}_d = \frac{e\tau_{mr}}{m^*}\vec{E} = \mu\vec{E}. \tag{2.16}$$

Note that the drift velocity is the collective average velocity caused by the applied electric field and does not replace the individual velocity of the electrons which for the conducting electrons will remain approximately v_F. However τ_{mr} combined with v_F can be used to calculate the mean free path l_{mfp} of the system using

$$l_{mfp} = \tau_{mr} \times v_F, \tag{2.17}$$

which is important because in any system the shortest length scale will determine whether the regime is ballistic or diffusive. So for example if the mean free path is less than the physical dimensions of the system then it will be in a diffusive regime.

In zero magnetic field the current density is given by

$$\vec{J} = ne\vec{v}_d = \frac{ne^2\tau_{mr}}{m^*}\vec{E} = \sigma\vec{E}, \tag{2.18}$$

where σ is the Drude conductivity and σ and μ are related via

$$\sigma = ne\mu. \tag{2.19}$$

Experimentally μ and n are considered the key properties of a 2DEG, and are quoted in research publications.

2.6.4 Transport in a Magnetic Field

When a magnetic field is applied perpendicular to a conductor a voltage will be measured transversely to the direction of the electric current; this phenomenon is known as the Hall effect and is a result of the Lorentz force which is given by

$$\vec{F} = q(\vec{E} + \vec{v} \times \vec{B}), \tag{2.20}$$

where q is the charge of the charge carrier, $\vec{E}$ is the electric field, $\vec{v}$ is the velocity of the charge carrier, and $\vec{B}$ is the applied magnetic field. In most cases q will be the electron charge e. For simplicity, consider a two-dimensional system; due to the Lorentz force, charge carriers

get pushed to one side of the conductor, generating a Hall voltage as they travel along, which produces a force in the opposite direction, until an equilibrium is reached. This is shown in Fig. 2.5.

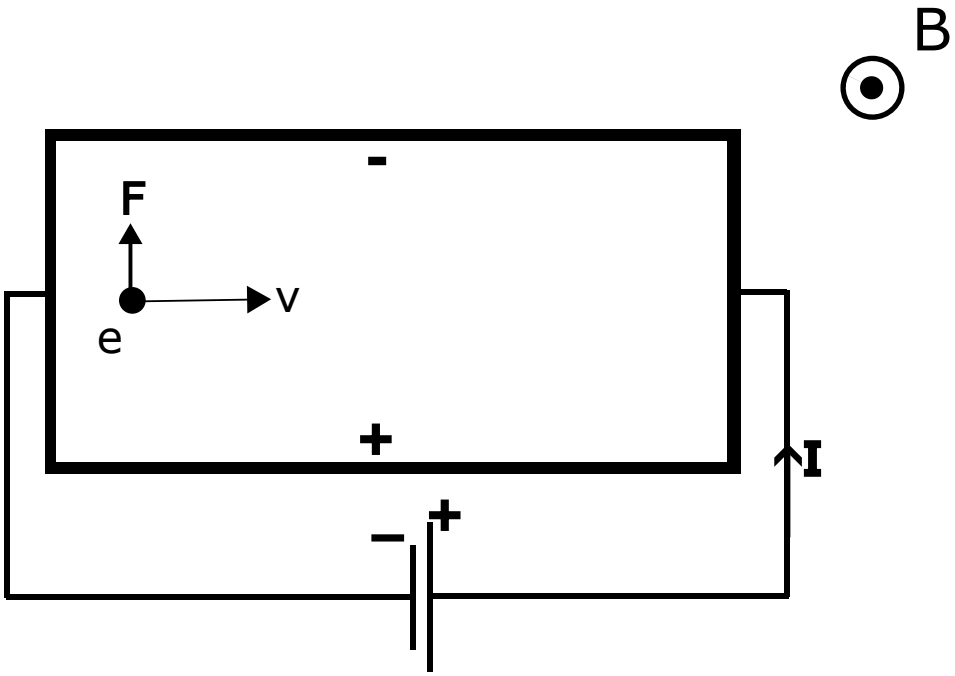

Figure 2.5: 2D Hall effect sketch showing how charge carriers get pushed by the Lorentz force to one side in a conductor by a perpendicular magnetic field, generating a voltage transverse to the direction of the current $\vec{I}$ and magnetic field $\vec{B}$. This voltage is inversely proportional to the density of charge carriers, electrons in this case, and provides a way of measuring the carrier density n and the mobility μ.

At equilibrium, the net force is zero, meaning that $E = |\vec{E}| = |\vec{v} \times \vec{B}|$. Assuming a uniform electric field then $E = V_H/w$ where V_H is the Hall voltage and w is the width of the system, therefore $V_H = vwB$. In addition, the total current will be given by $I = |\vec{I}| = nw|\vec{v}|q$, where n is the carrier density. Combining these results and simplifying gives

$$V_H = \frac{BI}{nq}, \tag{2.21}$$

where all quantities are either measured in the experiment or are known constants. This result gives a quick and easy way of calculating the density in the system and can be combined with resistance measurements in order to extract the mobility using

$$\mu = \frac{1}{ne\rho}, \tag{2.22}$$

where $\rho = \frac{1}{\sigma}$ is the resistivity of the conductor when the voltage is measured in the same direction as the current.

2.7 Scattering Mechanisms

There are a variety of scattering mechanisms that occur in a 2DEG. The following section will outline the main scattering mechanisms that are relevant for this thesis. The most important characteristic of any scattering mechanism is whether or not it conserves momentum in the direction of the applied current, as this affects the resistance of the conductor. A momentum conserving scattering event by itself does not modify the measured resistance, whereas a non-momentum conserving collision does.

2.7.1 Boundary roughness

Boundary roughness scattering is the scattering between electrons and the boundary of the 2DEG. The boundary roughness of a 2DEG can vary greatly depending on the fabrication; the smoother the boundary the higher the percentage of momentum-conserving collisions. In the literature there are two main ways of quantifying this using either the percentage of momentum conserving collisions, often referred to as 'p', or the 'slip length', which is the distance travelled by an electron between non-momentum-conserving boundary scattering events. These two nomenclatures are equivalent, but we will use the % of momentum conserving collisions in this thesis. A simple sketch illustrating the difference between a smooth and a rough boundary is shown in Fig. 2.6. For this type of scattering to be significant in a conductor the width of the Hall bar must be comparable to the other length scales in the system, such as the electron-phonon scattering length l_{e-ph} or the electron-electron scattering length l_{ee} [38].

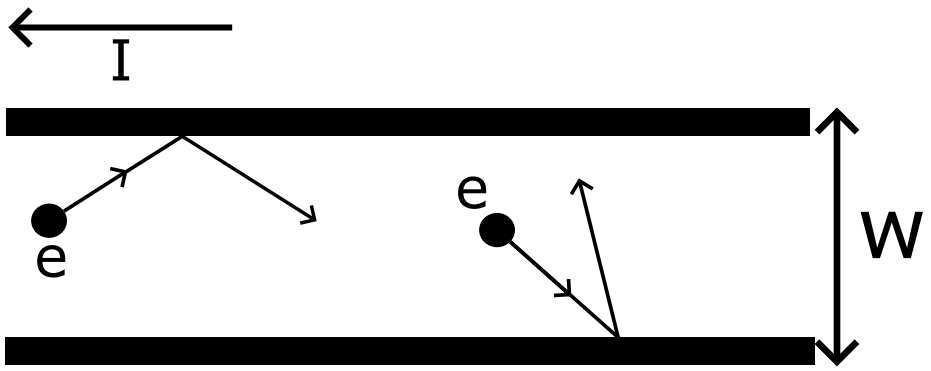

Figure 2.6: Schematic showing the effect of boundary roughness on an electron-boundary scattering event in a 2DEG Hall bar of width w when a current I is applied. As shown on the left the electron could potentially bounce off the boundary conserving its momentum in the direction of the current. Alternatively, as shown on the right, the electron could bounce off the boundary and not conserve momentum in the direction of the current, contributing to the resistance.

2.7.2 Electron-Phonon scattering

The behaviour of the scattering between electrons and phonons can vary greatly depending on the temperature and has been covered in great depth elsewhere [39], but can roughly be divided into three different regimes: the Bloch-Grüneisen regime, the equipartition regime, and the inelastic regime. Electron momentum is not conserved in any of these regimes. The Bloch-Grüneisen regime is dominated by piezoelectric coupling, where $\rho \propto T^5$, resulting in a rapid increase in the resistance as a function of temperature. Piezoelectric coupling is a type of acoustic phonon scattering caused by the macroscopic polarization caused by strain [40]. The transition from the Bloch-Grüneisen regime to the equipartition regime is defined as the Bloch-Grüneisen temperature, which is given by

$$k_B T_{BG} = 2k_F \hbar c_s, \tag{2.23}$$

where T_{BG} is the Bloch-Grüneisen temperature and c_s is the speed of sound. This transition can be understood by considering the restrictions of the possible phonon energies, illustrated in Fig. 2.7. At low temperatures the energy of a phonon is given by $\hbar c_s k$, where k is the wavevector of the phonon. This characteristic energy can be associated with a temperature by setting the expression equal to $k_B T$. Because conducting electrons are near the Fermi surface the result of an electron-phonon scattering event is that the electron will move somewhere

else near the Fermi surface within k_BT. As a result, the change in the wavevector of the electrons at low temperatures can only take on values from 0 to $2k_F$. The temperature at which phonons can produce a change in the electron wavevector of $2k_F$ is defined as the Bloch-Grüneisen temperature, which gives rise to Eq. 2.23. Below this temperature these relatively higher energy phonons are not emitted/absorbed, leading to a significant decrease in the measured resistance.

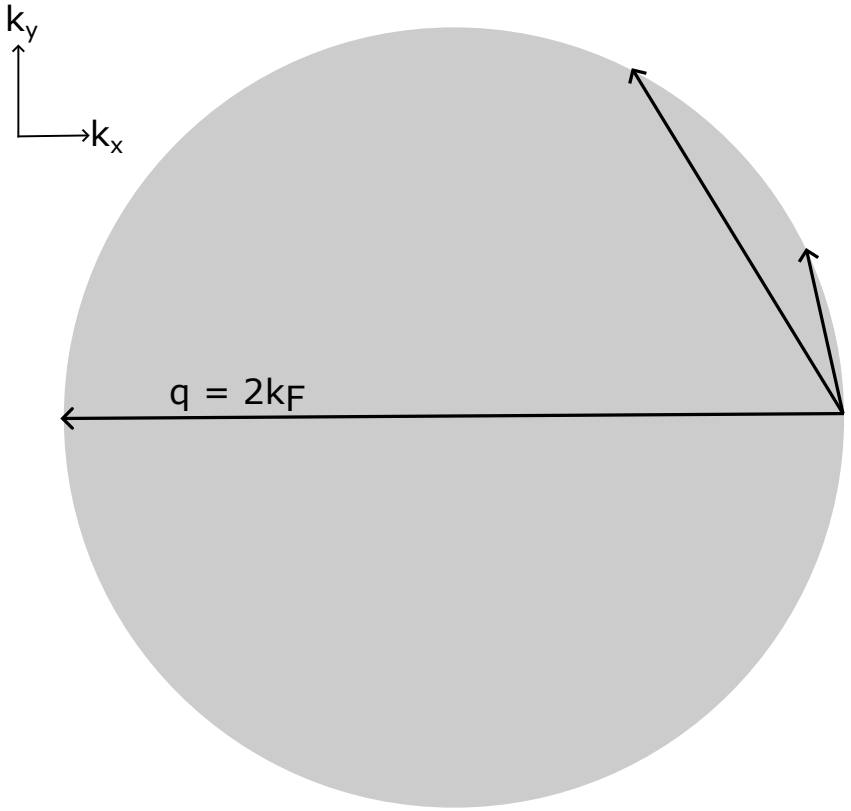

Figure 2.7: Sketch of the Bloch-Grüneisen phase limitation. The solid grey circle is the Fermi circle in 2D and the different arrows represent different possible scattering scenarios along the Fermi surface. A temperature corresponding to a phonon wavevector of much less than $2k_F$ means that electrons will be unable to scatter to the opposite side of the Fermi circle and will instead be limited to lower momentum scattering, which cause a smaller change in the overall momentum of the electron. This manifests itself as a steep rise in the resistance as the temperature is increased and approaches the Bloch-Grüneisen temperature T_{BG}.

The equipartition regime, at energies below the optical phonon energy 36 meV [41], typically corresponding to temperatures below 40 K, is characterised by electrons scattered via deformation-potential, which is the strain effect on the band structure, and piezoelectric coupled acoustic phonons. The typical phonon energies in this regime are smaller than k_BT

resulting in scattering events being quasi-elastic. Subsequently the resistance will only see a modest increase in this regime as a function of temperature.

The inelastic regime, at energies above 36 meV [41], is characterised by the onset of longitudinal optical phonons. These are high energy phonons which are a significant source of inelastic scattering and as a result the resistance starts increasing rapidly in this regime. The main highlight of this regime is the validity of the Wiedemann-Franz law, which relates the thermal conductivity

$$\kappa = \frac{\pi^2 n k_B^2 T \tau_\kappa}{3m} \tag{2.24}$$

and the electrical conductivity

$$\sigma = \frac{n e^2 \tau_{mr}}{m}, \tag{2.25}$$

defining the ratio of κ to σ of a given material to be proportional to the temperature

$$\frac{\kappa}{\sigma} = \frac{\pi^2 k_B^2 T \tau_\kappa}{3e^2 \tau_{mr}} = L_0 T, \tag{2.26}$$

where e is the electron charge, m is the mass, k_B is the Boltzmann constant, n is the carrier density, L_0 is the Lorentz number, T is the temperature, and τ_κ is the associated scattering timescale for thermal conductivity.

2.7.3 Electron-Electron scattering

There are two types of electron-electron scattering that may occur in a GaAs-based 2DEG: normal scattering and Umklapp scattering. A full treatment of the possible electron - electron scattering mechanisms can be found in Chapter 4.6 of Ref. [12], which gives two key results: the resulting change in momentum can either be $k_1 + k_2 - k_1' - k_2' = 0$ for normal scattering or $k_1 + k_2 - k_1' - k_2' = g$ for Umklapp scattering, where k_n are the initial electron states, k_n' are the final electron states, and g is a reciprocal lattice vector. The first equation states that momentum is conserved, whereas the second one is momentum-relaxing, allowing electrons to lose momentum to the lattice. For the samples investigated in this thesis, due to the low density and perfectly circular Fermi surface, the Umklapp scattering is negligible [42]. As a result, the scattering of electrons can largely be considered analogous to the classical transport of gas particles. The time τ_{ee} between electron-electron scattering events when $k_B T \ll E_F$ is given by

$$\frac{1}{\tau_{ee}} = -\frac{E_F}{2\pi\hbar}\left(\frac{k_B T}{E_F}\right)^2 \left(\ln\left(\frac{k_B T}{E_F}\right) - \ln\left(\frac{q_{TF}}{p_F}\right) - \ln 2 - 1\right), \tag{2.27}$$

where q_{TF} is the Thomas-Fermi screening wavevector in 2D given by $2me^2/\hbar^2$, and p_F is the Fermi momentum [43]. Note that there is some debate as to the exact prefactor of the equation [44, 45, 46]. In this thesis the original equation by Ref. [43] was used, a decision which will be revisited in Chapter 6.

2.8 Hydrodynamics

The aim of this section is to provide the necessary background information to understand the state of the existing research in electron hydrodynamics, which was originally predicted by Gurzhi in 1963 [47]. It was argued that as the temperature increased, the electron-electron (e-e) scattering length would decrease, reducing the resistance, as e-e scattering events in GaAs/AlGaAs are momentum-conserving. However it would not be until 1994 that L. W. Molenkamp and M. J. M. de Jong [42, 48] would first observe these effects, see Fig. 2.8, in a GaAs/AlGaAs-based two-dimensional electron gas, contributing their observations to the interplay between the enhanced e-e scattering rates caused by a DC current I_{DC} and the momentum-relaxing behaviour of boundary scattering. These findings would then be reinforced by Chabasseur-Molyneux *et al.* [49], who also concluded that the minima observed after the negative differential resistance could be attributed to the e-e scattering length becoming comparable to the mean free path, leading to an increasing resistance.

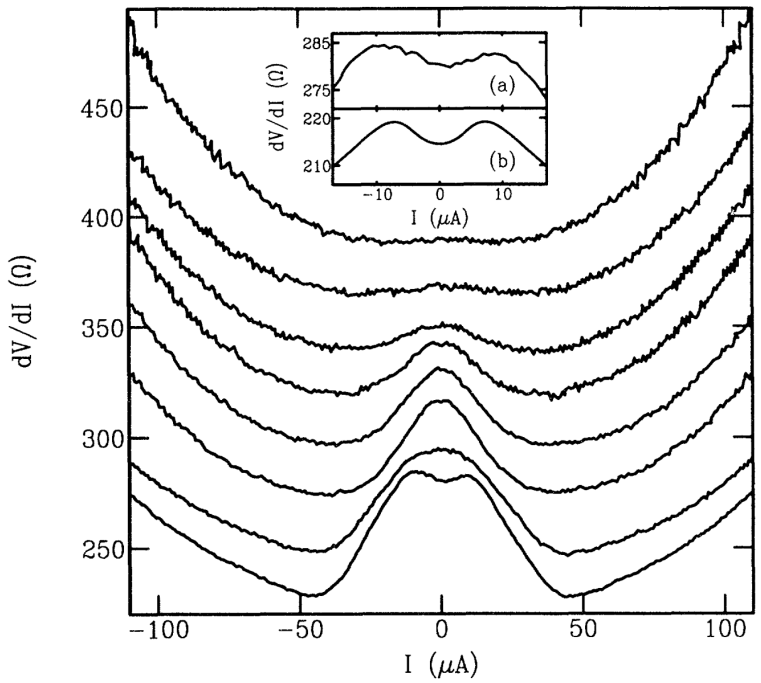

Figure 2.8: Original hydrodynamic effect observed in de Jong and Molenkamp for a Hall bar width of 3.5 μm at various lattice temperatures. From top to bottom the lattice temperatures are 24.7, 20.4, 17.3, 13.6, 10.4, 8.7, 4.4, and 1.5 K. At 1.5 K the density is 2.2×10^{11} cm^{-2} and the mobility is 1.6×10^{6} cm^2/Vs. As the temperature decreases, the hydrodynamic regime develops and becomes more robust. At the lowest temperature a ballistic regime is also observed as an increase in the resistance at low currents. At all temperatures after the onset of the hydrodynamic regime the resistance starts increasing, which can be attributed to the increase in electron-phonon scattering. The inset shows (a) a magnification of the T = 1.5 K results compared with the (b) theoretical predictions. From de Jong and Molenkamp [48].

At the same time as this is happening, the effects of applying a magnetic field to narrow Hall bars was also being investigated [50], showing an anomalous magnetoresistance peak at low magnetic field. This peak can be attributed to the enhanced boundary scattering caused by the low magnetic field, as shown in Fig. 2.9, and it is observed that by applying a sufficiently strong magnetic field the resistivity of the narrow Hall bar recovers its bulk value.

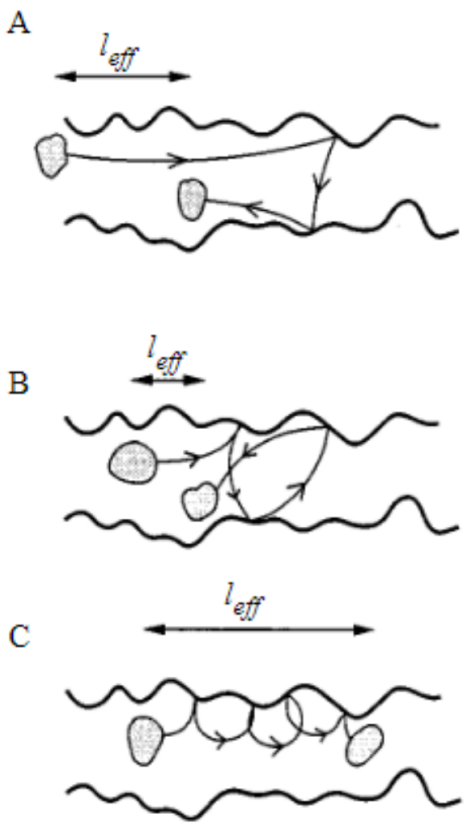

Figure 2.9: Sketch of boundary interactions from Thornton. (A) When the cyclotron radius is significantly greater than the width of the Hall bar the magnetic field pushes the electrons into the Hall bar boundary, enhancing the momentum relaxing boundary interactions leading to an increased resistance. (B) When the cyclotron radius is roughly equal to twice the width of the Hall bar then the resistance reaches a maximum. (C) As the cyclotron radius becomes significantly shorter than the width of the Hall bar then only the states near the edge of the Hall bar will interact with the boundary and the diffusive backscattering is suppressed. From T. J. Thornton [38].

The field has seen a resurgence since the mid 2010's, developing a model for the negative magnetoresistance in viscous flow [51, 52] allowing for the calculation of viscosity coefficients as a function of the applied magnetic field and temperature. A few papers quickly follow by Gusev *et al.* [53, 54] illustrating several hydrodynamic effects such as the resistivity being inversely proportional to the square of the temperature and the square of the sample width. Then in 2021 Keser *et al.* [55] experimentally introduced a perfectly smooth boundary to the system, removing the interaction between e-e scattering and the boundary scattering, proving that the interactions between the e-e scattering and the boundary scattering caused the negative differential resistance observed in the case of current heating and the application of a magnetic field. Finally in one of the latest developments at the time of writing, theoretical

developments have been made on the hydrodynamics-induced violation of the Wiedemann Franz Law in bulk GaAs/AlGaAs and an updated formula for the e-e scattering length as a function of temperature [56]. These developments are of interest since the hydrodynamic effects have so far only been observed in systems with transport features such as narrow channels and not in bulk systems.

2.9 Ohmic-contact structure

The ohmic contacts act as the bridge between the semiconductor and the instruments used to measure it. As mentioned in the introduction, the main method of cooling a semiconductor at low temperature is through the ohmic contacts. Therefore understanding this vital link and their structure is very important. The aim of this section is to provide the background and context required to put the results of Chapter 7 on the structural study of ohmic contacts into perspective.

The structural composition of the AuNiGe based ohmic contacts on GaAs/AlGaAs-based two-dimensional electron gases have been studied since their inception in 1967 by Braslau *et al.* [57]. Previously Gunn had discovered that by including 12 % Ge together with 88 % Au, the melting point of the ohmic contact would decrease from 1063 to 356 °C, forming low-resistance ohmic contacts [58]. The problem with these contacts however was that they had a rough surface morphology with an uneven vertical diffusion into GaAs [59]. It was found that rapid annealing of Au, Ge, and Ni at 450-480 °C for 45 seconds was able to reliably create ohmic contacts with an improved surface morphology [57], but the exact mechanism was not well understood. This would change as a result of various electron-microscope studies such as Ref. [60, 61] which investigated the annealing process at various annealing temperatures, annealing times, and layers of AuGe/Ni/Au. The main phases identified were Au(Ga, As), NiGe(Ga, As), and Ni_2GeAs. It was believed that the existence of a Ni_2GeAs/ GaAs interface was the cause of the low resistivity observed at medium annealing times. Studies such as Ref. [62, 9] saw similar results despite the altered ohmic recipes. The main difference between these studies is that they identified the Au-based compound to be β-AuGa instead of Au with small amounts of Ga and As.

Later studies such as Ref. [63] investigated the impact of varying the Ni content and found that an increasing Ni content increased the amount of GaAs consumed during the annealing process. This study also identified the main Au phase to be Au_4Ga, disagreeing with the previous studies. Even more recently in one of the most comprehensive and modern studies done, see Ref. [64], all the previously mentioned phases were found. However, it is worth noting that none of these studies found Al in the ohmic contact. Some studies mention the GaAs layer being eaten away, which would suggest Al being released as well, but it was never detected. Ref. [65] did find Al on top of the ohmic contacts, but this was a AuGe-based ohmic contact.

Finally it was discovered recently that cooling these contacts down to 1 K caused them to go superconducting [66], but that this was only in parts of the ohmic contact since it was

still able to cool the electrons down to 1 mK [1].

Paper	Temp (°C)	Time (s)	Initial composition (nm, wt%)	Main Phases
Braslau [57]	450-480	45	115 mg AuGe, 5 mg Ni	
Kuan [61]	490	90/ 115/ 200	100 AuGe 20 Ni, 50 Au	Au(Ga, As) Ni_2GeAs NiGe(Ga, As)
Murakami [62]	300-700	various (120)	0/ 5/ 10 Ni 100 AuGe, 35 Ni, 50 Au	β-AuGa, α-AuGa NiAs(Ge), NiGe
Shih [9]	440	120	Au, Ni, AuGe, 0/5 Ni	β-AuGa, NiAs(Ge)
Lumpkin [63]	420	Not stated	150 (5.7 % Ni or 19.5 % Ni rest AuGe)	Au_4Ga, NiGe Ni_2GeAs
Baranska [64]	400-440	30/ 90/ 120	5 Ni, 100 AuGe, 35 Ni 300 Au, 225 AuGe 45/56/60/70 Ni, 300 Au	Poly-Au, β-AuGa NiAs(Ge), Au NiAs(Ge, Au)
Christou [65]	410/ 425/ 450	60	115 AuGe 400 Au	Only looked for Al
Beauchamp [66] (V834 only)	430	80	130 AuGe 50 Ni, 164 Au	

Table 2.2: Annealing conditions and the main phases observed for various ohmic contacts. Note that unless otherwise mentioned all percentages are by weight, all thicknesses in initial composition are in nm, and Au-Ge has a 88 % - 12 % composition. The layers in the initial composition go from top to bottom, meaning that the last layer mentioned is the one directly in contact with GaAs. α-AuGa is just Au with some Ga absorbed into it, but with no alteration to the crystalline structure. β-AuGa is equivalent to Au_4Ga. In general a lot of the same phases are observed despite the wide range of temperatures and annealing times used. The annealing conditions of the samples used in this thesis are also very comparable with the ones from previous studies.

Chapter 3

Electron Microscopy Techniques

3.1 Introduction

The ohmic contact is the bridge between the semiconductor and the outside world, allowing meaningful measurements to be carried out and for the semiconductor to be cooled. As a result, the resistance of these ohmic contacts is very important and the superconductivity that has been observed [1] is significant, as it can dramatically reduce the ohmic contacts ability to cool the semiconductor. The aim of this chapter is to introduce and describe the microscopy techniques used to study the structure and the composition of AuNiGe-based ohmic contacts. Each of the following sections briefly describes the theory of the technique as well as how it was applied. Sections 3.2 and 3.3 on Focused Ion Beam (FIB) and Scanning Electron Microscopy (SEM) respectively describe how the samples were prepared for further study. These steps were required as Transmission Electron Microscopy (TEM) requires any sample to be less than 100 nm thick and ideally less than 50 nm. Prior to this step the samples were still fully functioning Hall bars. Sections 3.4 and 3.5 on TEM and Energy-Dispersive X-ray Spectroscopy (EDS) respectively describes how these techniques were used for extracting the crystallographic structure as well as the elemental composition of the samples. The work was done in collaboration with the Henry Royce Institute as well as Royce@Oxford. Without their equipment and expertise, the following work would not have been possible. Note that due to the extenuating circumstances caused by COVID-19, all microscopy images and derived data were taken by the support scientists as the Department of Materials at the University of Oxford with my direct supervision.

3.2 Focused Ion Beam

Focused Ion Beam microscopy is a microscopy technique used in various aspects of material science and more specifically in the preparation of TEM samples. For a more in-depth review of FIB, which goes beyond the uses in this thesis, see Ref. [67]. FIB works on the principle of creating ions by connecting a reservoir material, usually Ga, to a fine Tungsten needle in a strong electric field, liquefying the material [68]. Eventually ions are emitted and led through a series of apertures in order to properly focus the beam, shown in Fig. 3.1. The ion used in the FIB preparation of a TEM sample is very important. Ga, which is the most common ion used in FIB, is also one of the main elements in GaAs/AlGaAs-based two-dimensional electron gases. As a result, using a Ga ion beam would not be appropriate due to the excess Ga which would then appear in any elemental analysis of the sample. In this thesis, a Xe ion beam was used in order to avoid this issue.

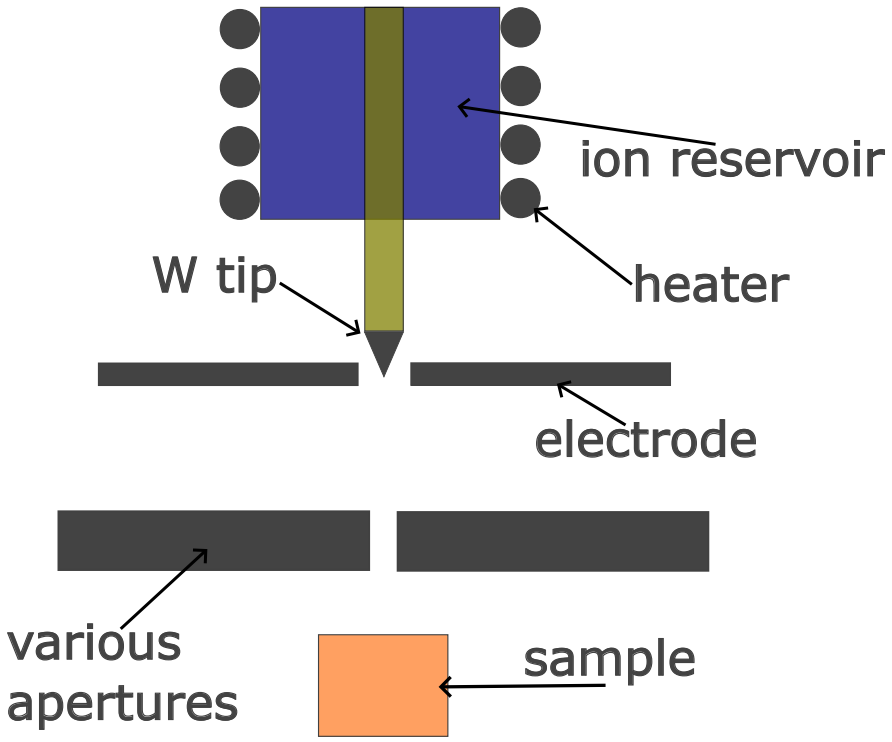

Figure 3.1: Focused Ion Beam schematic. Initially the ion reservoir is heated so that it wets the tungsten tip. An extraction field, typically greater than 10^8V/cm for Ga, is then applied using the electrodes in order to ionise the reservoir element. The ions are then emitted by the tip and go through a series of apertures in order to focus the beam. The ions are accelerated using energies typically in the 5-50 keV range, and the accelerating energy determines whether the beam will cause deposition or etching.

The mode of the FIB depends on the energy involved. At energies of 30-40 keV and

using a precursor gas [69] the FIB is used for the deposition of material, whereas at higher energies it is used to etch material away. For preparing a TEM sample both of these modes are required. Initially a region of interest is marked by depositing a mixture of platinum and carbon on top of the region. Then the Xe beam is used to etch around the region of interest in order to extract a cross-section of the sample, see Fig. 3.2. Once the sample has been extracted the entire specimen is treated with the Xe beam in order to thin it. Originally the thickness of the samples is in the order of microns, but needs to be thinned down to less than 100 nm in order to be used for TEM [70]. Ultimately the sample is moved onto a grid, usually copper, for TEM/EDS analysis.

(a)

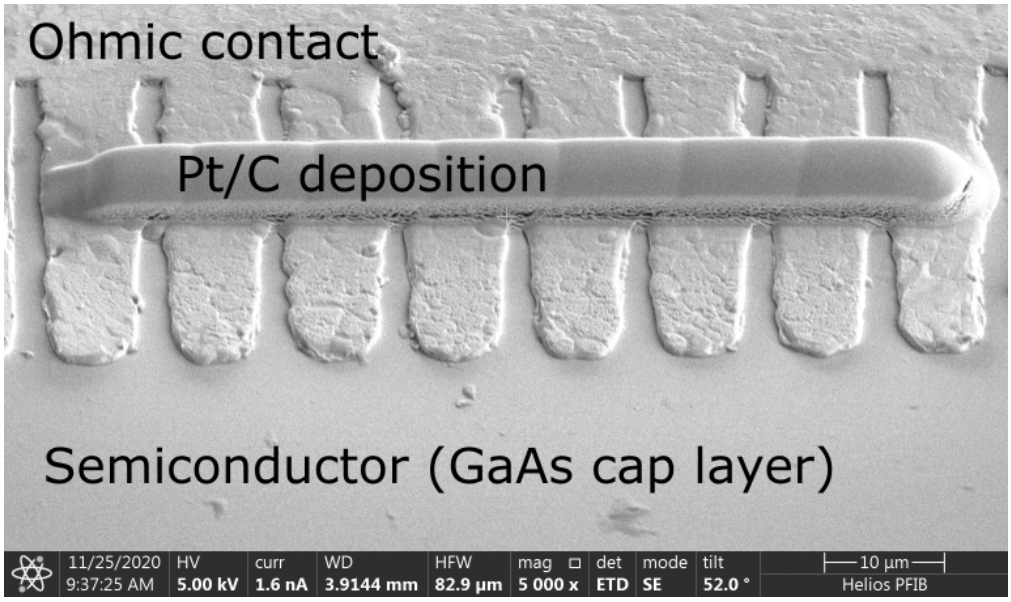

(b)

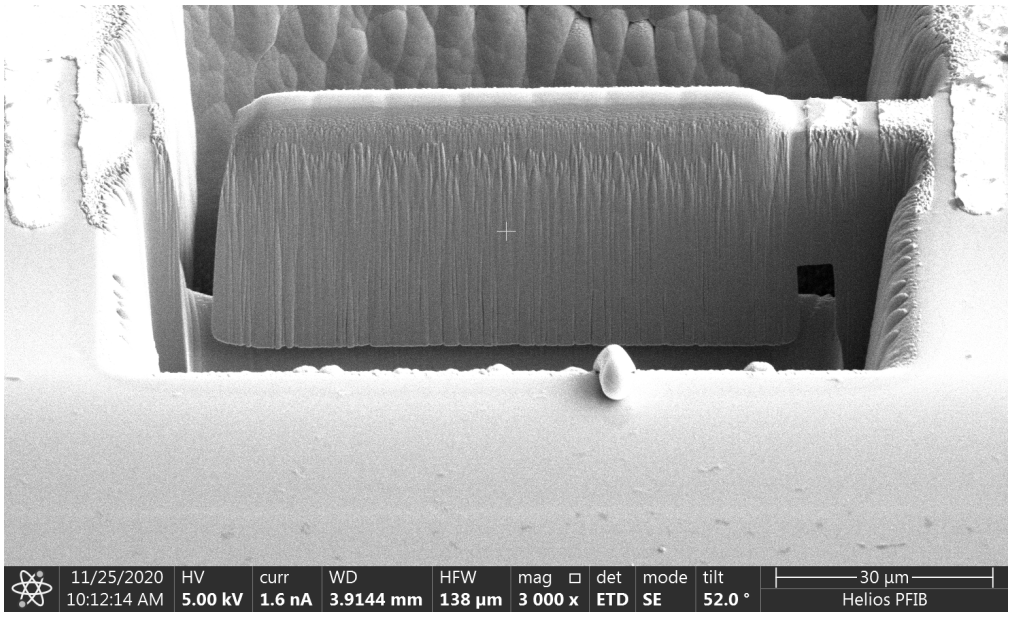

Figure 3.2: Figures showing the FIB extraction of sample used for TEM. (a) The initial deposition of Pt/C on top of the V834 crenellations. The area immediately below this region is what will be extracted for TEM cross section imaging after being thinned. (b) The sample right before it is extracted and thinned. A triangular trench has been dug on both sides of the region defined by the Pt/C deposit. The remaining steps are to attach a needle to the deposition and etch the sample off the rest of the wafer before thinning it. Credit for the images goes to Dr Gareth Hughes.

3.3 Scanning Electron Microscopy

A Scanning Electron Microscope uses high energy electrons in order to provide information on the surface topography of a material, up to a depth of 1 μm, but usually less. The primary electrons are typically excited using a tungsten filament heated up to 2500 °C. Various lenses are then used to focus the electrons appropriately over the selected area. Qualitatively, SEM is similar to FIB, but with electrons instead of positive ions. For a schematic see Fig. 3.3. Interactions between the primary electrons and the material then produces secondary electrons, backscattered electrons, and X-rays which are then detected in order to form an image. The secondary electrons are the ones knocked out of orbit by the primary electrons. They are more numerous, and originate near the surface of the sample. Backscattered electrons on the other hand are the result of primary electrons being deflected by the nucleus of an atom, having much greater penetration depth, but are significantly fewer in numbers with a lower resolution [71].

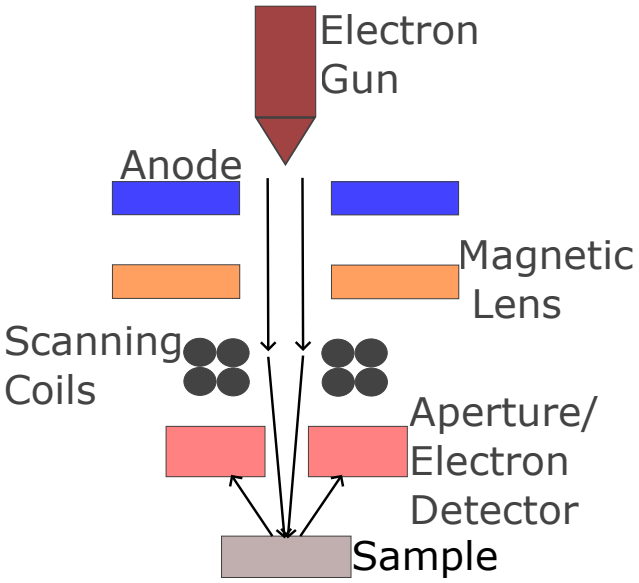

Figure 3.3: Schematic of a Scanning Electron Microscope. Initially electrons are excited at the electron gun, usually from a tungsten filament. Then the anode and magnetic lenses concentrate the electron beam into a fine probe, which is scanned across the surface of the sample. The purpose of the scan coils is to finely adjust the electron beam in order to get a raster image of the surface area. The electron beam interacts with the sample surface to create secondary electrons, backscattered electrons, and X-rays, which are captured by detectors from which the images are created by displacing the instantaneous signal on a screen at a position corresponding to the beam position of the sample.

3.4 Transmission Electron Microscopy

The Transmission Electron Microscope depends on the transmission of electrons through a specimen and has a variety of different modes. Here we will describe Scanning Transmission Electron Microscopy (STEM) and Selected Area Diffraction (SAD), which were used to study the AuNiGe ohmic contacts. Both methods have similarities with SEM, as their initial premise is identical, the firing of electrons at a sample. As a result, the electron gun, lenses, and vacuum system are all very similar to each other; however, the way the image is produced is entirely different [72]. In addition, TEM techniques aim to gather information about the internal structure of the image by transmitting electrons through a thin sample, whereas SEM aims to investigate the surface.

SAD is a technique performed using TEM equipment based on the diffraction of electrons. A parallel electron beam is concentrated on the area of interest causing diffraction at particular angles given by

$$n\lambda = d\sin(\theta_n), \tag{3.1}$$

where n is the order of diffraction, λ is the wavelength of the electron, d is the spacing of the planes, and θ_n is the angle of scattering for constructive interference. This process results in a SAD diffraction pattern. In order to compare these diffraction patterns a piece of software called CrysTBox, which compares given diffraction patterns to the diffraction pattern of a suspected compound, was used. CrysTBox is then able to determine the crystal orientation, index diffractions spots, and provide an overall agreement between a diffraction pattern and a suspected compound. Another possible diffraction pattern which can be observed is Kikuchi line patterns. These are the resultant diffraction pattern of thick crystals with multiple Bragg reflections of inelastically scattered electrons [73]. Therefore they are proof of crystalline structure, but cannot be used to identify phases in a compound.

STEM is a combination of TEM and SEM. As mentioned previously, the electron beam in TEM passes through the sample, dramatically improving the resolution relative to an equivalent SEM setup, as resolution is proportional to the sample volume [74], as shown in Fig. 3.4. With a sufficiently fine probe of electrons a resolution greater than 0.2 nm can be reached, which is sufficient to resolve individual columns of atoms in an image. These properties make STEM an ideal microscopy technique for studying microscopic ohmic contacts.

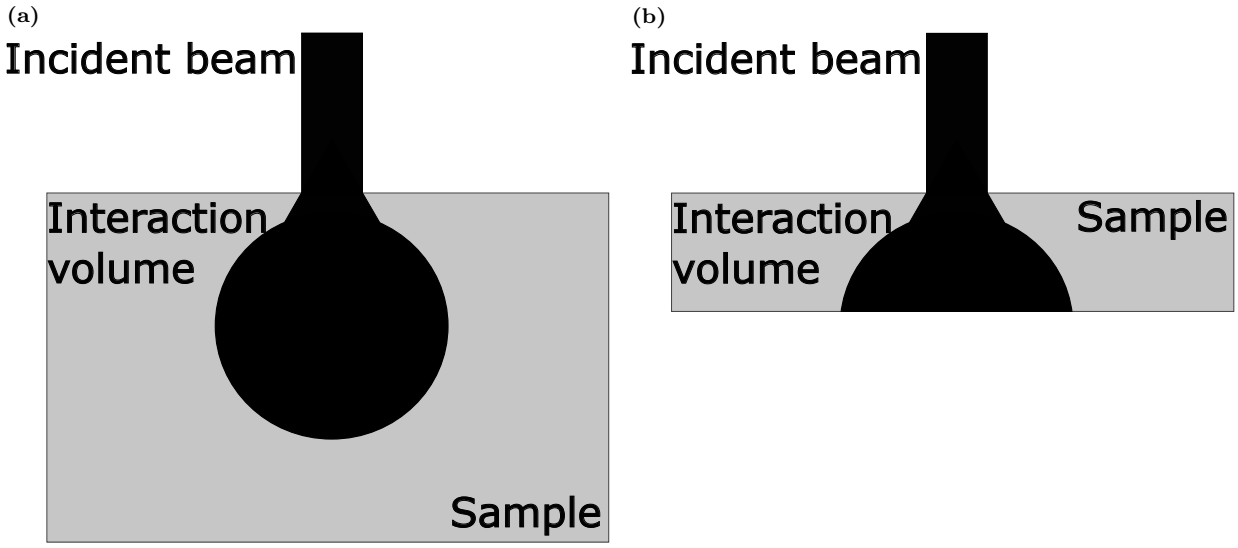

Figure 3.4: Comparison of sample volume in (a) SEM and (b) STEM. (a) The total interaction volume of a typical SEM setup whereas (b) shows the interaction volume of a STEM setup. Because the resolution of any electron microscopy setup is dependent on the interaction volume then, all else being equal, the STEM setup will have a better resolution.

3.5 Energy-dispersive X-ray spectroscopy

Energy-dispersive X-ray spectroscopy is a microanalysis technique, which determines the elemental composition of a sample by looking at the unique energies of X-rays emitted by the sample due to the incident electron beam [75]. When an electron of sufficient energy hits an electron in orbit around an atom then it is knocked out of orbit leaving the atom in an excited state. Depending on the orbit of the emitted electron, one of three things may happen. If the emitted electron was in an outer orbit, usually in the M shell, then when the state is filled again a low-energy photon, usually in the visible range, is emitted in a process known as cathodoluminescence. If the emitted electron was in an inner state then when the state is filled again it will either give off a characteristic X-ray photon or a characteristic Auger electron. EDS uses the characteristic X-rays to calculate the elemental composition of a sample. The energy of these X-rays is given by

$$\Delta E = \frac{hc}{\lambda}, \tag{3.2}$$

where λ is the wavelength of the X-ray, h is Planck's constant, and c is the speed of light in a vacuum. Figure 3.5 shows the various possible photon emissions from an atom. Note that sub-shells have been omitted since their energies are so close that they can usually not be distinguished. For example, Al has a Kα_1 emission at 1.48670 keV and a Kα_2 emission at 1.48627 keV [76].

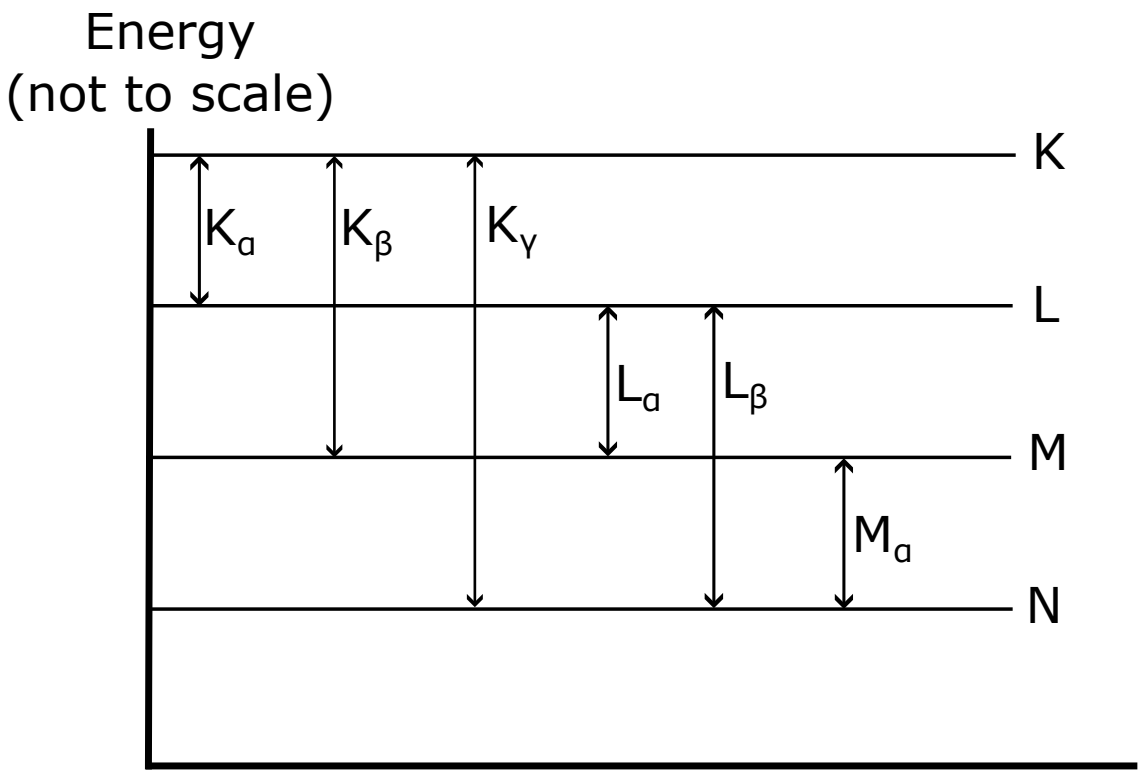

Figure 3.5: Energy levels used for EDS analysis. Note that the sub bands of the L, M, and N shells of which there are 3, 5 and 7 sub bands respectively have been omitted since they can usually not be distinguished due to smearing effects of the energies. In theory all of these energies are unique to an element, but in reality there can be some overlap.

One disadvantage of using EDS to identify the elemental composition is that, while in theory all elements have unique energies, this is not always the case in practice. Sometimes the energies involved are so close that they can be very difficult to distinguish [77]. This is especially the case when one element is dominating the spectrum as can be seen in Fig. 3.6, where due to the amount of Au present, its M line is completely dominating the spectrum from 2 to 2.3 keV. As a result, if there were any small amount of an element with a peak in this range it would be difficult to distinguish it from Au.

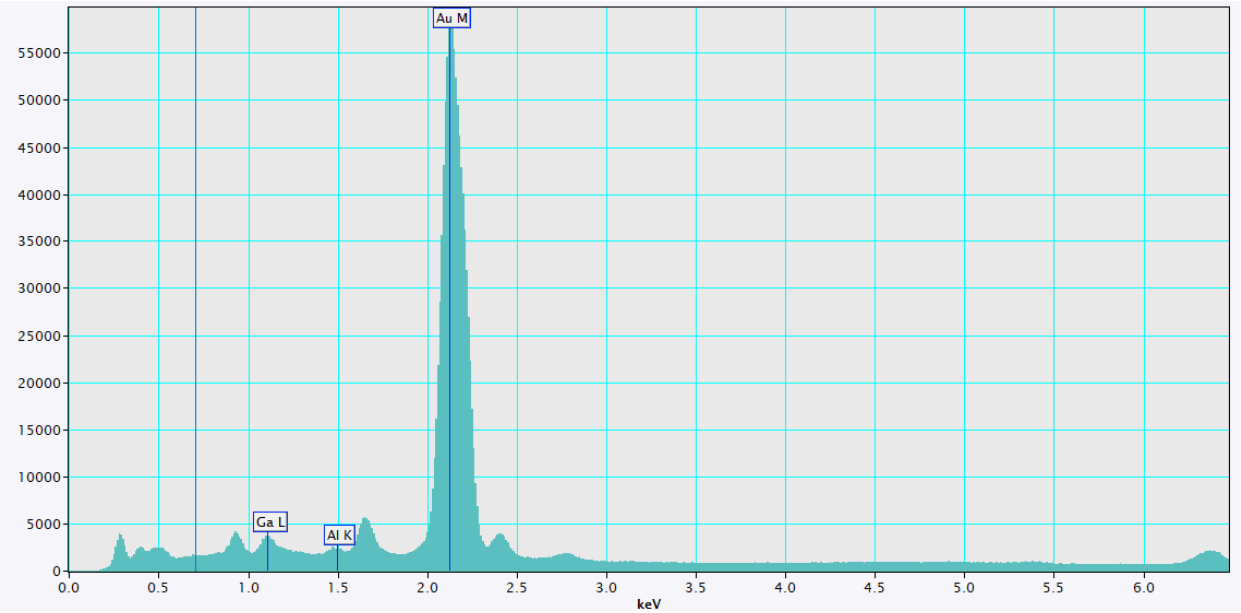

Figure 3.6: Typical EDS energy spectrum histogram from 0 to 6.5 keV where the Ga L, Al K, and the Au M peak have been highlighted. Note the width of the Au M peak, which is the dominant element in this spectrum. If there was a small amount of any other element with a peak in the 2 - 2.3 keV range then it would not be possible to distinguish it from the Au M peak. There are several peaks that are not highlighted, which is for a combination of reasons. Some are alternative peaks for Ga, Al, and Au which were not as suitable for determining the elemental composition. Other peaks are contaminants in the system which can be ignored; one example of this is Cu, which has a peak at 0.93 keV. Since the sample is put on a Cu grid, it is always expected to find some amounts of Cu when doing the elemental analysis. Credit for data taken for this images goes to Dr Ian Griffiths.

Chapter 4

Low-temperature experimental techniques

4.1 Introduction

In this chapter the low temperature experimental techniques and equipment used will be explained. The chapter is divided into two main sections; Section 4.2 explains the types of resistance measurements, how they differ, and which one is the most appropriate to use in a given circumstance. For sensitive measurements the choice of measurement technique becomes important because the leads used for measurements can vary, which could lead to erroneous results. Section 4.3 describes the most important pieces of equipment, which for the thesis is the 4.2 K LHe Dewar, the preamplifiers used for the noise measurements, and the Gifford McMahon fridge alongside its thermometry which was used for lower-temperature measurements, going down to about 0.5 K.

4.2 Resistance Measurements

The electrical resistance of samples is measured using two-terminal (2T) or four-terminal (4T) measurement techniques. The principle underlying these measurements is Ohms law [78],

$$V = IR, \tag{4.1}$$

where V is the voltage across the device, I is the current flowing through the device, and R is the resistance. The key feature of the n terminal measurement is that we can choose exactly what part of the system we are passing a current and a voltage through. Where these methods differ is in how they pass a current and measure the voltage across a system. Fundamentally there are four different types of contacts for electrical measurements; two for current and two for voltage.

4.2.1 Two-Terminal Measurements

Two-terminal measurements uses voltage and current probes that are combined prior to measuring any load including wires as shown in Fig. 4.1. This is the fastest and easiest possible electrical resistance measurement, but includes the leads in the measurement. In many cases this is not problematic as long as the lead resistance is significantly less than the sample resistance. However, as soon as these become comparable or the lead resistance becomes greater than the sample resistance then the measurement will be inaccurate. In the most extreme cases where the sample resistance is significantly less than the leads, which can often be the case in dilution refrigerators, then the sample resistance becomes little more than a rounding error for the measurement. One of the most common examples of a two-terminal resistance measurement is the multimeter.

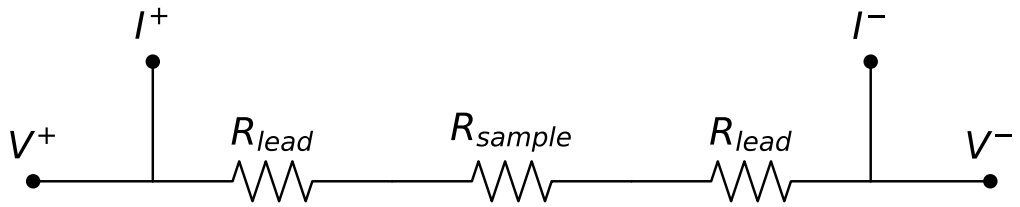

Figure 4.1: Two-terminal measurement schematic, where R_{lead} is the resistance of the leads, R_{sample} is the resistance of the sample, I^+ is the current source, I^- is the current drain (ground), V^+ is the voltage source, and V^- is the voltage drain. The schematic shows 4 separate terminals, but they are joined prior to measuring any load, hence why they are called two-terminal. As a result the lead resistances are included in the total resistance measurement, resulting in $R_{measured} = 2R_{lead} + R_{sample}$. If the lead resistances are very small relative to the sample resistance then the effects are negligible, however if the sample resistance is comparable or significantly less than the lead resistance then the measurement will not be accurate.

4.2.2 Four-Terminal Measurements

As a result of the shortcomings of 2T measurements another type of measurement is often required. This other type of measurement is the four-terminal measurement, or one of its derivatives, which will also be discussed here. The idea behind 4T measurements is to separate the voltage and current probes as is shown in Fig. 4.2. The downside of this method is that it requires additional leads going to the sample and is therefore not always possible. The upside with this measurement however is that it is significantly more accurate, as it eliminates the resistance of the leads from the measurement, meaning that the electrical resistance measured is only that of the sample [79]. With these improvements, measurements in the 0.1 Ω range becomes significantly easier, assuming the environment is not too noisy.

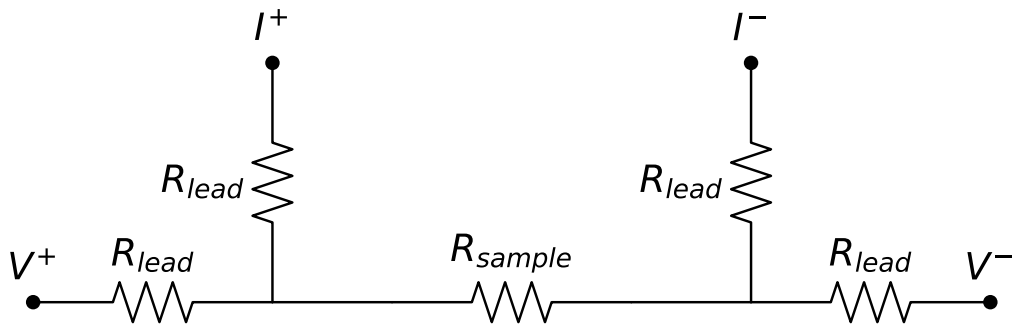

Figure 4.2: Four-terminal schematic, where R_{lead} is the resistance of the leads, R_{sample} is the resistance of the sample, I^+ is the current source, I^- is the current drain (ground), V^+ is the voltage source, and V^- is the voltage drain. Because the current and voltage sources/ drains are separated, which requires additional leads to the sample, the resistance of the leads is not picked up by the measurement so that $R_{measured} = R_{sample}$.

There are other types of measurements as well, but these are derivatives of the 4T measurement technique. So far the setups described have only had one voltage source, one voltage drain, one current source, and one current drain. However there is no reason as to why it is this way, except that it is easier to deal with. For example, a setup could have two current drains instead of one, in which case it could be called a five-terminal measurement.

4.3 Equipment

4.3.1 4.2 K dewar

The 4.2 K liquid helium dewar has been invaluable throughout this thesis and has many advantages over a fridge, despite being unable to go to as low a temperature. Measuring devices on a 4.2 K dewar, called dipping, is faster, cheaper, and a lot more flexible than using a fridge. As a result it is commonplace to characterise samples and make sure that they work in a 4.2 K dewar prior to using a fridge. With the right type of dipping probe, as was the case for this thesis, it is also possible to perform magnetic field measurements in the 100 mT range using a small superconducting solenoid. Another advantage of the dewar is that the bath temperature is known, the temperature is constant as long as there is liquid helium left in the dewar, and it is better heat sunk because it is submerged in a liquid.

4.3.2 Noise measurements

For the noise measurements carried out in this thesis the NI PXI-5922 16 to 24-Bit Flexible-Resolution Digitizer was used for digitizing the signal and sending it to the measurement computer. It has a noise floor of between 3 and 4 nV/ $\sqrt{\text{Hz}}$ from 50 kHz to 1 MHz [80]. The signal was measured using either two NF LI75-A low-noise amplifiers, which have a voltage noise floor of 1.2 nV/ $\sqrt{\text{Hz}}$ (at 100 kHz) and a current noise floor of 13 fA/ $\sqrt{\text{Hz}}$ [81], or two NF multichannel amplifiers (CMP 60116-2) with a voltage noise floor of 2.5 nV/ $\sqrt{\text{Hz}}$ (at 1 MHz) and a current noise floor of 15 fA/ $\sqrt{\text{Hz}}$ [82]. For the full noise floor of the LI75-A as a function of the frequency, see Fig. 4.3; note the $1/f$ behaviour at low frequency which flattens out beyond 1 kHz. Both the NI PXI-5922 and the NF multichannel amplifier follow similar curves, but in the case of the NI PXI-5922 the curve has not flattened until 50 kHz and it has a known noise peak at 10 kHz. This has implications on what parts of the spectrum can be used for analysing the Johnson noise.

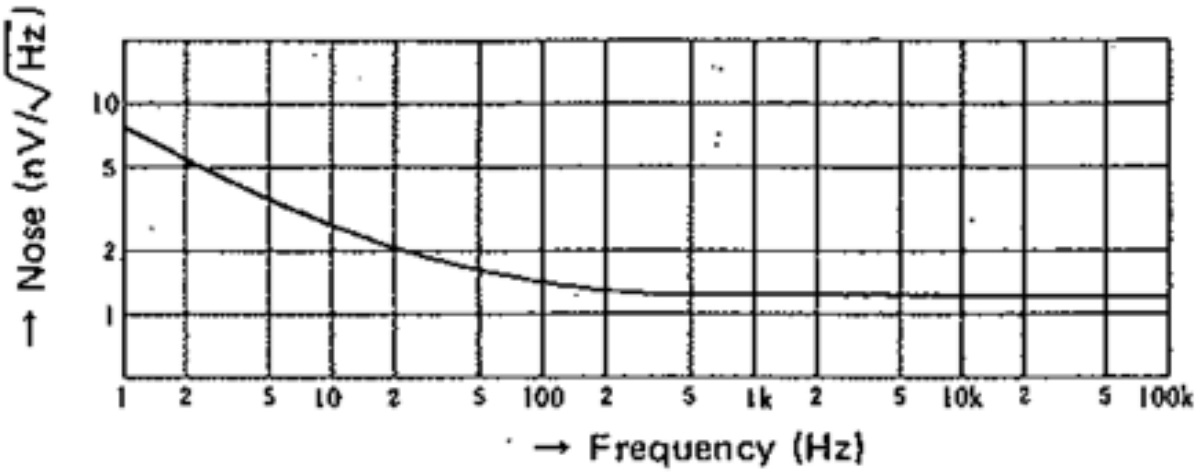

Figure 4.3: LI75-A noise floor in units of $n\text{V}/\sqrt{\text{Hz}}$ as a function of frequency. The noise decreases as a function of the frequency until about 1 kHz where it levels out at 1.2 $n\text{V}/\sqrt{\text{Hz}}$. As a result, these preamplifiers are not able to measure any noise below this value by themselves. This figure, as well as the stated noise floor, was taken from the manual [81].

4.3.3 Gifford McMahon Fridge

The main fridge used in this thesis was a custom-made Vericold fridge with a 70 K, 4 K, and demagnetization stage attached to the 4 K stage. The Vericold fridge is a Gifford-McMahon-type fridge, first introduced in 1960 [83], which works as described in Fig. 4.4. Specifically, there is an attached compressor which pumps He in order to remove heat from the system, which is then removed using a water loop leading to a 70 K and a 4 K stage. To cool down even further a demagnetization stage is used, see Fig. 4.5, which is connected to the 4 K stage using a mechanical switch. While connected to the 4 K stage the magnet is slowly up ramped by applying a current going up to 30 A so that the temperature stays at approximately 4 K. Once the magnetic field is ramped up, the switch is opened, isolating the demagnetization stage from the 4 K stage, at which point the field is ramped down to 0 T thus adiabatically lowering the temperature [84]. The isolated stage can reach temperatures as low as 0.5 K and will slowly heat back up to 4 K over the course of days at which point the pill can be closed again and the cycle repeated.

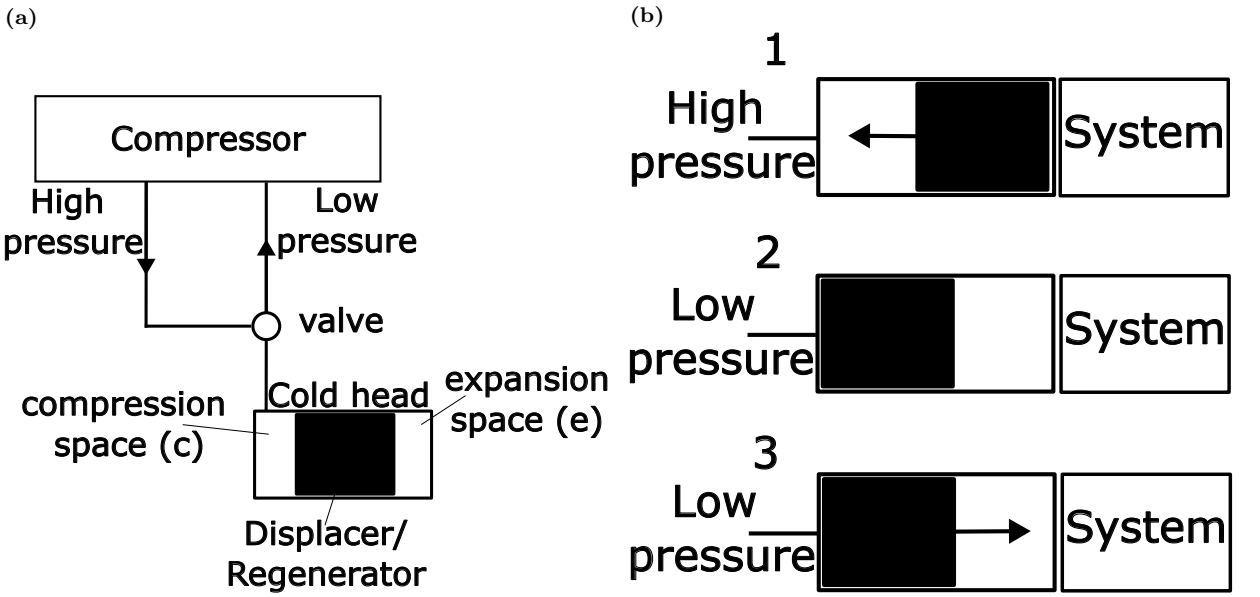

Figure 4.4: Gifford McMahon fridge and cooling cycle. (a) Shows the schematic for the Gifford McMahon fridge, which consists of a compressor with a high and a low pressure line connected to a cold head via a valve. The cold head consists of two spaces; a compression space and an expansion space, which are separated by a displacer/regenerator. The displacer is a solid body that can be moved mechanically and lets gas pass through from one side to the other. (b) Shows the cold head at various stages of the cooling cycle. Initially in 1 when the high pressure line is connected, the displacer, which at this stage is cooler than the gas, is moved mechanically from right to left, causing it to heat up, meaning that the gas cools via Joule expansion as it is pushed from the left to the right. Then in 2 the high pressure line is closed and the low pressure line is opened. As a result the high pressure gas on the right hand side of the cold head starts expanding and cools dramatically as some of it moves past the displacer and out of the system. This also cools the displacer back down. Ultimately in 3 the displacer is moved back to the right hand side, forcing the remaining gas to the left hand side of the cold head. At this point the low pressure line is closed, the high pressure line is opened, and the cycle repeats.

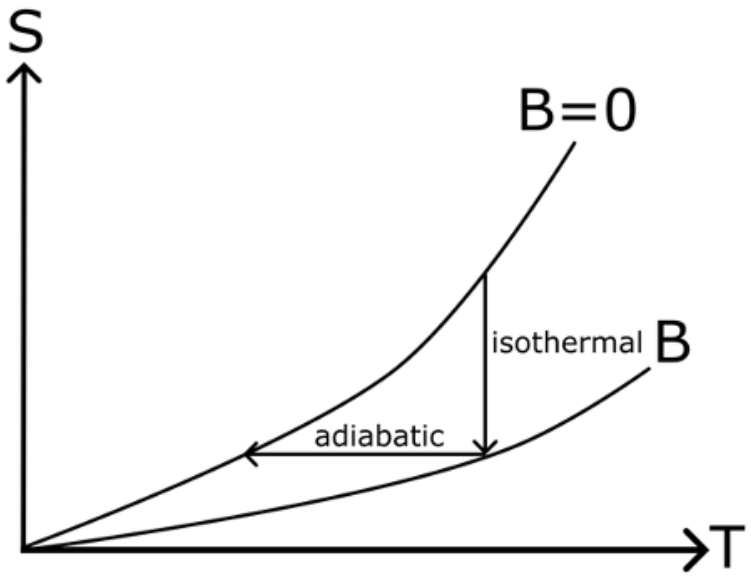

Figure 4.5: Adiabatic demagnetization plot for the pill showing the entropy S as a function of the temperature T of the two-step cooling process. First the magnetic field is isothermally ramped up. Applying a magnetic field reduces the disorder in the system and therefore the entropy. This process is slow and usually entails keeping the system connected to a bath so that it can lose the heat that is generated. Once the field is fully ramped up, the system is thermally isolated from its surroundings. At this stage the magnetic field is ramped down adiabatically, i.e. as fast as possible. Since the rapid decrease in the applied magnetic field cannot reduce the entropy due to the second law of thermodynamics, the temperature of the isolated system drops to make up for it.

4.3.3.1 Thermometry

Knowing the temperature is of the utmost importance when performing experiments at low T, making reliable thermometers a requirement. Thermometers can either be primary or secondary, with the latter requiring calibration in order to work. The Gifford-McMahon fridge used in this thesis has a Ruthenium Oxide (RuO_2)-based resistance thermometer, which are commercially calibrated and valid down to approximately 50 mK although there are cases of them working down to 5 mK [85]. At lower temperatures they stop working due to parasitic rf heating causing the resistance to flatten as a function of the temperature [86].

Chapter 5

Cross-correlation measurement of Electronic noise

5.1 Introduction

Electronic noise is everywhere and while it is usually a nuisance it may contain valuable information about the system being measured [87][88]. The causes of electronic noise can be attributed to different types of interactions between the electrons in a conductor and its environment. The main types of noise observed in semiconductors are $1/f$ noise, Johnson noise, and Schottky noise [89]; these types are classified by their voltage rms with different types of noise dominating at different frequencies. The aim of this chapter is to describe these types of noise and to explore how Johnson noise may be used to measure the electron temperature in out-of-equilibrium scenarios, including a brief overview of signal-processing techniques such as the Fourier transform, cross-correlation and Welch's method.

5.2 Electronic noise in semiconductors

The most common types of electronic noise in semiconductors are $1/f$ noise, Johnson noise, and Schottky noise, which dominate in different frequency regimes. The following work describes these types of noise, and whether or not they are relevant in the context of measuring the electron temperature in a two-dimensional electron gas.

5.2.1 $1/f$ noise

$1/f$ noise, also called Flicker noise, dominates the spectrum at lower frequencies, as shown on the left hand side of Fig. 5.1. Despite its name however the general form of $1/f$ noise is actually given by

$$S(f) \propto \frac{1}{f^{\alpha}}, \tag{5.1}$$

where $S(f)$ is the power spectral density, f is the frequency, and α is an exponent with a value between 0 and 2 [90, 91]. This type of noise is found in all electronics to varying extents, but is thought to be the result of crystalline defects causing relaxation events in semiconductors. The main issue with this type of noise however is that it is extremely device specific, thus making it an unsuitable candidate for thermometry and a general nuisance at low frequencies [92].

5.2.2 Johnson noise

Johnson noise is the result of random fluctuations of electrons across a conductor at a finite temperature even when no bias is applied meaning the long term average of the potential is zero [93]. However the rms voltage, given by

$$\langle V^2 \rangle = \frac{1}{\tilde{T}} \int_0^{\tilde{T}} (V(t) - \langle V \rangle)^2 dt = \frac{1}{\tilde{T}} \int_0^{\tilde{T}} V(t)^2 dt, \tag{5.2}$$

where V is the voltage, and $\tilde{T}$ is the total time that t integrates over, is not zero. These voltage fluctuations, usually measured in the frequency domain, are by definition related to the power spectral density via

$$\frac{1}{T} \int_0^{T} V(t)^2 dt = \int_0^{\infty} S(f) df, \tag{5.3}$$

where $S(f)$ is the power spectral density as a function of the frequency f, given by

$$S(f) = \frac{4Rhf}{e^{\frac{hf}{k_B T_e}} - 1}, \tag{5.4}$$

where R is the resistance, h is Plancks constant, k_B is the Boltzmann constant, and T_e is the electron temperature [94]. From this equation there are two regimes, $f < \frac{k_B T_e}{h}$ and $f \geq \frac{k_B T_e}{h}$. In the first regime the Johnson noise will be flat as a function of the frequency, whereas in the second regime there will be a roll-off as shown in Fig. 5.1. In the lower regime, Eq. 5.4 can be simplified to

$$S(f) = 4k_B T_e R, \tag{5.5}$$

which is completely independent of the frequency. Furthermore, in this regime Johnson noise is only a function of the resistance and the electron temperature. In appropriate devices the resistance can be accurately measured, leaving Johnson noise as a measure of the electron temperature, making it an ideal candidate as a primary thermometer.

The main drawback of using Johnson noise is that at lower temperatures the expected thermal fluctuations in $V(t)$ may drop below the voltage noise floor of the measurement equipment. For example, at 4.2 K a 100 Ω resistor will have a Johnson noise of 2.32×10^{-20} $\mathrm{V^2 Hz^{-1}}$, corresponding to a voltage rms of 1.52×10^{-10} $\mathrm{V}/\sqrt{\mathrm{Hz}}$.

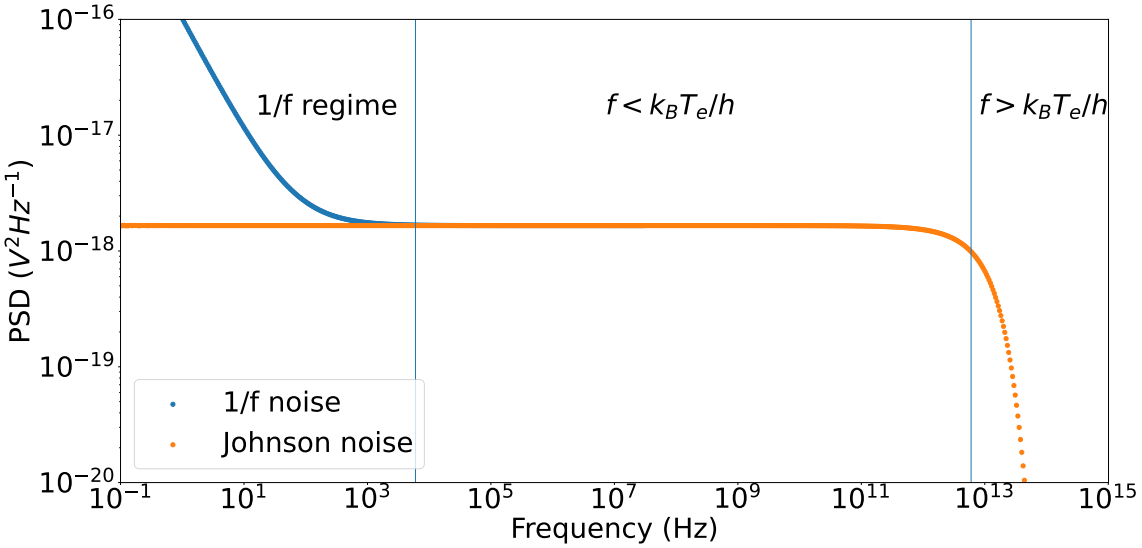

Figure 5.1: Typical noise spectrum of a 100 ohm resistors at 300 K from 0.1 to 10^{15} Hz. At low frequencies, typically below 10 kHz, the $1/f$ noise dominates any measurement. $1/f$ noise is very device specific and is generally a nuisance. At medium frequencies, typically between 100 kHz and 1 THz, the flat part of the Johnson noise will dominate. Finally at high frequencies, beyond 10 THz, the roll-off of the Johnson noise will occur. Therefore the flat part of the Johnson noise can be used as a primary thermometer as it only depends on the resistance and the temperature of the system. As an added bonus, because Johnson noise is flat, the resolution of the frequency data is not important.

5.2.3 Schottky noise

Schottky noise, often abbreviated as shot noise, is the result of the quantised nature of charge, which becomes apparent at very low currents and when there is a potential barrier [95]. In a semiconductor any barrier will cause a build-up of potential until electrons gain enough potential energy to overcome it. At large currents this process is more or less continuous, but at sufficiently low currents the quantised nature of electron charge becomes relevant and will appear as sudden noise peaks in the spectrum. Semiconductors can suffer from a significant amount of shot noise, where for a p-n junction the rms shot voltage is given by

$$S_I = 2qI_{DC}\Delta f, \tag{5.6}$$

where q is the elementary charge in Coulombs, I_{DC} is the DC current in A, and Δf is the frequency bandwidth [96]. Letting $q = 1.609 \times 10^{-19}$ C, $I_{DC} = 10$ μA, and $\Delta f = 100$ kHz gives a rms shot voltage of 5.67×10^{-10} V/$\sqrt{\text{Hz}}$, which is comparable to the Johnson noise. As a result shot noise could be an issue, but only if there is charge build-up in the system

[97]. For the narrow Hall bars investigated in this thesis, this is not the case - we expect the Johnson noise to be dominant.

5.3 Digital signal-processing techniques

In Section 5.2 Johnson noise was established as a viable primary thermometer for measuring the electron temperature. This section will outline the numerical processing techniques used to extract the electron temperature T_e from measurements.

5.3.1 Discrete Fourier Transform

The Discrete Fourier Transform (DFT) is a mathematical method to convert data sampled from a continuous function into its inverse domain. The most common example is converting from the time-domain into the frequency domain, given by

$$X_k = \sum_{n=0}^{N-1} x_n \times e^{-\frac{2\pi i}{N} kn}, \tag{5.7}$$

where X_k is the Fourier transform of x_n, the originally sampled data [98]. One of the main motivations behind this method is that by converting from the time-domain to the frequency domain one can see what frequencies make up the original time-domain data as demonstrated in Fig. 5.2. The original time-domain data in (a) is a combination of two separate sine waves of frequencies 1 and 2 Hz. When converted into the frequency domain as seen in (b) this appears as two peaks, one at 1 Hz and the other at 2 Hz, as expected. With this in mind, throughout the thesis $V(t)$ will represent the discrete voltage measured as a function of time, $V(f)$ will be the DFT of $V(t)$, and a subscript will be used when it is a generic signal and the domain is not relevant unless otherwise specified.

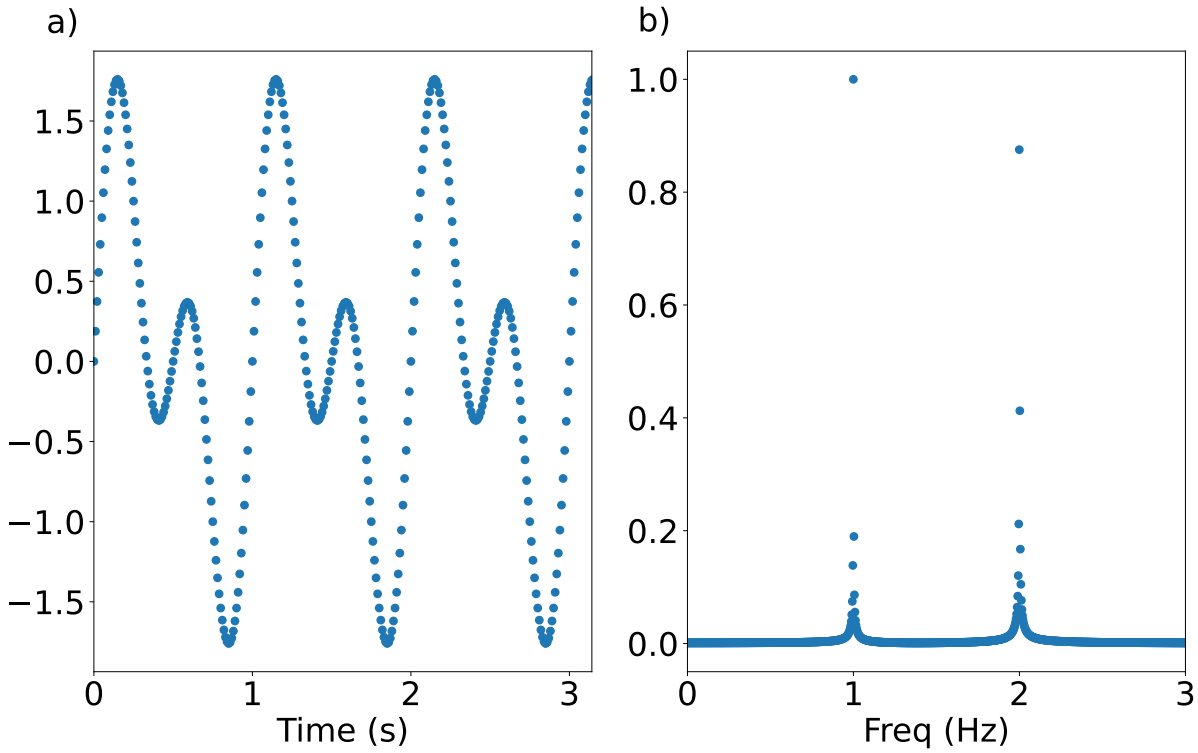

Figure 5.2: (a) The result of a superposition of sine waves of 1 and 2 Hz in the time-domain. (b) The DFT of the combined sine wave, showing clear peaks at 1 and 2 Hz. In theory the two peaks should be perfect Kronecker deltas, however some widening has occurred since the original signal domain is finite, only existing from $t = 0$ to $t = \pi$.

5.3.2 Auto-correlation

The auto-correlation of a discrete signal V_n is defined as

$$r_V(n) = V_n^* V_n = \sum_{m=-\infty}^{\infty} V_m^* V_{n+m}, \tag{5.8}$$

where * indicates the complex conjugate. Auto-correlation can be thought of as how much a signal has in common with a delayed copy of itself [99] and is closely linked with the power spectral density. The main drawback of auto-correlation is that anything wrong with the initial signal, especially noise or other unwanted contributions, will remain after auto-correlation.

5.3.3 Power spectral density

The power spectral density, commonly called PSD, describes how the power of a time-domain signal is distributed as a function of frequency [100]. It is denoted as $S(f)$ and is defined as

$$S = \frac{1}{N}\sum_{n=0}^{N-1}|V(t)|^2 \tag{5.9}$$

for a discrete signal, where N is the number of data points. Using Parseval's theorem [101] this becomes

$$S(f) = \frac{1}{N}(FT(V(t)) \times FT(V(t))^*). \tag{5.10}$$

Using Eq. 5.7 this is equivalent to

$$S(f) = \frac{1}{N}|V(f)|^2, \tag{5.11}$$

where $V(f)$ is the Fourier transform of $V(t)$. The units of the power spectral density are $\mathrm{V^2Hz^{-1}}$ as it represents the variance of the data, but measured signals are often expressed in units of $\mathrm{V}/\sqrt{\mathrm{Hz}}$ which are in terms of the standard deviation of the data. Note that this expression is identical to the Fourier transform of the auto-correlation function, which is referred to as the Wiener–Khinchin theorem [102]. Thus in the case of voltage measured as a function of time it acts as the link between the measured voltage and the power spectral density used to calculate the electron temperature seen in Eq. 5.4.

5.3.4 Cross-correlation

Cross-correlation is very similar to auto-correlation, but overcomes auto-correlation main drawback, flaws in the original signal, at the cost of additional complexity. Instead of correlating a signal with itself, it is instead correlated with another signal, being defined as

$$r_{VG}(n) = (V^* \times G)_n = \sum_{m=-\infty}^{\infty} V_m^* \times G_{n+m}, \tag{5.12}$$

where V and G are two separate signals [103]. The cross-correlation measures how much one signal has in common with a time-delayed copy of another signal, which can be seen in Fig. 5.3 and Fig. 5.4. Therefore auto-correlation can just be thought of as the simplest case of cross-correlation where $V = G$. Additionally one can write the cross-correlated power

spectral density as

$$S(f) = \frac{1}{N}|V(f) \times G^*(f)|, \tag{5.13}$$

which corresponds to the spectral density that both the signals have in common. In the context of electronic noise measurements a cross-correlated measurement will only consist of the noise contributions that are common to both V and G [104]. This means that if the two signals have separate power supplies and wiring, then these noise contributions will not be present in the cross-correlated signal. Considering how noisy room-temperature components can be, shown in Eq. 5.5 where there is a linear dependence on T_e, this is a necessity when attempting to measure low temperature Johnson noise contributions accurately in a system.

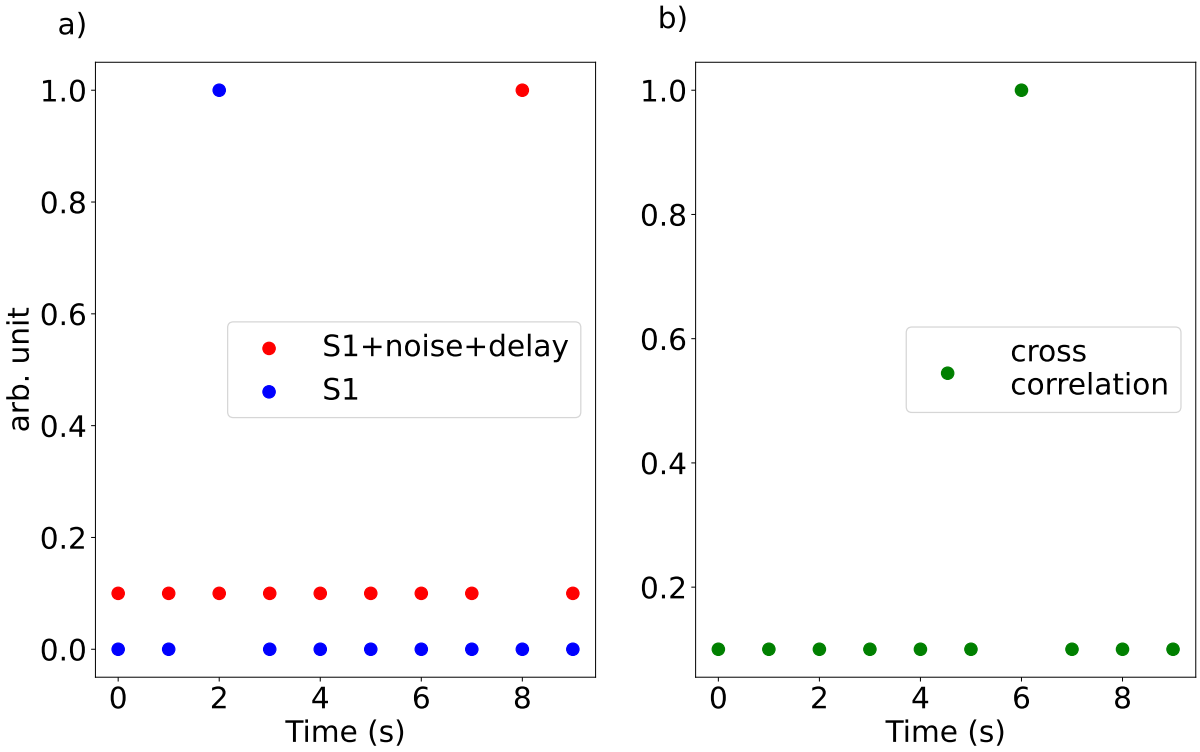

Figure 5.3: (a) Figure consists of a blue and a red signal. The blue signal has a peak at $t = 2$ seconds and is zero everywhere else. The red signal is the same as the blue signal, but background noise as well as a delay of 6 seconds has been added so that it peaks at $t = 8$ seconds. (b) The result of cross-correlating the two signals and bringing it back into the time-domain. The new signal has a peak at $t = 6$ seconds which is the time delay between the two original signals, thus illustrating how cross-correlation can be used to find the delay between two signals.

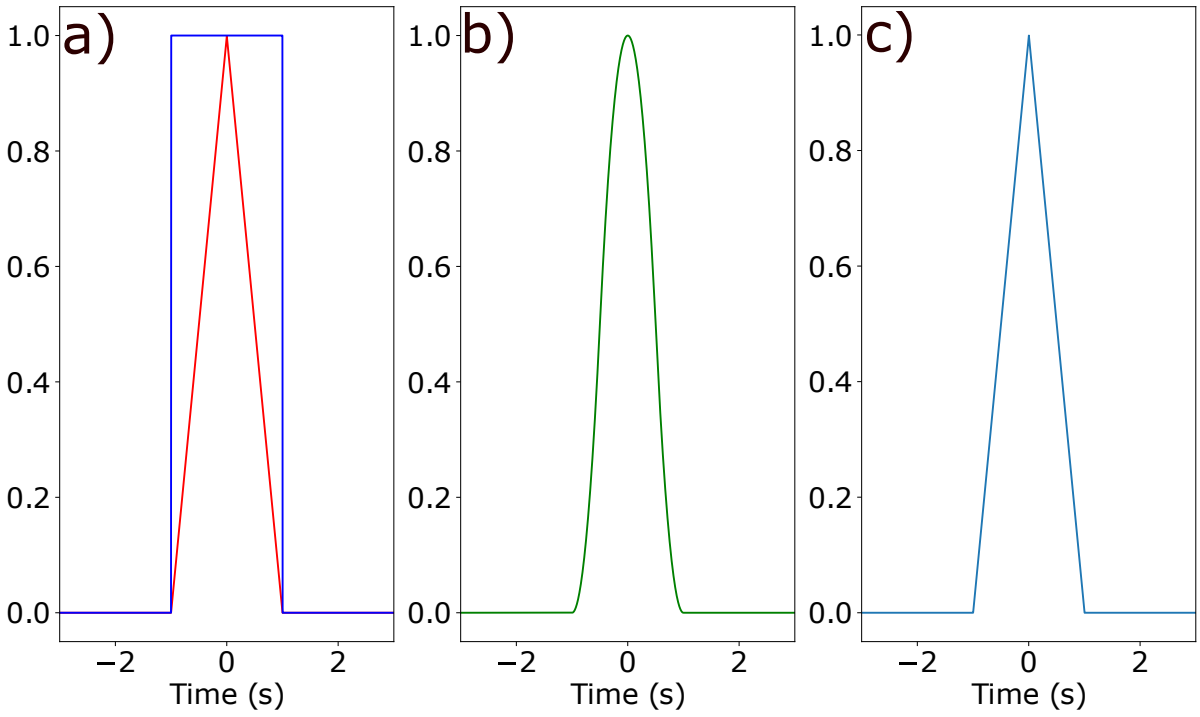

Figure 5.4: (a) Two waves, a triangular wave (red) and a square wave (blue). Note that in this case the correlation of these two signals will be another triangular wave identical to the red signal. (b) The resulting cross-correlated wave of the two signals brought back into the time-domain. (c) The result of using the cross-correlated signal calculated in (b) in order to find what both of the signals have in common.

5.3.5 Welch's method

Welch's method is a tool for calculating the power spectral density of a signal that sacrifices the resolution of the data in favour of reducing the noise peaks [105]. When measuring the Johnson noise the reduction in resolution is, to a point, not an issue because the defining feature of Johnson noise is that it is flat as a function of frequency. The general approach of Welch's method is to take a data set

$$V(t) = V_0, V_1, ..., V_{N-1}, \tag{5.14}$$

and partition it into overlapping segments. This is shown in Fig. 5.5 where M is the number of points in each segment, S is the shift between segments therefore determining the overlap, and K is the total number of segments. For each of these segments the DFT is calculated

with some windowing function at frequency $f = i/M$, where $-(M/2-1) \leq i \leq M/2$, giving

$$V_k(f) = \sum_m V_m w_m e^{2\pi i f m}, \tag{5.15}$$

where w is the windowing function, k is the segment index, and m is the index for all the points in the kth segment given by $(k-1)S, ..., M + (k-1)S - 1$. For each of the segments the power spectral density $P_k(f)$, called the modified periodogram, is calculated and given by

$$P_k(f) = \frac{1}{W}|V_k(f)|^2, \tag{5.16}$$

where W normalises the right hand side and depends on the windowing function. Finally the periodograms are all averaged in order to get the estimated PSD, i.e.

$$S(f) = \frac{1}{K}\sum_{k-1}^{K} P_k(f). \tag{5.17}$$

Note that if $K \to N$ the original equation for the power spectral density is recovered. Welch's method can also be used in the case of cross-correlated signals. The only required change is in Eq. 5.16 where $|V_k(f)|^2$ needs to be replaced with $|V_k(f) \times G_k^*(f)|$ where G is another voltage signal. Lastly the window function w used for calculating the periodogram varies greatly [106], but in this thesis a Hann function is used, as testing found that it made very little difference.

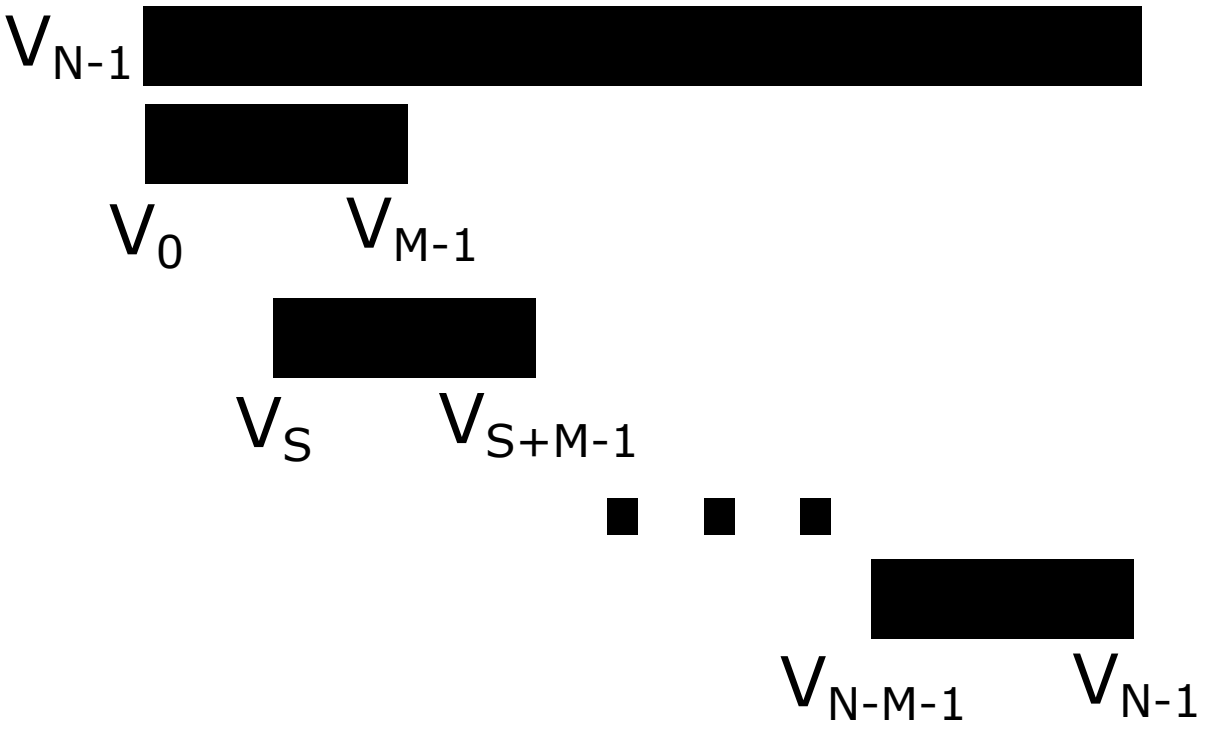

Figure 5.5: Welch's method data overlap. An initial data set V_{N-1} is divided into segments with a specified amount of overlap, usually 0.5, meaning that for any segment the first half of its data will overlap with the previous segment and the second half of its data will overlap with the next segment. The DFT is taken of each segment which is in turn averaged and normalised in order to get the power spectral density with reduced noise and resolution.

5.4 Signal processing workflow

The previous section discussed all the concepts required in order to successfully measure the electron temperature of a system using Johnson noise. The aim of this section is to describe how all of these concepts are brought together in order to measure the electron temperature using the example of a system at a known $T_e = 4.2$ K and resistance. The processing flow, shown in Fig. 5.6, begins with the real voltage fluctuations as a function of time. It is impossible to perfectly measure these fluctuations due to limitations on the resolution and bandwidth, but using NF LI75-A or NF CMP 60116-2 preamplifiers and a NI PXI-5922 spectrum analyser two approximate measurements can be made. The NF CMP 60116-2 preamplifier has a voltage noise of 2.5 nV/$\sqrt{\text{Hz}}$ and an inherent current noise of 15 fA/$\sqrt{\text{Hz}}$. However due to the preamplifiers being independently powered their voltage noise is not cross-correlated. Current noise is inherently cross-correlated and cannot be avoided, but the inherent current noise in the preamplifier is too low to impact the measurement as the two-terminal resistance of the sample is only about 200 Ω. The NI PXI-5922 has a voltage noise floor of 3-4 nV/$\sqrt{\text{Hz}}$ between 50 kHz and 1 MHz. Since only one spectrum analyser is used the voltage noise from it will be cross-correlated across the signals, but only after the preamplifier signals are amplified.

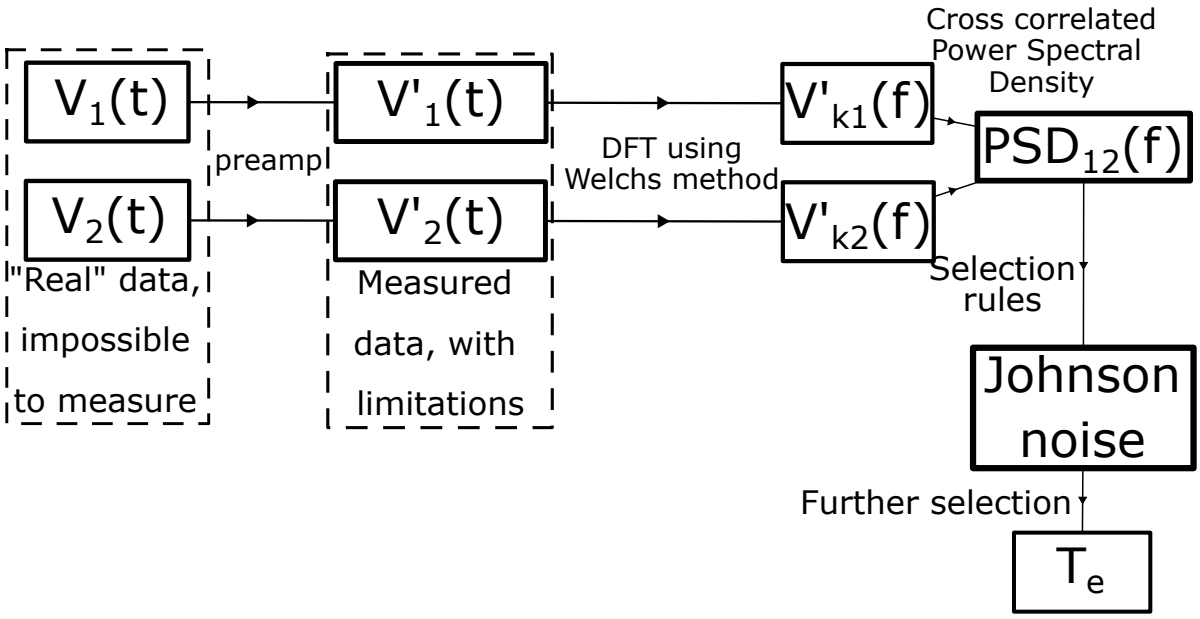

Figure 5.6: The processing flow from how the taken data gets processed to how the electron temperature is extracted. For both of the 'real' signals, given by $V_1(t)$ and $V_2(t)$, there is a continuous and infinite amount of data. These signals are made up of various contributions throughout the circuit including the sample of interest and noise from the wiring. The measured signals from the preamps, $V_1'(t)$ and $V_2'(t)$, are imperfect measurements of this data due to limitations on bandwidth and resolution. In addition the preamps will pick up another noise term from their power supply. The next step is to calculate the periodograms of these individual signals, reducing the resolution, but eliminating any spurious noise peaks in the data. Then the cross-correlated power spectral density is calculated, eliminating any noise term in the signals that are not correlated with each other, such as the noise from the preamp power supply and the noise from the separate wiring. To extract the Johnson noise from this cross-correlated signal the data from 200 kHz to 600 kHz is extracted. Then the mean and standard deviation are calculated, and any data points outside of one standard deviation of the mean is discarded before the mean is recalculated. Finally the new mean is used to calculate the associated electron temperature.

The two signals from the preamplifiers were taken over a period of 2-5 seconds and consist of approximately 2-5 million data points. The data is then divided into segments and the DFT is taken of the segments following Welch's method. The resultant set of segmented DFT's are then cross-correlated in order to calculate the cross-correlated power spectral density. This process is then repeated 100 times and averaged; Fig. 5.7 shows how the uncertainty of the electron temperature ΔT_e and the temperature T_e settles as a function of the number of measurements n taken. At this stage the first set of selection rules is applied, where after looking at the running average and running standard deviation of the data set it was found that the region between 200 and 600 kHz was the most appropriate for Johnson noise. Lower frequencies suffered from $1/f$ noise and higher frequencies had issues with roll-off. Once the Johnson noise has been extracted its mean and standard deviation are

calculated. The final selection rule is then to disregard all the data outside of one standard deviation and to recalculate the average noise. Finally the electron temperature is calculated using the newly calculated average noise. These steps are shown in Fig. 5.8 which shows the selection process of the power spectral density as a function of frequency in (a) and the binned histogram version of the same plot in (b). In the example shown the theoretical Johnson noise voltage rms is 1.62×10^{-10} V/$\sqrt{\text{Hz}}$, which compares favourably to the calculated value of $(1.6 \pm 0.3) \times 10^{-10}$ V/$\sqrt{\text{Hz}}$.

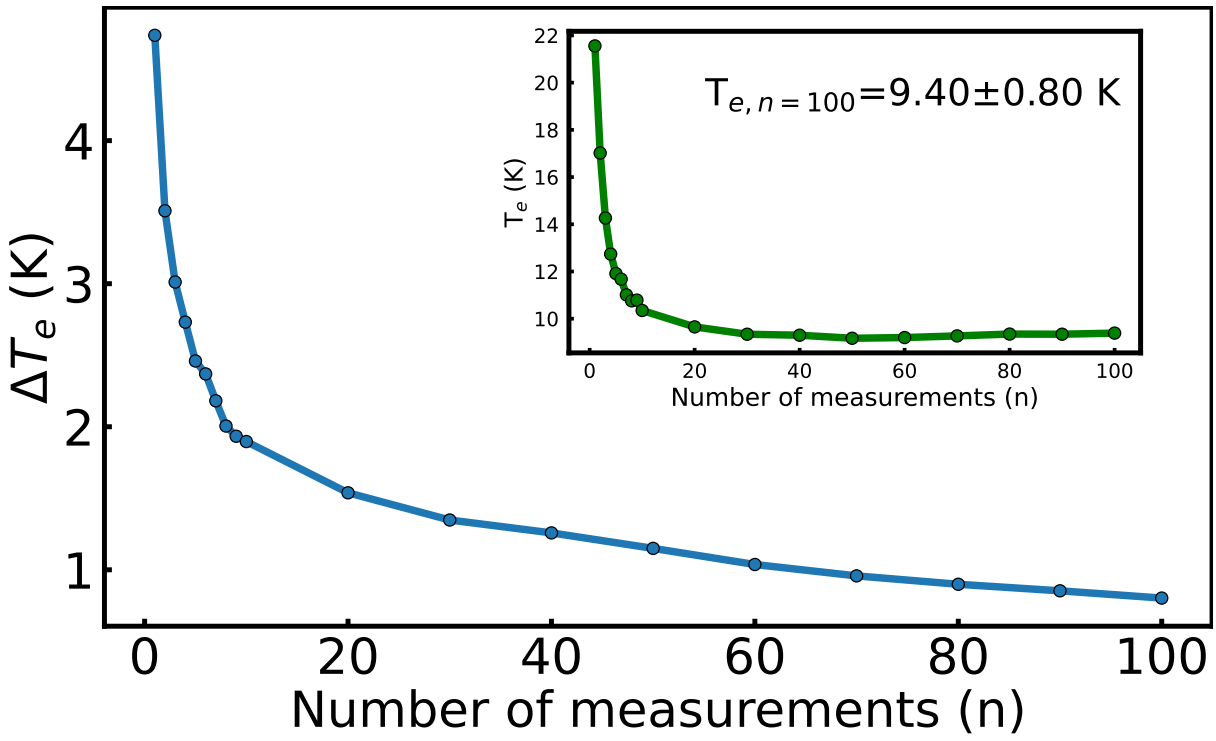

Figure 5.7: The uncertainty of the electron temperature ΔT_e as a function of the number of files n processed. At $n = 100$ the uncertainty has settled to 0.8 K, fitting a generic $1/f$ to the data shows that as n goes to infinity the uncertainty settles at 0.7 K. The inset shows the calculated electron temperature T_e over the same range; settling at $n = 80$. Increasing n would therefore have reduced ΔT_e, but at a significant cost to processing and with no further improvements for T_e.

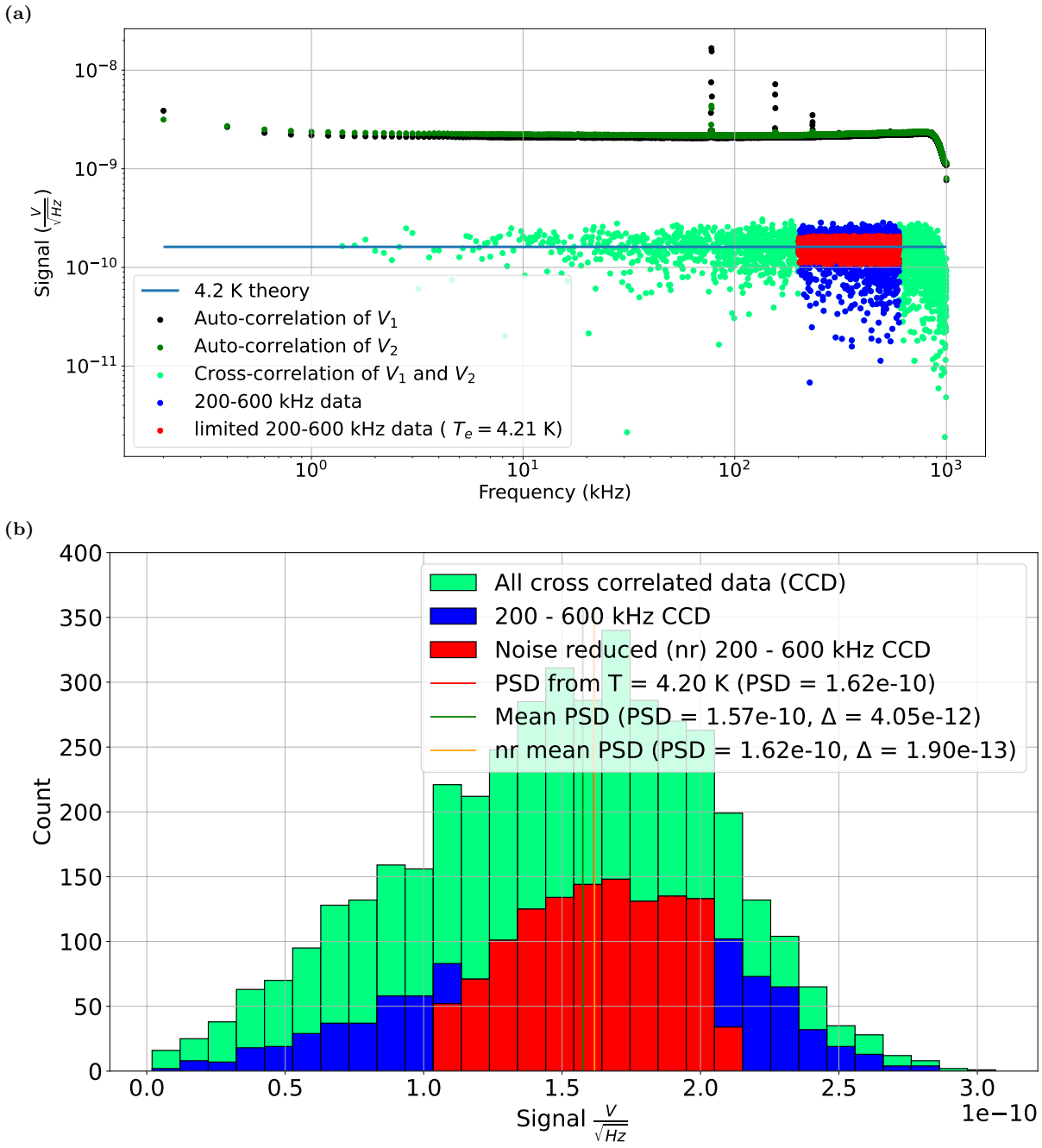

Figure 5.8: Noise processing example for a sample where $T_e = 4.2$ K and $R = 112.5\ \Omega$. (a) The measured noise spectrum S as a function of the frequency f. The black/ green data are the auto-correlated signals, the light green shows the entirety of the cross-correlated data, and the light blue shows the cross-correlated data in the 200-600 kHz range. Using the blue data the mean and standard deviation were calculated, and any data outside of one standard deviation was removed resulting in the red data. Finally using this red data the electron temperature is calculated using $S = 4k_B T_e R$. The horizontal line is the theoretical value of the Johnson noise at $T_e = 4.2$ K and $R = 112.5\ \Omega$. It was found that the calculated signal value of $(1.6 \pm 0.3) \times 10^{-10}\ \mathrm{V}/\sqrt{\mathrm{Hz}}$ compares favourably to the theoretical value of $1.62 \times 10^{-10}\ \mathrm{V}/\sqrt{\mathrm{Hz}}$. (b) The histogram version of the same data using the same colour scheme. In addition it also shows the rms voltage of the initial 200-600 kHz data and the limited version of the same data. The overlap between the theoretical value for 4.2 K is so close to the calculated value that they are hard to distinguish.

Chapter 6

Magnetohydrodynamics

6.1 Introduction

The advancement of molecular beam epitaxy has allowed for the creation of many novel semiconductor systems. One of these systems is the GaAs/AlGaAs-based two-dimensional electron gas (2DEG), most commonly shaped into Hall bars. A more recent development in this area has been the ability to suspend these structures [107], which are thought to be partially decoupled from the mesa and to have a reduced electron-phonon coupling [20]. The purpose of this chapter is to present the measurements performed on suspended and non-suspended 10 μm wide Hall bars, see Fig. 6.1, as a function of a DC heating current, and an applied perpendicular magnetic field, predominantly at a temperature of 4.2 K. These results will be compared with each other and a wider Hall bar in order to carefully study the impact of the width of the Hall bar. From this study a complex picture of interacting length scales will emerge, where the differential resistivity will, in some cases, decrease as the applied DC current increases. It will emerge that the narrow Hall bar can hide regimes that would otherwise be present, but that these regimes may be recovered upon the application of a perpendicular magnetic field. Lastly this chapter will greatly utilise cross-correlation Johnson noise thermometry established in Chapter 5 in order to relate the DC current to the much more useful electron temperature.

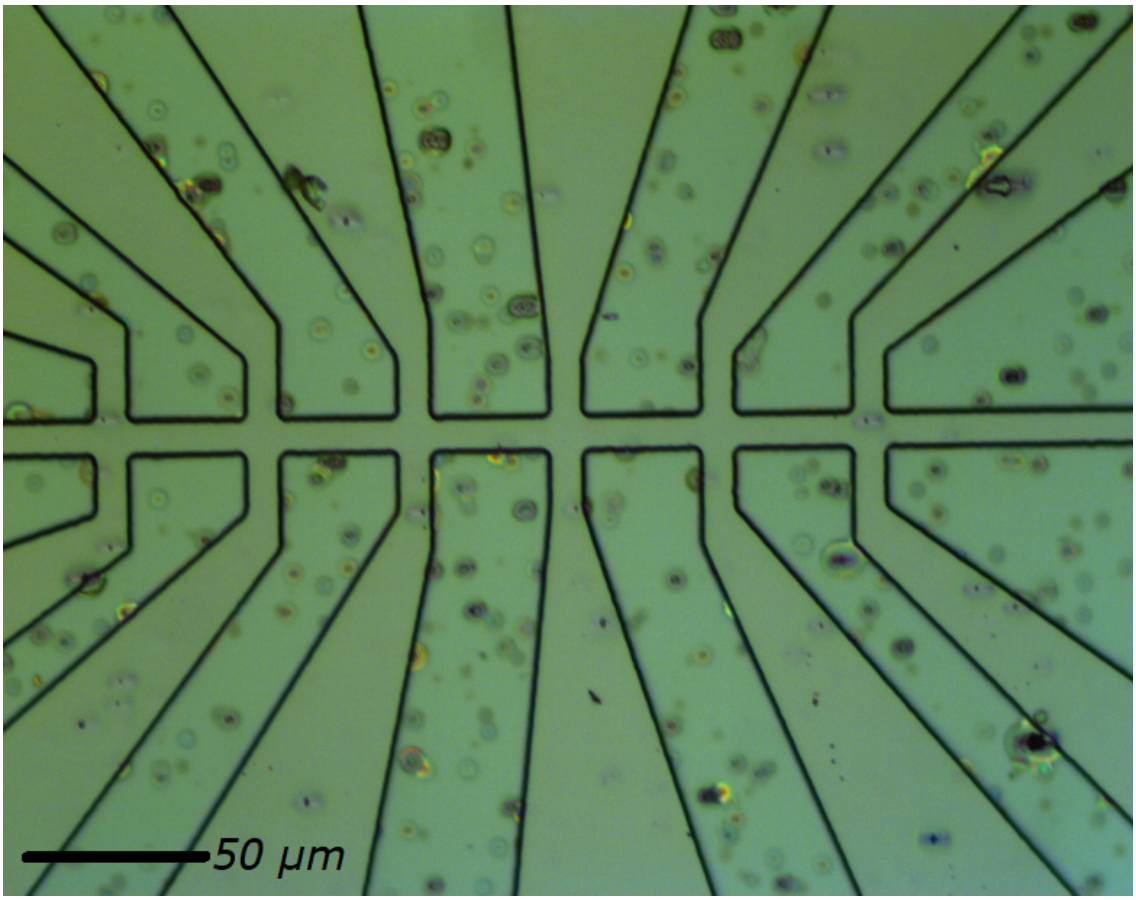

Figure 6.1: Optical microscope image of the N and S type Hall bar. The Hall bar and the voltage probes have been etched on the mesa as is seen by the black outline. The width of the Hall bar is approximately 10 μm and the pairs of voltage probes are 40 μm apart, meaning that the length/width ratio, or number of squares, between adjacent voltage probes is 4. The black spots are due to Ga spitting during MBE growth and they can cause extra scattering, depending on the size. Image source: Dr. Stuart Holmes.

6.2 Current heating

Differential resistivity measurements can be very useful as it enables measuring the resistance of a device as it is being heated with a DC current, i.e., changing the electron temperature. The aim of this section is to explain what differential resistivity is, how it heats a Hall bar and to perform basic differential resistance measurements on both narrow suspended and narrow non-suspended Hall bars with the ultimate aim of distinguishing suspended and non-suspended Hall bars. As previously mentioned, Ref. [20] reported seeing a difference even as high as 7 K, which opens the possibility of seeing a difference even when using a 4.2 K LHe dewar.

6.2.1 Differential resistance

The traditional electrical resistance measurement based on Ohms law, $V = IR$, is only one of two types of resistance measurements. The other type of resistance, which is usually called differential or dynamic resistance, is defined as the change in voltage response due to a change in the current i.e., $R = \frac{dV}{dI}$ [108].

In this chapter differential resistance measurements are performed by combining an AC and a DC signal as outlined in Fig. 6.2. The AC signal is given by $I_{AC} = I_0 \sin(\omega t)$, where I_0 is always 1 μA or less. Given that $f(I)$ is the form of the voltage response at a given current then the DC current I_{DC} response will be

$$V_{DC} = f(I_{DC}) \tag{6.1}$$

and the AC + DC current will be given by

$$V_{AC+DC} = f(I_{DC} + I_{AC}), \tag{6.2}$$

leading to a change given by

$$\Delta V = V_{AC+DC} - V_{DC} = f(I_{DC} + I_{AC}) - f(I_{DC}). \tag{6.3}$$

The change in current over this voltage interval is given by the AC current signal, so dividing both sides by the change in current gives a resistance,

$$R = \frac{\Delta V}{\Delta I} = \frac{V_{AC+DC} - V_{DC}}{I_{AC}} = \frac{f(I_{DC} + I_{AC}) - f(I_{DC})}{I_{AC}} \tag{6.4}$$

which in the case where $I_{AC} \ll I_{DC}$ is approximately equal to the definition of a derivative, meaning that the resistance measured is the differential resistance.

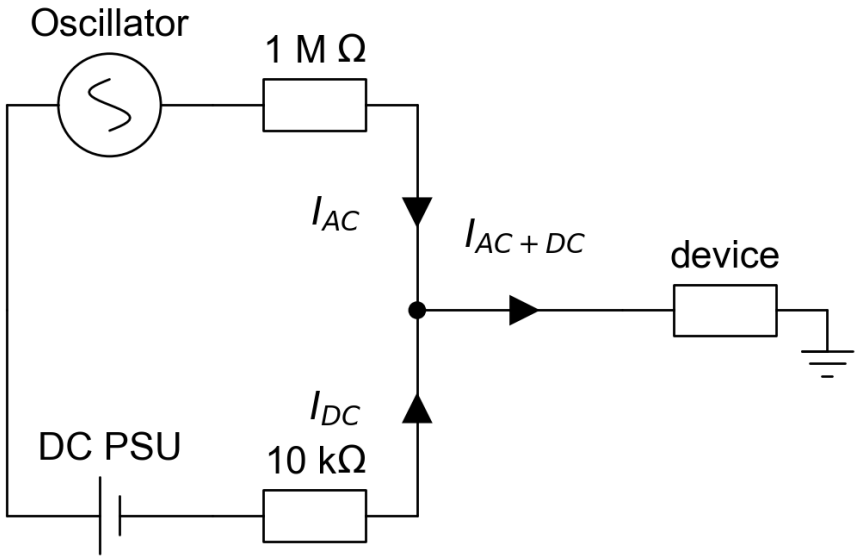

Figure 6.2: Setup for AC + DC current measurements. The AC current I_{AC} is provided by the internal oscillator of a 7265 lock-in amplifier. The DC source I_{DC} varies on the measurements taken, being either an IOTECH DAC for current sweeps or a collection of DC batteries for noise measurements. Typical resistances used for the AC and DC currents were 1 MΩ and 10 kΩ, respectively. The oscillator output has an amplitude of 1 V, which results in an AC current of 1 μA which does not cause Joule heating for T_L>1 K.

Note that throughout this chapter, R_{sq} will be used for the differential resistance per square, which is equivalent to the differential resistivity.

6.2.2 Current-heating background

The AC differential resistance $R = \frac{dV}{dI}$ uses a small AC current ($\leq 1\mu$A) to which a DC current I_{DC} is added, which provides Joule heating of the electrons to a temperature T_e above the lattice temperature T_L. The total power provided from the DC current will be given by

$$P_{in} = I^2 R = I^2 R_{sq} \frac{L}{W}, \tag{6.5}$$

where L is the length of the sample, W is the width of the sample, L/W is the number of squares, and R_{sq} is the resistance per square. This expression should be equal to the power lost by the electrons through momentum-relaxing collisions, which is given by

$$P_{lost} = \frac{Q}{\tau_{e-ph}}, \tag{6.6}$$

where Q is the energy transferred and τ_{e-ph} is the electron-phonon scattering time. Q is determined by the total number of electrons, their heat capacity C_v per electron[109], and the temperature difference ΔT via

$$Q = C_v LWn\Delta T. \tag{6.7}$$

Combining Eq. 6.6 and Eq. 6.7 gives

$$P_{lost} = \frac{LWnC_v\Delta T}{\tau_{e-ph}}. \tag{6.8}$$

Finally, combining Eq. 6.5 and Eq. 6.8 and rearranging for ΔT results in

$$\Delta T = \frac{I^2 R_{sq}\tau_{e-ph}}{nC_v W^2}, \tag{6.9}$$

giving a quadratic relationship between the change in temperature and the applied DC current.

6.2.3 Results and Discussion

By heating the narrow Hall bars with a DC current it was found that three regimes developed for both the suspended and normal Hall bars, see Fig. 6.3, which are consistent with the results from the original paper by de Jong [48]. These regimes, which appear as a function of the applied DC current, can be understood in terms of the relevant length scales [110]. At low currents the narrow Hall bars are in a ballistic regime where the width of the Hall bar is the limiting, i.e., smallest, length scale. As a result, when the DC current increases in this regime, the resistivity increases due to an increased amount of non-momentum-conserving collisions between the electrons and the rough boundary of the Hall bar. At medium currents there is a hydrodynamic regime where the resistivity actually decreases with increasing current, due to the electron-electron scattering length l_{ee} becoming the limiting factor. This phenomenon was first predicted by Gurzhi back in 1963 [47], as a result this negative resistivity with

an increasing current is sometimes referred to as Gurzhi flow. Electron-electron scattering in 2DEGs is predominantly normal-type scattering as opposed to Umklapp scattering and is therefore momentum conserving [111] as mentioned in Chapter 2. As a result, when the electron-electron scattering length becomes smaller than the scattering length of non-momentum-conserving collisions then the resistivity decreases. At higher currents, electron-phonon collisions become dominant and the resistivity starts increasing again [48].

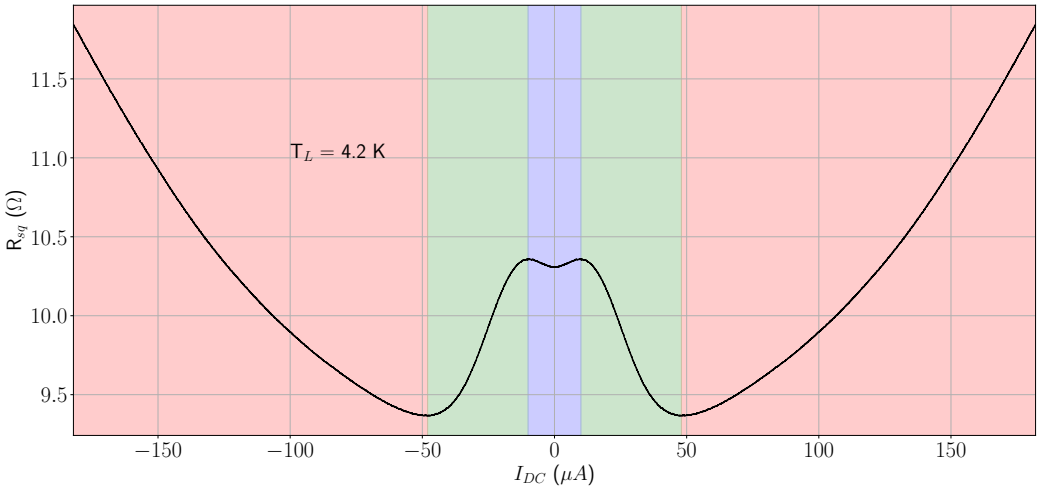

Figure 6.3: Differential resistivity of sample S2 as a function of applied DC current I_{DC}. Qualitatively these results were identical for the three other samples studied, one of which was suspended and the two others which were not. There are three distinct regions in this plot at low, medium, and high currents, which can be explained using the length scales Hall bar width w, e-e scattering length l_{ee}, and the electron-phonon scattering length l_{e-ph}. At low currents, blue, the width of the Hall bar is the smallest length scale so the system is in the quasi-ballistic regime. The collisions between the electrons and the boundary do not conserve momentum and therefore the resistance increases with the current. At medium currents, green, l_{ee} is the shortest length scale and, since electron electron scattering events are momentum-conserving and these scattering events replace the boundary-scattering events, the resistance decreases. At higher currents, red, due to the increasing amount of phonons, l_{e-ph} becomes the shortest length scale and the resistance starts increasing.

Fig. 6.4 shows normalised resistivity measurements of the suspended and non-suspended narrow Hall bars. Note that each of these curves is the average of two samples since they were very similar and represents the typical behaviour observed. The suspended curve has a much shallower hydrodynamic regime that ends at a lower DC current compared to the normal Hall bar. This could indicate that the suspended Hall bar is more sensitive to heating caused by I_{DC} due to the suspension [112]. However, it is difficult to make any definitive judgements due to the unknown temperature of the system, as the high currents used will

cause significant heating in the sample. In addition, accurate densities and mobilities of these samples are required in order to make further comments.

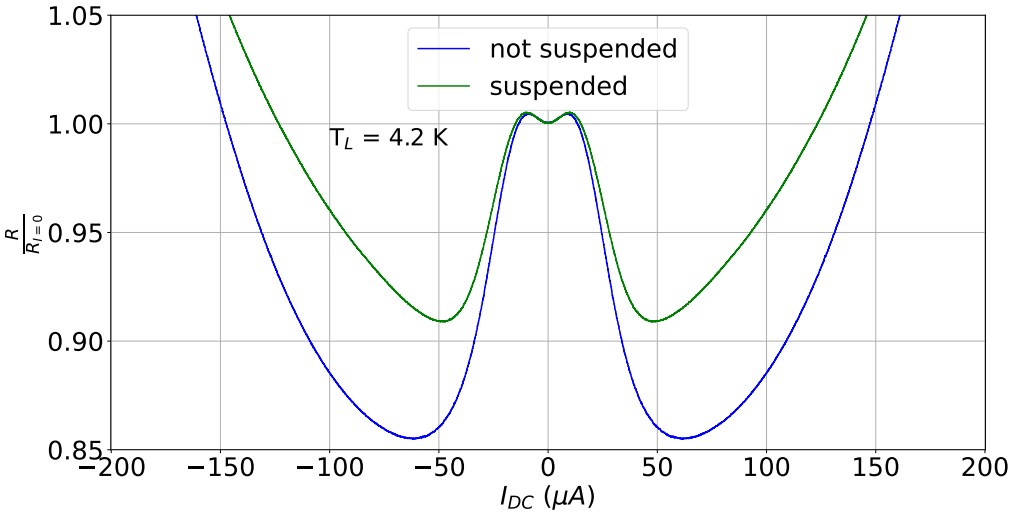

Figure 6.4: Normalised R versus I comparison of suspended and non-suspended 10 μm-wide Hall bars. The minimum in the resistance occurs at a lower current for the suspended Hall bars, which could be a result of the suspended structures being unable to dissipate as much heat as non-suspended Hall bars.

6.3 Magnetic field sweeps

In addition to performing Hall measurements to extract the mobility and the density of the 2DEG, the application of a magnetic field in narrow systems while performing longitudinal resistance measurements can also determine characteristics of the system, such as the actual 2DEG width, which may differ from the lithographic width due to depletion near the edges. It may also determine the specularity of the electron-boundary collisions [38] and measure the Hall viscosity of electron fluids in clean systems [51, 52, 53, 54].

6.3.1 Length scale in a magnetic field

The application of a magnetic field B perpendicular to the 2DEG introduces a new length scale, the cyclotron radius, which is given by

$$r_c = \frac{\hbar k_F}{eB}, \tag{6.10}$$

where $\hbar$ is the reduced Planck's constant, k_F is the Fermi wavevector, e is the electron charge, and B is the applied magnetic field. In a 2DEG, $k_F = \sqrt{2\pi n}$, resulting in [113]

$$r_c = \frac{\hbar\sqrt{2\pi n}}{eB}. \tag{6.11}$$

This length scale together with the width of the Hall bar W determines the behaviour of the longitudinal resistance as a function of the applied magnetic field and gives rise to two different regimes. At low magnetic field, when $\frac{W}{r_c} < 0.55$, the magnetic field causes an increase in the measured resistance caused by the Lorentz force pushing the electrons into the side of the Hall bar increasing the electron-boundary scattering. However, when $\frac{W}{r_c} > 0.55$ [38] then an increasing magnetic field decreases the longitudinal resistance as electrons get confined to the edges and diffusive backscattering is suppressed. At this point the system will recover its bulk resistivity, i.e. the resistivity expected of an infinite width Hall bar. At even higher magnetic fields, Shubnikov-de-Haas oscillations will be observed, but such high fields were not used in these measurements.

In addition, the drop in the measured resistance from zero magnetic field until $\frac{W}{r_c} \gg 0.55$ will also help determine the p parameter, which ranges from 0 to 1 corresponding to completely diffusive and completely specular boundary scattering respectively. The effective

collision time is determined from Matthiessen's rule:

$$\frac{1}{\tau_{eff}} = \frac{1}{\tau_0} + \frac{1}{\tau_b}, \tag{6.12}$$

where τ_{eff}, τ_0, and τ_b are the timescales associated with the effective collision time, the bulk collision time, and the mean time between diffusive backscattering events. This equation is equivalent to

$$\frac{1}{l_{eff}} = \frac{1}{l_0} + \frac{1}{l_b}, \tag{6.13}$$

in terms of the respective corresponding length scales as the velocities for all of these scattering events are equal. Each of these length scale will have an associated resistivity letting us rewrite the equation as

$$\rho_{eff} = \rho_0 l_0 \left(\frac{1}{l_0} + \frac{1-p}{W} \right), \tag{6.14}$$

where $l_b \approx W/(1-p)$ [38]. Note that the subscript 0 refers to the bulk value, which in this case is the value with a magnetic field applied, whereas the subscript eff refers to the value with no magnetic field applied. Therefore the p parameter relates the resistivity at zero magnetic field to that at moderate magnetic field and is the fraction of electron-boundary collisions which are momentum-conserving. If p has a value of 1 then all boundary collisions are momentum-conserving, i.e., the boundary is perfectly smooth, whereas a p value of 0 means that the boundary is perfectly rough. Rearranging this equation we can then measure p, which is a good measure of the roughness of the system, and compare it to the literature.

6.3.2 Results and Discussion

The longitudinal resistivity measurements performed on the narrow Hall bars, see Fig. 6.5, exhibit the expected double peak [50]. These peaks are consistent with a Hall bar width of 9 μm using Eq. 6.11, which is one micrometre less than what they were meant to be. Such results are expected since it is common for there to be some depletion near the edge of the Hall bar [114]. At strong magnetic fields, where the cyclotron radius is significantly smaller than all other lengths, the resistivity levels out at a lower value.

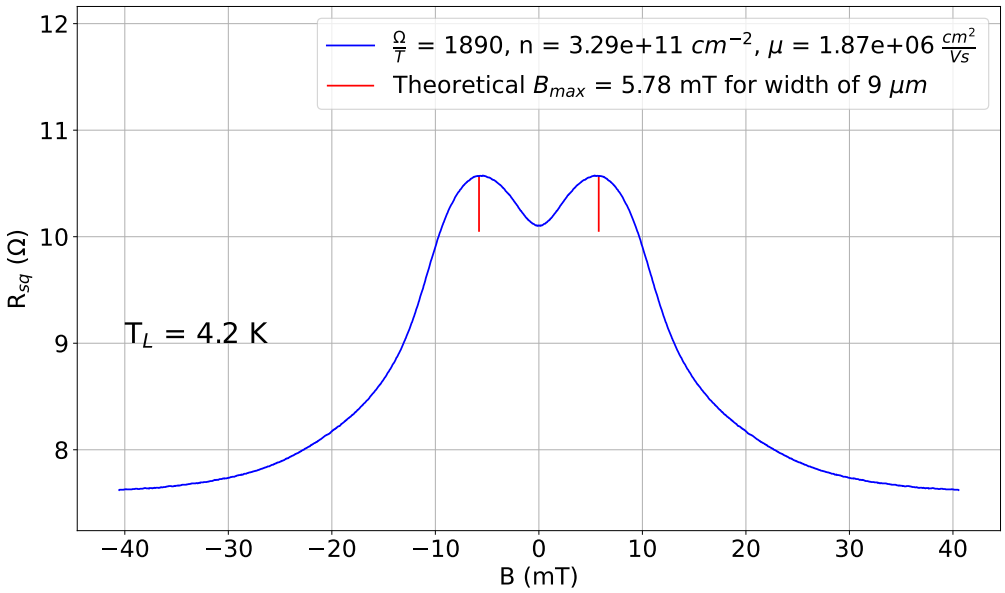

Figure 6.5: Longitudinal resistivity as a function of applied perpendicular magnetic field B for sample S2. Note that these measurements were repeated for one other suspended device and two other non-suspended devices but the results were qualitatively identical. Two peaks are observed at approximately $\pm$ 5.8 mT, which corresponds to a Hall bar width of 9 μm using $W = 0.55 \times r_c$, where W is the width and r_c is the cyclotron radius. This is in line with the expected 10 μm as there is likely to be some depletion near the edge of the Hall bar, reducing the functional width.

Using this data it is also possible to calculate the p value. Extrapolating the data seen in Fig. 6.5, the resistivity curve flattens out at $7.6 \pm 0.1\ \Omega$ and has an original value of 10.1 Ω. Rearranging Eq. 6.14 gives

$$p = 1 - \frac{\Delta\rho W}{\rho_0 l_0}, \tag{6.15}$$

where $\Delta\rho = \rho_{eff} - \rho_0$. For the data in Fig. 6.5 the value of p was estimated to be 0.88 ± 0.01, meaning that only 12% of the boundary-scattering events are diffusive, comparing favourably to other values in literature [38]. These results also help explain why the ballistic regime observed in Fig. 6.3 is so shallow. Most of the collision events conserve their momentum and there is only a small minority, that contribute to the increasing resistance.

6.4 Current sweeps at various magnetic fields

In the previous section we saw that upon the application of a magnetic field the longitudinal resistivity of the Hall bar would initially peak before dropping approximately 20-30% and recovering a lower bulk resistivity. This raises the question about how the application of a magnetic field interferes with the interplay of length scales seen in Sec 6.2.

6.4.1 Results and Discussion

Current sweeps at various magnetic fields were carried out for the N1 and S1 chips in order to see what the impact of the magnetic field was and if there were any differences between a normal Hall bar versus a suspended one. Figure 6.6 shows the relative resistivity curves of N1 at various magnetic fields including zero field, normalised to the resistivity at I_{DC}=0. Initially as the field is ramped up, the Knudsen peaks, signalling the transition from the ballistic to the e-e regime, appear to widen slightly and become more prominent, but qualitatively the regimes look similar to that of no magnetic field. However, as the magnetic field is increased further, the regimes change. Instead of having three distinct regimes, one of which has a decreasing resistance with an increasing I_{DC}, there are now two, both of which have an increasing resistivity as a function of the applied I_{DC}. The first regime, occurring at low I_{DC}, sees a very rapid increase, while the second regime sees a much slower increase as a function of the applied magnetic field. It is worth noting that this high I_{DC} regime bears some resemblance to the high I_{DC} regime seen in the cases of no magnetic field. The S1 device, seen in Fig. 6.7, is overall quite similar to the N1 device and exhibits the same transition from a three-regime system to a two-regime system as the magnetic field is ramped up. The rapid onset seen in both of these cases at high magnetic fields is indicative of a Bloch-Grüneisen transition [115]. However, if this is the case then an equivalent transition should be observed in a wider Hall bar of similar n and μ. To test this, a similar current-heating experiment, without the magnetic field, was run on the assessment chip for both of these samples, called A1. It was found, see Fig. 6.8, that a similar transition was observed in the assessment chip, reinforcing the idea that the observed transition in S1 and N1 was a Bloch-Grüneisen transition, which was initially hidden by the interplay between the length scales.

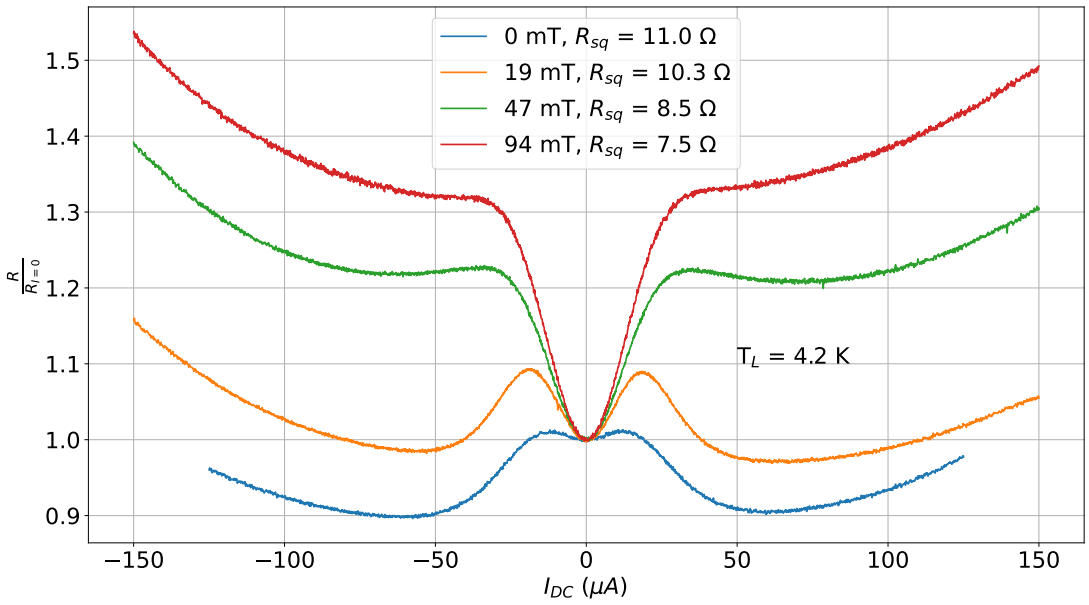

Figure 6.6: Normalised resistivity R_{sq} curves of illuminated N1, not suspended, as a function of applied DC current I_{DC} at different magnetic fields B. As the magnetic field increases the quasi ballistic regime disappears and makes way for a single transition between a low resistivity state and a high resistivity state, mirroring the observations made in a wider Hall bar with similar properties. This transition follows the characteristics of a Bloch-Grüneisen transition.

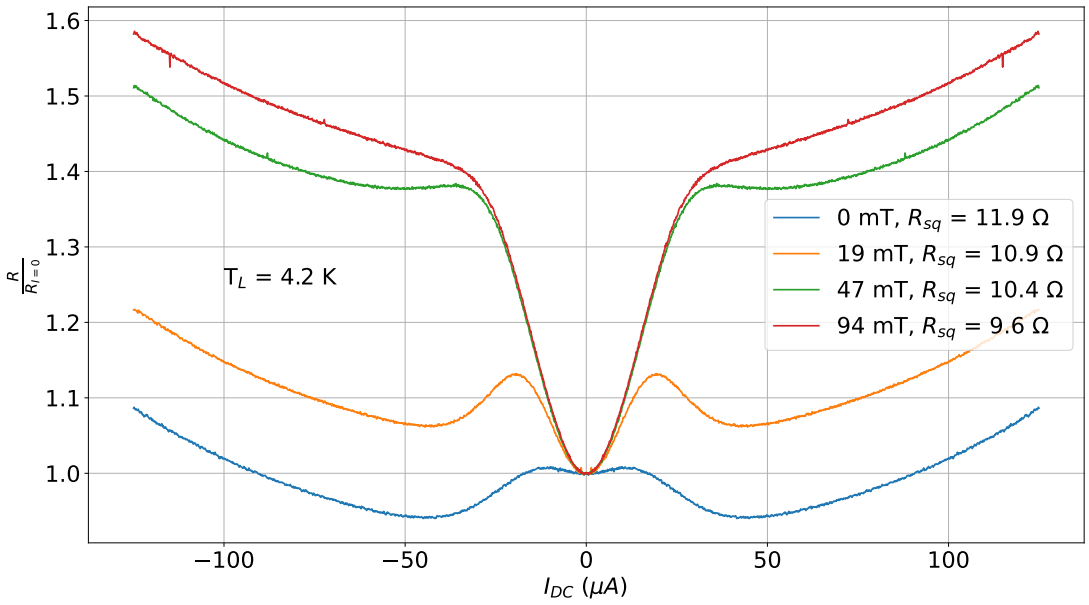

Figure 6.7: Normalised resistivity R_{sq} curves of illuminated S1, suspended, as a function of applied DC current I_{DC} at different magnetic fields B. As the magnetic field increases, the quasi-ballistic regime disappears and makes way for a single transition between a low-resistivity state and a high-resistivity state, mirroring the observations made in a wider Hall bar with identical properties. This transition follows the characteristics of a Bloch-Grüneisen transition.

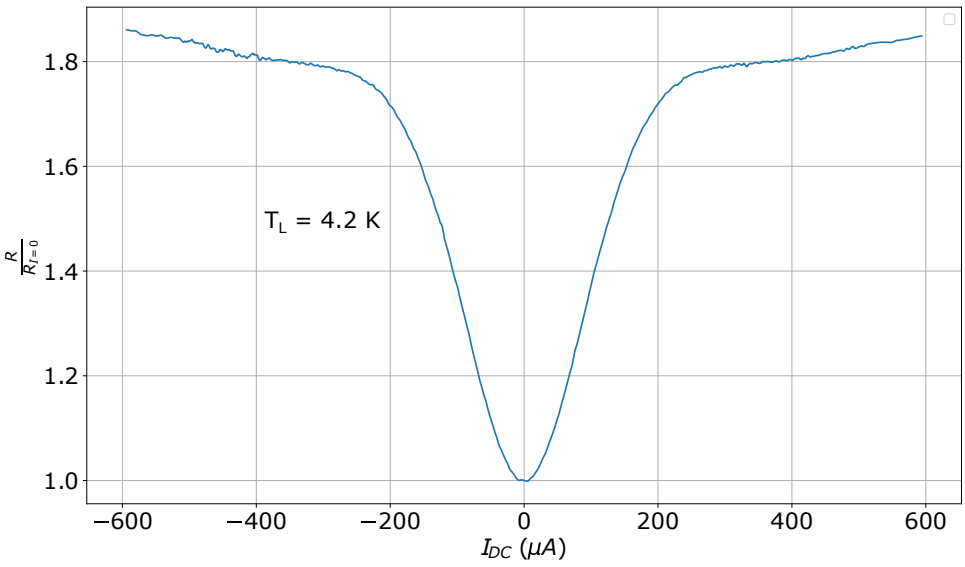

Figure 6.8: Normalised resistivity curve of the 80 μm-wide A1 Hall bar versus applied I_{DC}. At low currents until approximately 200 μA there is a rapid increase in the resistivity, which is indicative of a Bloch-Grüneisen transition. After the transition the increase in resistivity continues, but at a much slower rate, which is consistent with a normal electron-phonon regime.

6.5 Partially illuminated current and magnetic field sweeps

A complicated image of the interplay between various length scales is emerging. In the following section we show the effects of varying the density and mobility of the sample. This has an impact on the mean free path of the sample, which so far has not been relevant at small to medium currents. Pre-existing literature in this area [53, 54] has mainly focused on the viscosity of the electron flow at a given density. Some literature [55] has varied the density, but has remained in the viscous electron-electron regime. The following work starts out in the electron-phonon regime and transitions into the viscous electron-electron regime as the sample is illuminated. Assuming the length scale theory presented in other work [48, 38, 55] then there should not be a hydrodynamic regime present when the mean free path is less than the width of the Hall bar, but it should emerge as soon as the mean free path is made greater than the Hall bar width.

6.5.1 Results and Discussion

The results of the progressive illumination is shown in Fig. 6.9 for S2 where the differential resistance is measured as a function of the applied DC current at different magnetic fields. The difference between these two figures is a single illumination of the LED at 1.95 V for 250 ms. At $n = 2.14 \times 10^{11}$ cm^{-2} and $\mu = 1.13 \times 10^{6}$ cm^2/Vs for (a) and $n = 2.21 \times 10^{11}$ cm^{-2} and $\mu = 1.31 \times 10^{6}$ cm^2/Vs for (b) the corresponding mean free paths are 8.6 μm and 10.3 μm respectively. The known width of the Hall bar is $9 - 10$ μm meaning that these lengths are just below and above the width of the Hall bar, which is significant because a mean free path of just below the width of the Hall bar is likely to mean that there is no hydrodynamic regime at all whereas with a mean free path greater than the width of the Hall bar one would expect there to be a hydrodynamic regime. Figure 6.9a has no hydrodynamic regime at zero magnetic field, whereas Fig. 6.9b does. The hydrodynamic regime is very weak, but that is expected since the mean free path is only slighter larger than the width of the Hall bar. In addition, for both of the figures, when a magnetic field is introduced, then as soon as the cyclotron radius becomes the smallest length scale then a magnetohydrodynamic regime appears, which is associated with a drop in the measured resistance due to the increase of momentum conserving scattering events. This is consistent with the results in Section 6.4, where the hydrodynamic regime was completely destroyed once a sufficiently strong magnetic field was applied. At 8.3 μA and 10.6 μA for the more and less resistive results,

respectively, they both experience a transition from a lower-resistance to a higher-resistance regime where the results are equivalent regardless of the magnetic field strength. It is possible that this is the Bloch-Grüneisen transition. That would explain the sudden change in the resistance since the Bloch-Grüneisen transition has a much steeper temperature dependence than normal Joule heating [116] and why the results are all the same afterwards since e-ph scattering has become the dominant scattering mechanism.

(a)

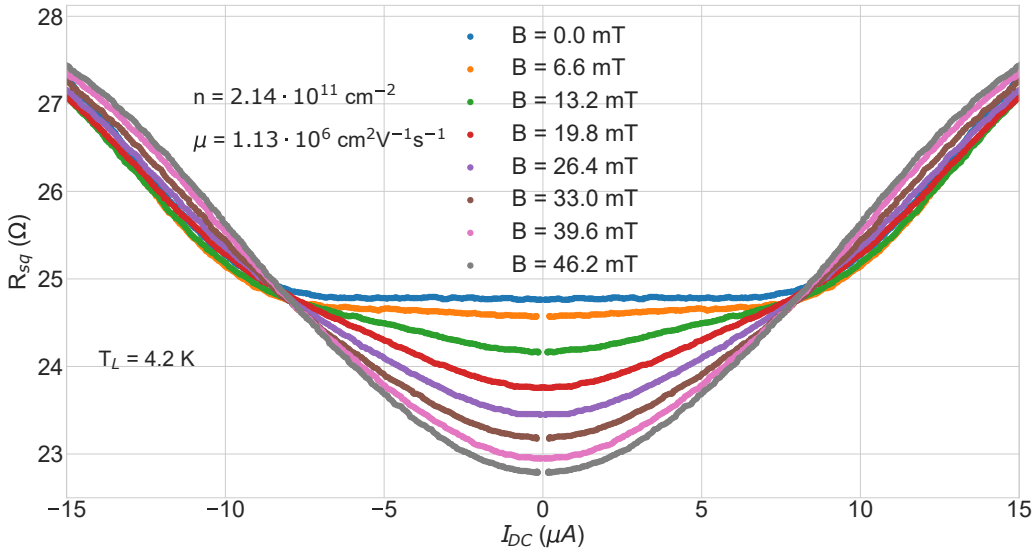

(b)

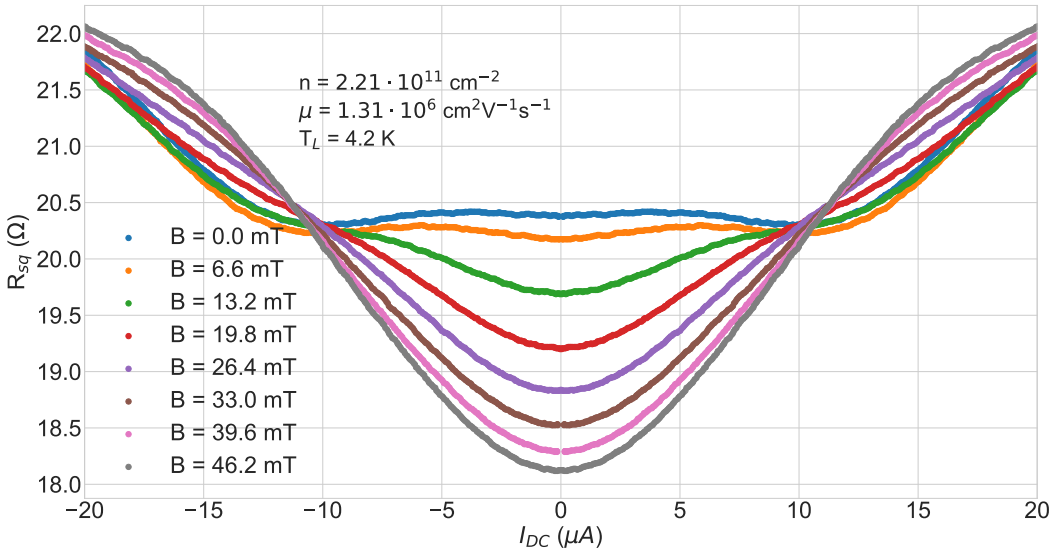

Figure 6.9: R_{sq} as a function of I_{DC} for partially illuminated S2 over 8 squares at an increasing perpendicular magnetic field. In(b) there has been another quick illumination after taking the data in (a). As the magnetic field increases the resistance of both sets of curves decreases, which is in line with the cyclotron radius becoming the dominant length scale. Where these plots differ is in the low-current regime with no magnetic field applied. In this regime (a) is completely flat whereas (b) shows an initial increase and decrease in the resistance. The associated mean free paths of these two sets of curves are 8.6 and 10.3 μm for (a) and (b) respectively, meaning that for (a) at no point is the width of the Hall bar less than the mean free path. As a result an interplay between the width of the Hall bar and electron-electron scattering length is unlikely, however for (b) this is narrowly not the case, resulting in a very weak hydrodynamic regime.

6.6 Cross-correlated noise measurements

The previous sections looked at the resistivity as a function of the applied DC current, which is related to an increasing electron temperature, see Sec. 6.2. However, in order to better understand these results and to properly calculate the associated length scales such as l_{ee}, it is necessary to measure the electron temperature as a function of the applied DC current. The aim of this section it to use the methodology described in Chapter 5 and the literature [117, 118] in order to establish the electron temperature. The setup for both the four-terminal resistance measurements and the noise measurements is shown in Fig. 6.10.

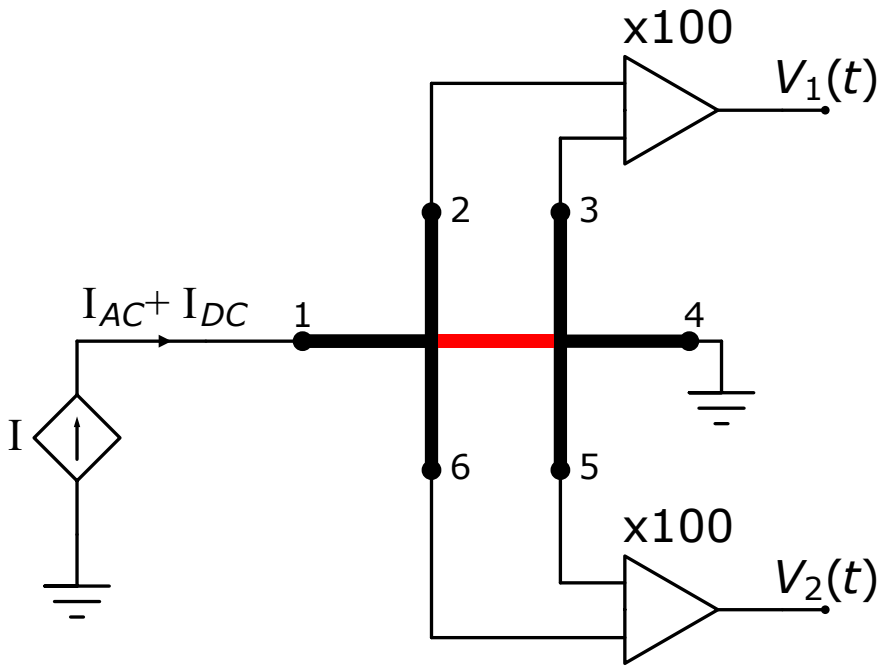

Figure 6.10: Setup for the four-terminal resistance and cross-correlation measurement. For the four-terminal measurements the AC current I_{AC} is set to 1 μA for a given heating current I_{DC}. The resistance is then measured across the red region only using either of the preamplifiers. For the cross-correlated noise measurements $I_{AC} = 0$, I_{DC} is provided by a shielded DC battery source, and the preamplifiers are independently powered. The resulting cross-correlated noise measurement is therefore only of the region highlighted in red, and does not include any other part of the Hall bar or wiring.

6.6.1 Results and Discussion

Using the cross-correlated Johnson-noise measurements, like the one shown in Fig. 6.11, it is possible to establish the relation between the applied DC current and the electron temperature for a specific sample as seen in Fig. 6.12 for the partially illuminated assessment chip. A second-order polynomial of the form $Ax^2 + 4.2$, motivated by Eq. 6.9, is then fitted to the data in order to extract any electron temperature given the applied current. Once the fit is known it allows for the creation of a plot of resistance versus electron temperature.

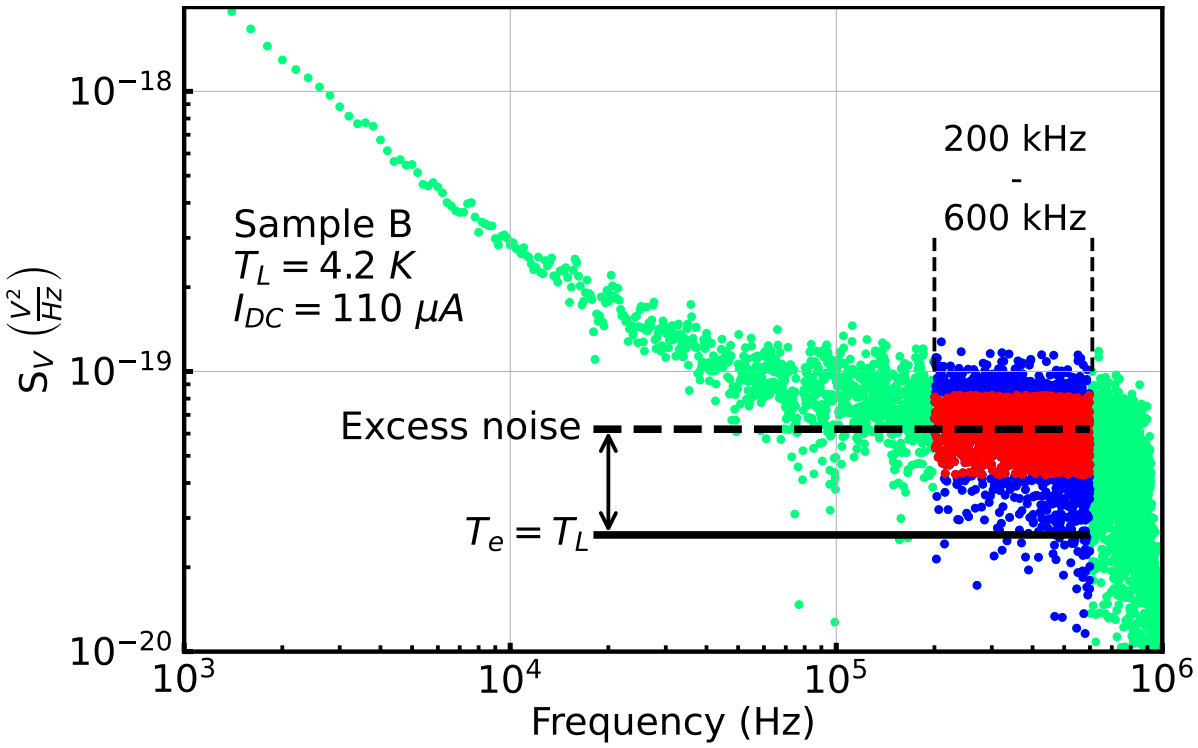

Figure 6.11: Johnson noise spectrum of the partially illuminated 80 μm wide A1 at 4.2 K as a function of frequency at a DC current of 110 μA. Light green points show the result of cross-correlating the two individual signals, settling at a noise floor slightly above that predicted for $T = 4.2$ K, illustrating how by applying a DC current the electron temperature increases. In order to extract the temperature, a flat region of the spectrum is chosen, in this case 200-600 kHz. For the 200-600 kHz region of data, the mean and the standard deviation are calculated. Using the mean and standard deviation all the data outside of one standard deviation is discarded. With the reduced 200-600 kHz data the mean and standard deviation are calculated again, shown in red, and used to calculate the electron temperature, which was found to be 9.4 ± 0.8 K.

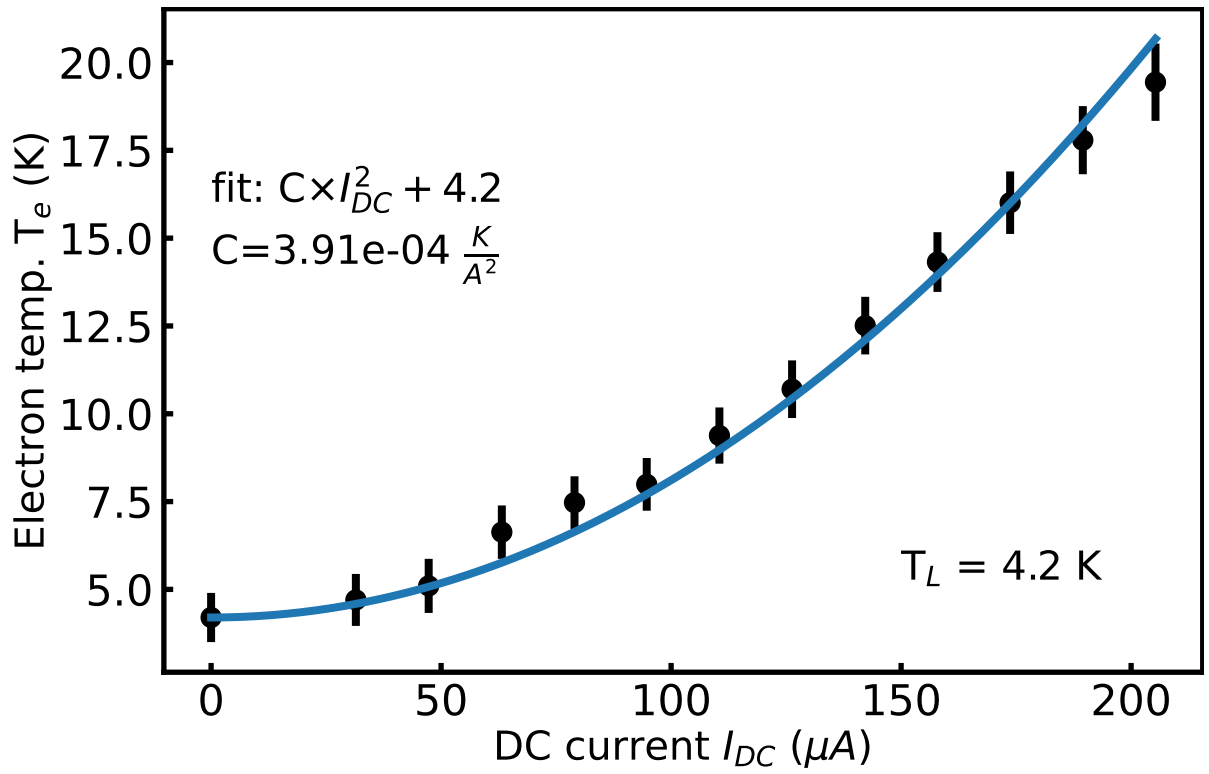

Figure 6.12: T(I) plot of A1 at an intermediate level of persistent photoconductivity with a quadratic fit in order to extract the electron temperature T_e at any given DC current I_{DC}. The electron temperature T_e is determined from the Johnson noise measurements, as a function of I_{DC}.

6.6.1.1 Fully illuminated narrow Hall bars

The cross-correlated Johnson noise methodology was first applied to the fully illuminated S2 and N1 as shown in Fig. 6.13 and Fig. 6.14 respectively. Qualitatively these curves look similar, but quantitatively the results are mixed. The R_{sq} minima for S2 and N1 are 27 K and 23 K respectively, which is not insignificant, but not sufficient given the uncertainties and the mobility/ density being slightly different between the two samples.

At the global R_{sq} minima the lattice heating caused by the DC current starts being significant, which gives rise to the increased resistance [42]. What is interesting to note is that the suspended Hall bar has a linear increase in the resistance in this regime whereas the normal Hall bar shows a higher-order increase as a function of the temperature. This is not completely unlike the results from Ref. [119] where phonon drag has a T^6 effect on the thermopower. Therefore the reduced dependence of the resistivity on the temperature could be a sign of reduced electron-phonon interaction caused by the suspension of the Hall bar.

Consider a truncated Taylor expansion

$$R(T) = R(T = 4.2\ K) + \frac{dR}{dT}\Delta T. \tag{6.16}$$

Using Eq. 6.9 it is observed that $R(T)$ depends on the electron-phonon scattering time τ_{e-ph}, meaning that a weaker R(T) dependence, all else being equal, means a reduced τ_{e-ph}. Ultimately more calibration points are required to draw a more definite conclusion at higher temperature, but it looks promising.

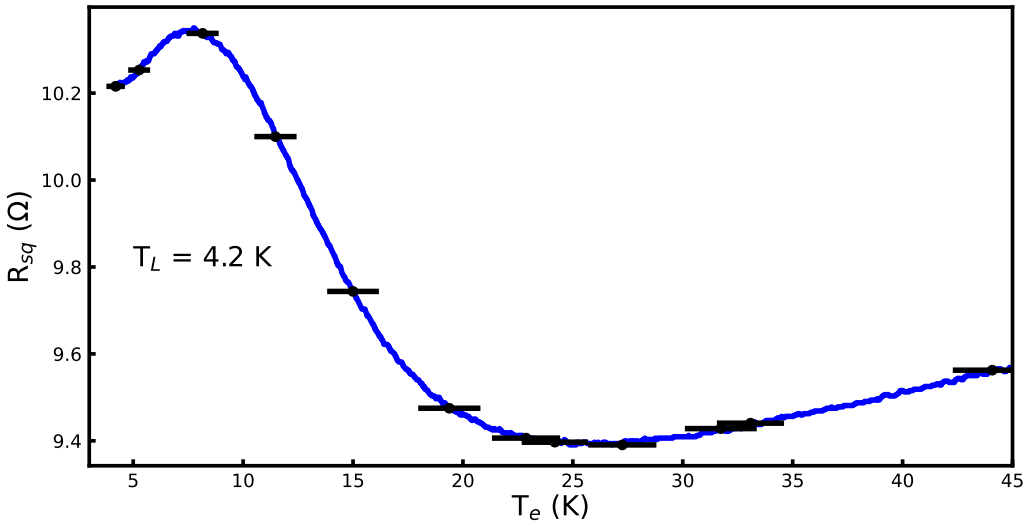

Figure 6.13: R_{sq}(T) as a function of electron temperature elevated by current heating of fully illuminated S2 (suspended). Blue is the converted data and black is the calibration points. A generic second-order polynomial was used for the fit. Initially a modest ballistic peak is observed, which is followed by a decrease in the resistance due to hydrodynamic electron flow. This drop in resistance represents a 7.8% reduction in the measured resistivity. The hydrodynamic minimum occurs at approximately 27 K and a linear R_{sq}(T) regime is observed at higher temperatures.

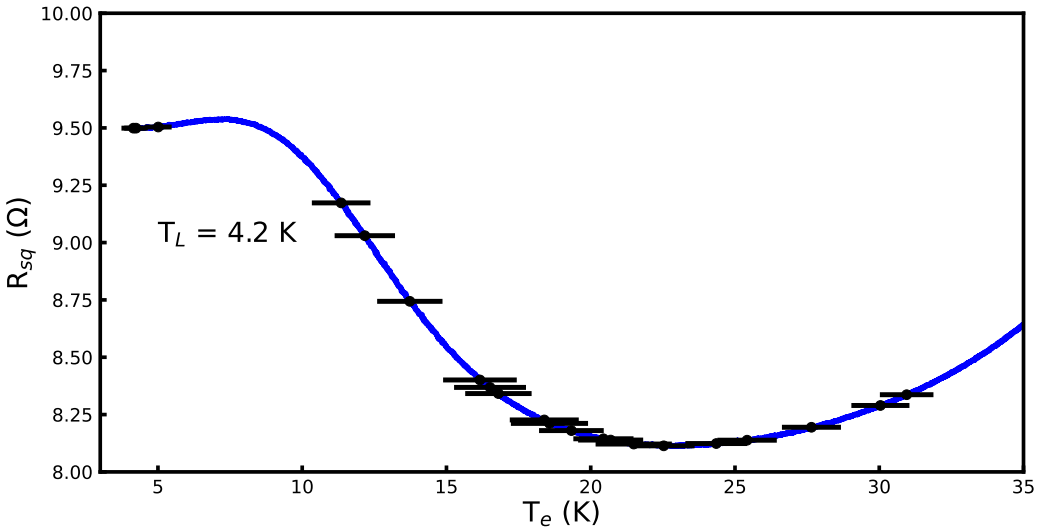

Figure 6.14: R_{sq}(T) as a function of electron temperature elevated by current heating of fully illuminated N1 (not suspended). Blue is the converted data and black is the calibration points. A generic second-order polynomial was used for the fit. A very weak ballistic peak is observed followed by a decrease in the resistance due to the hydrodynamic electron flow. This drop in resistance is about 15%, which is greater than what was found in the case of the suspended chip. The hydrodynamic minimum occurs at approximately 23 K and a quadratic R_{sq}(T) regime follows.

These results also allow for a better discussion of the conclusions from the de Jong and Molenkamp paper [48] as well as the l_{ee} prefactor as mentioned in Chapter 2. Now that the temperature is known from the cross-correlation measurements the l_{ee} scattering length and the temperature-corrected mean free path can be plotted as a function of the temperature together with the Hall bar width as shown in Fig. 6.15 for S2. Using the equation for the l_{ee} as provided by Ref. [43], with the original prefactor, is consistent with the conclusions from de Jong. At low temperatures the width of the Hall bar is the shortest relevant length scale, resulting in an increasing resistance as a function of the temperature. However at around 6-7 K, which is consistent with the observations of Fig. 6.13, l_{ee} becomes shorter than the width of the Hall bar. As a result the momentum-relaxing scattering events between the electrons and the boundary are replaced by momentum-conserving electron-electron scattering events, therefore reducing the resistance as a function of temperature. These results justify the use of the original prefactor to the equation for l_{ee}. A higher prefactor would lead to a decrease in l_{ee} as a function of the temperature which is inconsistent with the results. Additionally, Ref. [45] does note that due to the nature of the tunnelling experiments, from which many of these higher prefactors are derived, there could be contributions from both electrons and

holes, therefore increasing the prefactor. Since the measurements performed here are not tunnelling experiments, a lower prefactor is expected.

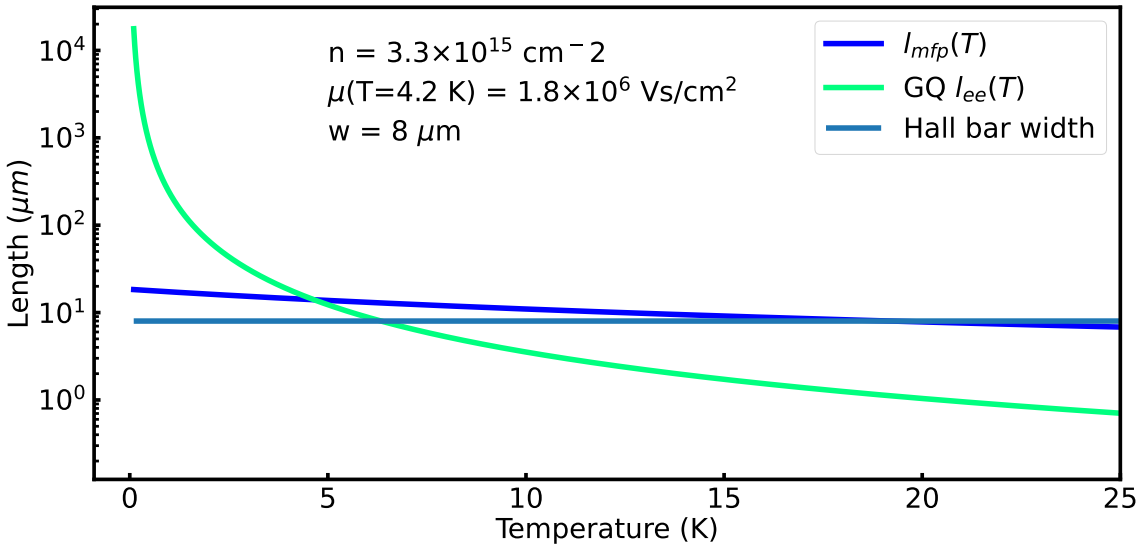

Figure 6.15: The electron-electron scattering length l_{ee}, temperature-corrected mean free path and the width of the Hall bar as a function of the temperature. Initially the width of the Hall bar is the shortest length scale, but as the temperature increases l_{ee} becomes shorter. The results of this is an initial increase in the resistance, but once l_{ee} is shorter, the resistance begins to drop until electron-phonon interactions become dominant. The l_{ee} plotted is based on the equation provided by Giuliani and Quinn (GQ) [43].

6.6.1.2 Fully illuminated wide Hall bars

The results of applying the cross-correlated noise methodology is shown in Fig. 6.16. The transition between the strong and weak $R_{sq}(T)$ dependences coincides with the Bloch-Grüneisen transition and appears consistent with the limited literature available [115]. Note that the Bloch-Grüneisen transition is a continuous transition [116], so it is difficult to pinpoint exactly when the transition occurs, but in the literature it is usually denoted towards the end of the steep $R_{sq}(T)$ dependence. The speed of sound is also highly directional in GaAs systems [120], meaning that there are technically many different possible Bloch-Grüneisen transitions. Here the transverse modes along (001) and the longitudinal modes along (100) as well as their mean, were used. The resulting velocity was found to be 3.40 km/s, 4.78 km/s, and 3.69 km/s for the transverse (001) mode, the longitudinal (100) mode, and their mean respectively. The mean was calculated using Ref. [121]. This average speed matches the transition observed very well, but it remains to be seen if the Bloch-Grüneisen transition is also the cause of the

behaviour seen in partially illuminated systems.

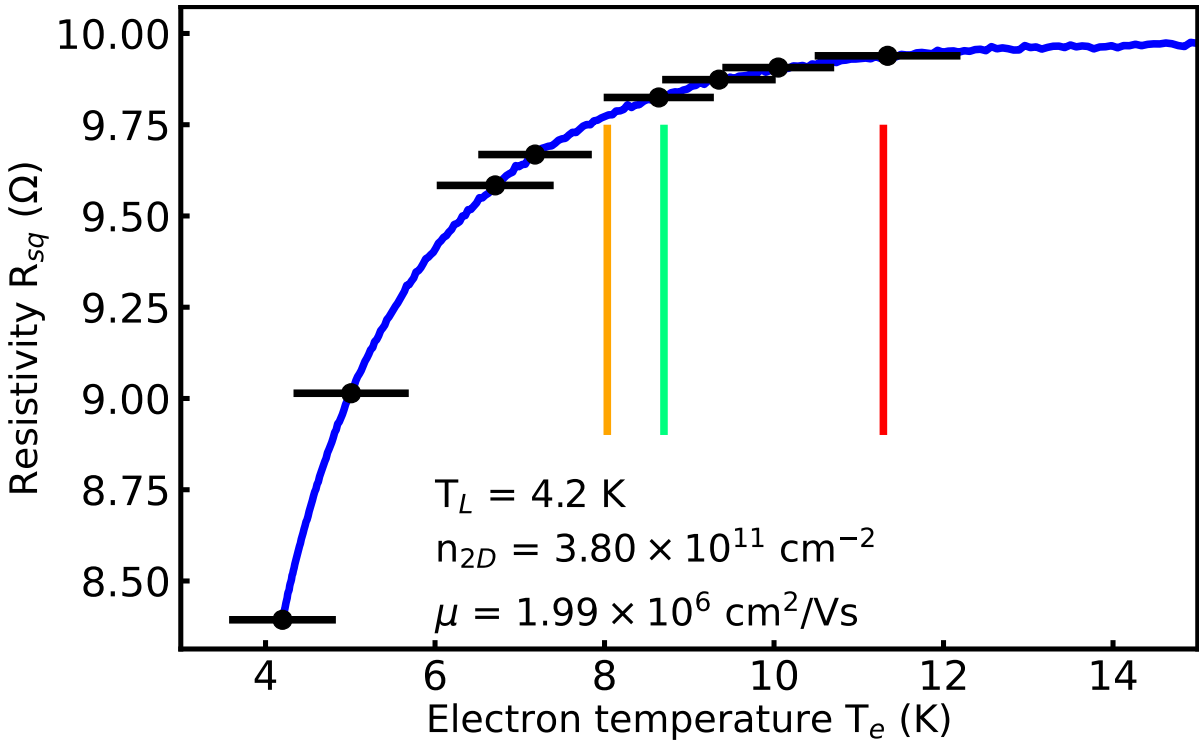

Figure 6.16: R_{sq}(T) as a function of electron temperature elevated by current heating of fully illuminated D1 80 micron wide Hall bar. The bullets are the calibration points where the Johnson noise was measured in order to change the x-axis from current I_{DC} to electron temperature T_e. All possible Bloch-Grüneisen transitions are shown as well as their mean. The orange, red, and light green vertical lines indicate the Bloch-Grüneisen transition T_{BG} for phonons in the transverse (001) direction, the longitudinal (100) direction, and their mean respectively. The mean of the possible transition temperatures align very well with the observed transition.

6.6.1.3 Partially illuminated Hall bars

Wide and narrow Hall bars were investigated using the noise technique for calculating the electron temperature, in order to put the results into context. Figure 6.17 shows the result of noise measurements on the partially illuminated N1 Hall bar, which was found to have a flat $R(I)$ dependence at low current similar to Fig. 6.9, with the potential Bloch-Grüneisen transitions. The transitions occur before the increase in resistivity making it unlikely to be the cause of the increase. The flat R(I) dependence at low currents is not typical for a 2DEG and its exact cause is not known, but could be the result of interplay between the length scales involved. At a density of 1.59×10^{11} cm^{-2} and a mobility of 7.82×10^5 cm^2/Vs it is possible to calculate the various length scales such as the temperature-corrected mean free path [122], the

electron-electron scattering length [43] and compare them with the width of the Hall bar. At 6 K, towards the end of the flat region, the electron-electron scattering length is the shortest length scale at 3.2 μm, followed by the temperature adjusted mean free path at 4.5 μm, with the longest length scale being the width of the Hall bar, at a constant 9 μm. However, it is worth noting that all of these length scales are comparable. One possible cause of the flat curve could be the e-e scattering length being the smallest length scale, meaning that when the electron temperature is raised by the DC current, the main increase in scattering events occurs between electrons and other electrons, leading to little heat being transferred between the electrons and the lattice. If the heat that is being transferred is then quickly being dissipated, then the increase in lattice temperature will be minimal. Additionally, the flat regime is only observed below the average Bloch-Grüneisen transition. Due to limitations on e-ph scattering in this regime, especially momentum-relaxing e-ph scattering events [123], the energy dissipated in the lattice will be minimal. This line of reasoning is speculative, but has similarities with the original argument made by de Jong [48]. Instead of an interplay between the e-e scattering length and the width of the Hall bar, it is an interplay between the e-e scattering length, the width of the Hall bar and the mean free path that is enabled by the Bloch-Grüneisen limitations on scattering. If this holds true then there are two important implications. The first is that if the Hall bar is wider, then the flat region should disappear, because it will proportionately increase the amount of e-ph scattering, leading to additional lattice heating, which in turn leads to more phonons and ultimately more momentum-relaxing scattering. The second implication is that as soon as the mean free path is raised above the width of the Hall bar, then the classical hydrodynamic regime should return. Both of these cases hold, as can be seen in Fig. 6.18 and Fig. 6.14 for the first and second implications respectively.

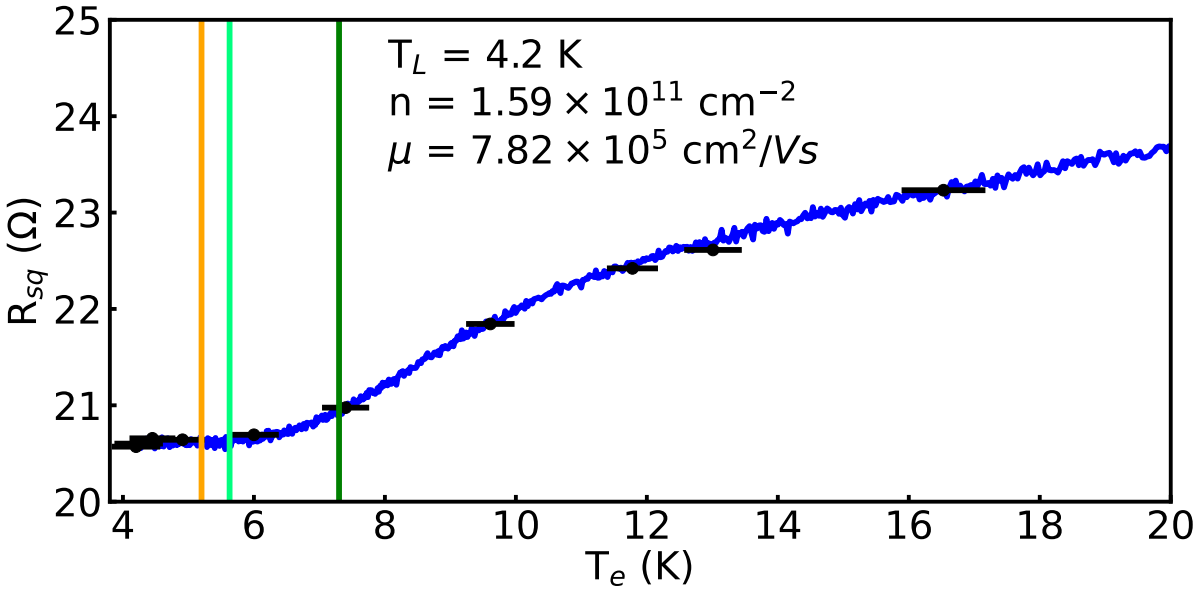

Figure 6.17: R_{sq}(T) as a function of electron temperature elevated by current heating of partially illuminated N1 (not suspended) with a density of 1.59×10^{11} cm^{-2} and a mobility of 7.82×10^5 cm^2/Vs. Note that these results were generic for both suspended and non-suspended Hall bars. Blue is the converted data and black is the calibration points. A generic second-order polynomial was used for the fit. The orange, green, and light green vertical lines indicate the Bloch-Grüneisen transition T_{BG} for phonons in the transverse (001) direction, the longitudinal (100) direction, and their mean, respectively. The transition observed in the resistance as a function of temperature is in some agreement with the potential Bloch-Grüneisen transitions.

Fig. 6.18 shows the results of the partially illuminated D1 sample. Unlike the previous results for fully illuminated D1 sample in Fig. 6.16 where one clear transition was observed, there appear to be two transitions present; one for the transverse (001) phonon mode and one for the longitudinal (100) mode. These results are promising, as the separate phonon modes have never been observed previously in a Bloch-Grüneisen transition.

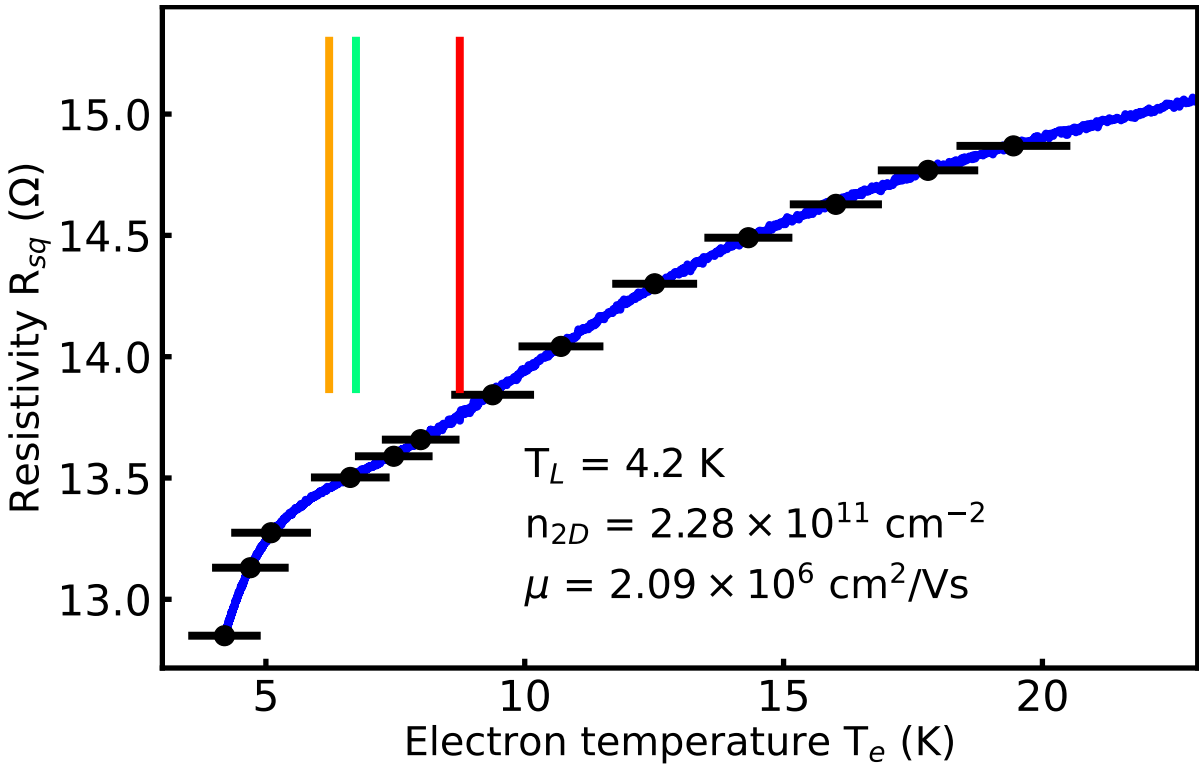

Figure 6.18: R_{sq}(T) as a function of electron temperature elevated by current heating of partially illuminated 80 μm wide A1 with a density of 2.28×10^{11} cm^{-2} and a mobility of 2.09×10^6 cm^2/Vs. Both possible Bloch-Grüneisen transitions as well as their mean have been included. The orange, red, and light green vertical lines indicate the Bloch-Grüneisen transition T_{BG} for phonons in the transverse (001) direction, the longitudinal (100) direction, and their mean respectively. There appear to be two transitions present in this data. The first one aligns well with the transverse (001) phonon mode whereas the second one seems to occur close to the longitudinal (100) phonon mode. Separate Bloch-Grüneisen transitions have never been observed, and it could be that the increased inhomogeneity of the partially illuminated sample is sufficient to separate them.

6.7 Fridge run

The essential missing piece up to this point is a fridge run where a wider variety of lattice temperatures can be investigated in order to study the effect of the lattice temperature on the hydrodynamic picture. In addition lower temperatures have only briefly been investigated in the literature [48, 53, 54, 55, 56]. The work presented here goes down to approximately 0.7 K and illustrates the effect of changing the lattice temperature on the hydrodynamic regime in both the fully illuminated and partially illuminated scenario.

Note that this fridge run would not have been possible without the contribution of Dr Aditya Jain who provided virtually all the technical assistance.

6.7.1 Results and Discussion

The differential-resistivity current sweeps at zero magnetic field can be seen in Fig. 6.19 at various temperatures between 3.91 K and 0.97 K. All temperatures show the same three regimes as a function of the applied DC current: an initial ballistic regime, a hydrodynamic regime, and finally an electron-phonon regime. Where they differ is in how pronounced these regimes are at different temperatures. At 3.91 K the ballistic regime only leads to a 0.2 Ω increase in the resistivity, whereas at 0.97 K the increase is 0.6 Ω. The hydrodynamic regime on the other hand does not see a significant change, only going from a change of 1 Ω to 1.2 Ω as the lattice temperature decreases, suggesting a slightly stronger hydrodynamic regime as the temperature decreases. In the e-ph regime all the various curves start to converge. Another interesting observation is that the DC current where one regime transitions into another does not appear to change appreciably as a function of the lattice temperature. One might expect that, as the lattice temperature decreases, the transitions should increase as a function of the applied current.

All of these observations can potentially be understood in terms of the length scales involved. As the lattice temperature decreases, the width of the Hall bar does not change, but the e-e scattering length and the mean free path increase [124, 44]. Therefore the initial regime becomes even more ballistic as the lattice temperature decreases. This also has the side effect of making the ballistic regime more momentum-relaxing since electron-boundary scattering events do not conserve momentum [38], thus at the transition from the ballistic to e-e scattering regime the electron temperature should be the same for all the different lattice temperatures. For the same reasons, the hydrodynamic regime is more or less unchanged at the different lattice temperatures. If the electron temperature is the same, then the electron-

electron scattering length is the same as well, ultimately leading to a hydrodynamic regime that is the same up to an offset. Finally in the electron-phonon regime the traces for all the different lattice temperatures begin to converge; this is a result of the current heating becoming so significant that any small difference in the lattice temperature is negligible. Ultimately this entire argument hinges on the electron temperature being the same regardless of the initial lattice temperature when the transition from the ballistic regime to the hydrodynamic regime occurs. Proving this definitively would be difficult, as the cross-correlated Johnson noise measurements would not work as well on a dry fridge, due to higher resistance wiring leading to an increase in the noise floor on the preamps and other sources of noise, particularly from vibrations [125].

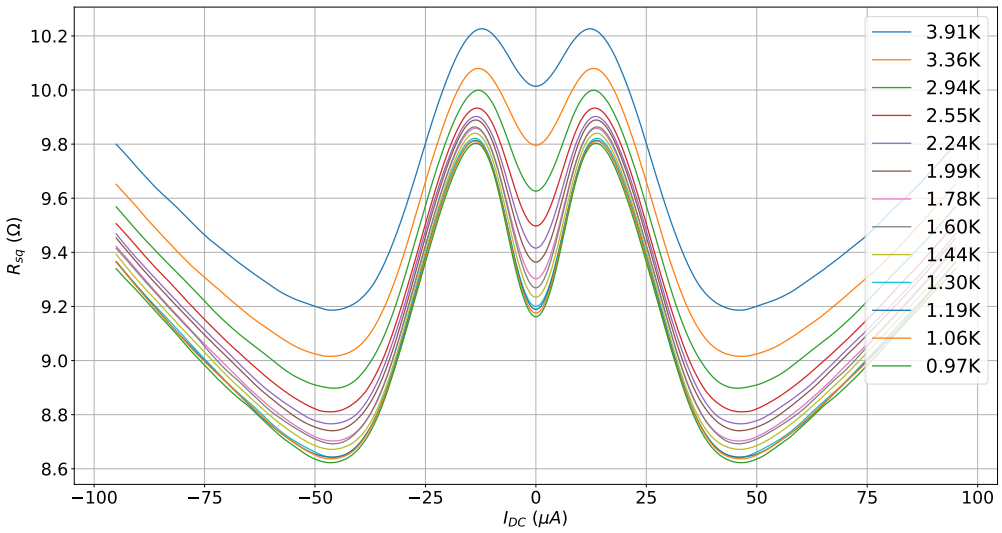

Figure 6.19: S2 differential resistivity current sweeps at various lattice temperatures. As the temperature increases there is a clear increase in the measured resistivity at all currents. The most interesting observation is how the resistivity changes over the ballistic regime at different lattice temperatures. As the temperature decreases, the change in resistance observed in the ballistic regime increases dramatically, meaning that the regime is becoming even more ballistic. The hydrodynamic regime does not see a significant difference in the resistance at different temperatures, but the transition from the hydrodynamic regime to the diffusive regime does. The resistance at the point of the transition from the hydrodynamic regime to the diffusive regime increases dramatically with temperature, suggesting a weakening hydrodynamic regime. Once in the diffusive regime the temperatures traces starts converging since the current heating dominates.

The same differential-resistivity current sweeps but with a magnetic field can be seen in Fig. 6.20 at various temperatures between 3.78 K and 0.81 K. As the lattice temperature decreases, the potential Bloch-Grüneisen transition becomes more apparent. The thermom-

etry for the fridge stopped being reliable around 5 K so it was not possible to increase the temperature up to the Bloch-Grüneisen temperature to see if the transition completely disappeared. However using the data presented it is possible to extrapolate the temperature where the transition would disappear. By looking at how the resistance increases as a function of temperature at $I_{DC} = 0$, where $T_L = T_e$, and at $I_{DC} = 50$ μA, after the transition, it is possible to calculate where they will be equal as the $I_{DC} = 0$ data increases much faster than the $I_{DC} = 50$ μA data. Carrying out this procedure, with a quadratic fit which matched the data very well, it was found that the two resistances will be equal between 7.8 and 9.7 K. The mean Bloch-Grüneisen temperature for this system is 9.12 K, which is in good agreement with the extrapolated crossover temperature. Ultimately, this further reinforces the observations made previously that by applying a sufficiently strong magnetic field to a narrow Hall bar it recovers the wide Hall bar behaviour and not just its bulk resistivity.

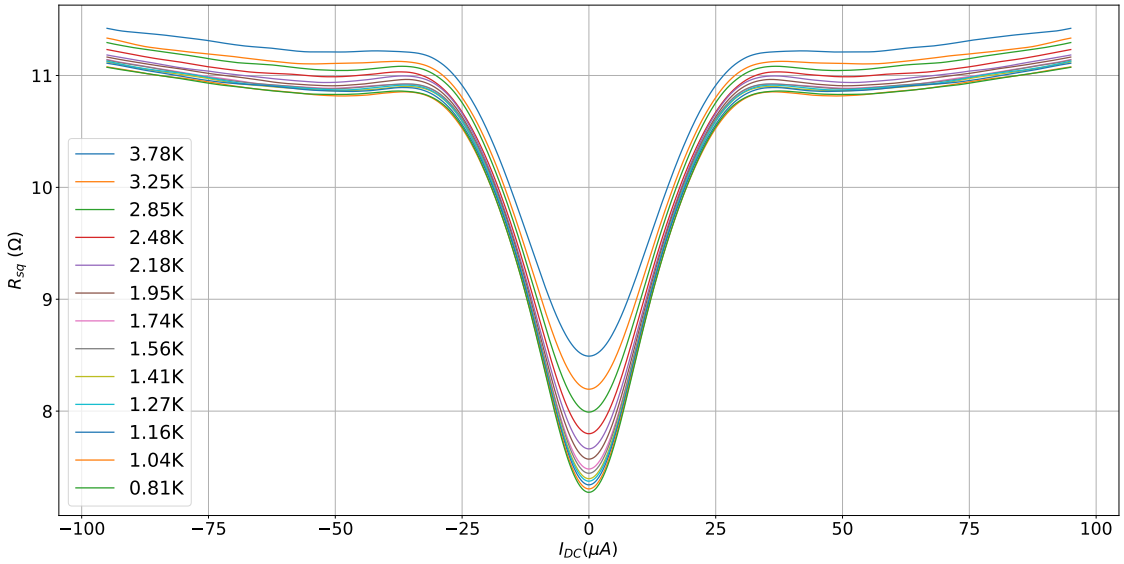

Figure 6.20: S2 differential resistivity current sweeps at various lattice temperatures at a magnetic field of 75 mT. As the temperature decreases the resistivity decreases as well, but this effect is more prominent around $I_{DC} = 0$, leading to a more prominent transition as the temperature decreases. These results make sense if the transition observed is the Bloch-Grüneisen transition because a lower initial temperature means that the lattice heating required will be greater. However the transition is complete by about 30 μA for all temperatures, meaning that a steeper transition is required, which is what is observed.

6.8 Summary

The initial aim of this chapter was to investigate suspended and non-suspended narrow Hall bars, in order to determine if there was a quick and easy way to determine if the Hall bar was suspended. Previous work in this area [20] found some potential differences in how the resistivity changed when heated, but the literature available was limited. Inspired by this, differential resistivity measurements were taken of both suspended and non-suspended Hall bars in order to see if there was a difference. The result, shown in Fig. 6.3, showed how under the right conditions the differential resistivity decreased as the sample was heated. These results, universal for all narrow Hall bars investigated, could be understood in terms of the electron-electron scattering length becoming the shortest length in the system and replacing momentum relaxing scattering events [48]. However some differences were found between the suspended and non-suspended Hall bars as shown in Fig. 6.4 where the hydrodynamic regime of the suspended Hall bars are reduced.

The next step was to introduce a magnetic field. Pre-existing literature [38] had shown how the introduction of a magnetic field would introduce another length scale into the system, but no work existed on how this would interact with the changing length scale caused by current heating. The main results of this can be seen in Fig. 6.6 and Fig. 6.7, where, upon the application of a sufficiently strong perpendicular magnetic field, the three regimes observed previously make way for two distinct regimes, both where the differential resistivity increases as a function of the applied magnetic field. It appears that the interplay between the width of the Hall bar and the electron-electron scattering length hid a Bloch-Grüneisen transition in the narrow Hall bars. The same general behaviour was also seen in the 80 μm wide assessment Hall bar, see Fig. 6.8, based on the same wafer as the narrow Hall bars. Some literature already exists on the Bloch-Grüneisen transition in Hall bars [115, 116], but it is limited and lacked primary thermometry.

The Bloch-Grüneisen transition also depends on the square-root of the density of the system. In order to better understand if the transition observed was Bloch-Grüneisen, the same devices as studied previously was partially illuminated, in order to change the density and mobility of the system while the width remained constant, thus changing the electron-electron scattering length and the mean free path. The results of these experiments were mixed. No definitive difference was found between the suspended and non-suspended Hall bars, see Fig. 6.9. However, it was found that at low densities a flat regime existed at low currents. This regime disappeared as soon as the mean free path became greater than the width of the Hall bar, making way for the hydrodynamic regime seen previously. It is not

entirely known why the resistivity is so flat in this regime, but it is speculated that it is a result of an interplay between all the length scales and the momentum-conserving nature of collisions prior to the Bloch-Grüneisen transition.

Penultimately, a primary thermometry technique, based on cross-correlated Johnson noise thermometry, was developed. This method has been used previously [126, 127, 128], but not in order to investigate the Bloch-Grüneisen transition. Using this technique it was possible to calculate the excess noise, see Fig. 6.11, in order to extract the electron temperature at a given DC current. With this technique, the narrow Hall bars were assessed and it was found that there does appear to be a difference in the τ_{e-ph} scattering length of the suspended and non-suspended Hall bars. In addition, it was also found that the suspected Bloch-Grüneisen transition observed in wider Hall bars occurs at the Bloch-Grüneisen temperature, thus reinforcing the idea that what is being observed is the Bloch-Grüneisen transition. The cross-correlation technique was also used on the partially illuminated samples, including one of the samples that experienced a flat resistivity, see Fig. 6.17, where it was observed that the flat regime ended at a temperature corresponding to the Bloch-Grüneisen transition, thus giving credence to the idea that the greater amount of momentum-conserving collisions observed prior to this transition is the cause of the flat resistivity.

Finally, a fridge run was performed in order to see the effect of varying the lattice temperature. Differential resistivity measurements were performed on a narrow suspended Hall bar with and without a magnetic field applied, as shown in Fig. 6.19 and Fig. 6.20. Across all measurements it was observed that an increased lattice temperature increased the resistivity measured. This is expected, but it was also found that different regimes had a different change in resistivity even at the same lattice temperatures. For the differential resistivity measurements with magnetic field prior to the Bloch-Grüneisen transition this makes sense, as by increasing the lattice temperature the starting point for the current sweep occurs closer to the Bloch-Grüneisen transition. By extrapolating the data it was found that the regime of reduced resistivity would disappear between 7.8 and 9.7 K, which matches well with the calculated Bloch-Grüneisen temperature of 9.12 K.

Chapter 7

Transmission Electron Microscopy study of AuNiGe-based ohmic contacts

7.1 Introduction

The advent of modern microscopy has allowed for the investigation of smaller and smaller systems. One of the big breakthroughs in microscopy has been the use of electron microscopy, first realised in 1928 [129], where the electron replaced the photon as the source of illumination, resulting in dramatically improved resolution due to the reduced de Broglie wavelength. State-of-the-art electron microscopes such as the Scanning Electron Microscope (SEM) and the Transmission Electron Microscope (TEM) combined with other modern microscopy techniques has allowed for the investigation of surfaces and crystalline structures at resolutions down to the atomic level [130]. As a result it has enabled the investigation of the microscopic ohmic contacts found on GaAs/AlGaAs two-dimensional electron gases (2DEGs), which were previously found to be superconducting around 1 K [66] shown in Fig. 7.1, which has a significant impact on their ability to cool due to Andreev reflection [1]. The study performed on these contacts looked at two different samples where the 2DEG is formed 90 nm below the surface, W476 and V834, which used two different types of AuNiGe-based ohmic recipes, eutectic slug and layered eutectic respectively. For W476, with a eutectic slug recipe, meaning that the elements are mixed prior to being deposited, the weight distribution was 83:12:5 for Au:Ge:Ni respectively. For V834, with a layered eutectic recipe meaning that the individual layers were deposited, the amounts were a 130 nm AuGe layer, a 50 nm Ni layer, and a 164 nm Au layer. Both sets of ohmic contacts were then annealed in forming gas at 430°C in a rapid thermal annealer for 80 seconds. The exact temperature and time might vary a small amount, but this annealing process is somewhat standard for making AlGaAs ohmic contacts [62]. There are two main findings of this chapter. The first is that a significant amount of the 2DEG below the bulk of the ohmic contact appears to have been eroded by the annealing process and the second is a further narrowing down of the potential compound(s) that could be responsible for the superconductivity.

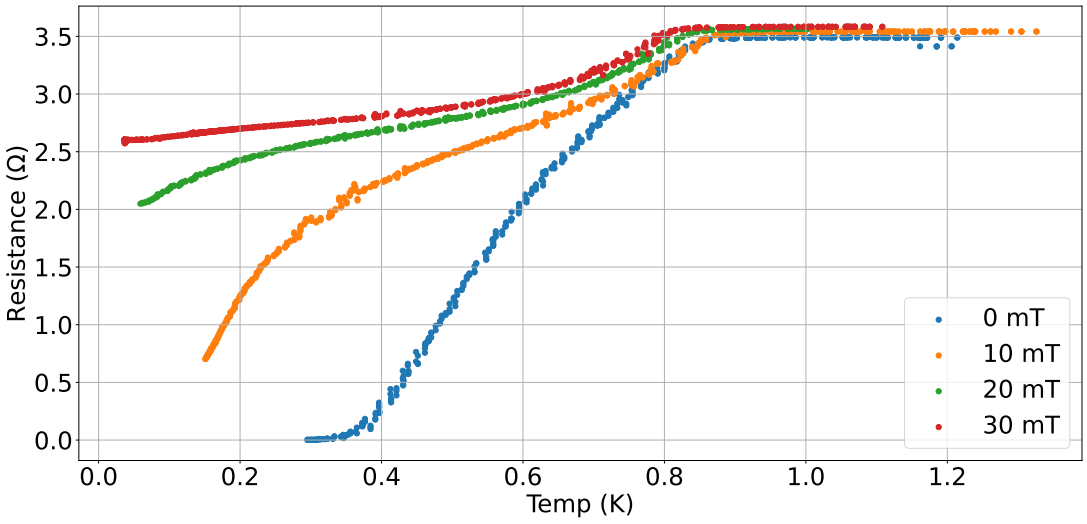

Figure 7.1: Superconducting transition of W476 sample with a eutectic slug recipe for various perpendicular magnetic fields. The transition begins at 0.8 K and the contact has gone fully superconducting by 0.3 K at no applied field. The superconducting transition is quickly destroyed upon the application of a magnetic field, as can be seen by the 10 and 20 mT curves.

7.2 Elemental Composition

In order to assess the cause of the superconductivity, it is necessary to quantify the elemental composition of the ohmic contact since the quantity of an element present will determine what crystalline structures are possible in the system. To quantify the elements energy-dispersive X-ray spectroscopy (EDS) was used with a focus on the elements seen in Table 7.1. Note that while the ohmic recipe and quantity of elements differed between W476 and V834 the elements used were the same.

Element	Source	Amount	EDS peak(s) (keV)[76]
Ga	wafer	Main wafer constituent	9.25, 1.1
As	wafer	Main wafer constituent	10.54, 1.28
Al	wafer	Only in 80 nm of $Al_{0.33}Ga_{0.66}As$	1.49
Si	wafer	Only in 40 nm of AlGaAs (negligible)	1.74
Au	ohmic	Main element in ohmic recipe	9.71, 2.12
Ge	ohmic	Secondary element in ohmic recipe	9.88, 1.19
Ni	ohmic	Small amount in ohmic recipe	7.48, 0.85

Table 7.1: Table of the elements present in the system, their origin, a rough idea of the amount present, and their EDS peak(s). The key takeaway is that there are many different elements present in significant enough amounts to form compounds, but the three main elements are Gallium, Arsenic, and Gold. Some combination of these would be expected to make up the bulk of the ohmic contact. Some elements such as Al, Ni and Ge are present as well, but a lot less, so if they were to be a part of the bulk contact, then it would be in very low concentrations. The significance of this is that when there is very little of an element present in the bulk of a system then it will usually not alter the crystalline structure. One example of this is Au and Al, where an Al content of less than 10% means Al is just absorbed into the Au structure without changing it [131].

7.2.1 W476

For the W476 eutectic slug sample two different regions were investigated. One at the centre of the ohmic contact, referred to as the bulk, and one over the crenellations which run along the edge of the ohmic contact, shown in Fig. 7.2. The region covered by the horizontal bar is what will be extracted for TEM analysis after being extracted and thinned used a Focused Ion Beam (FIB).

(a)

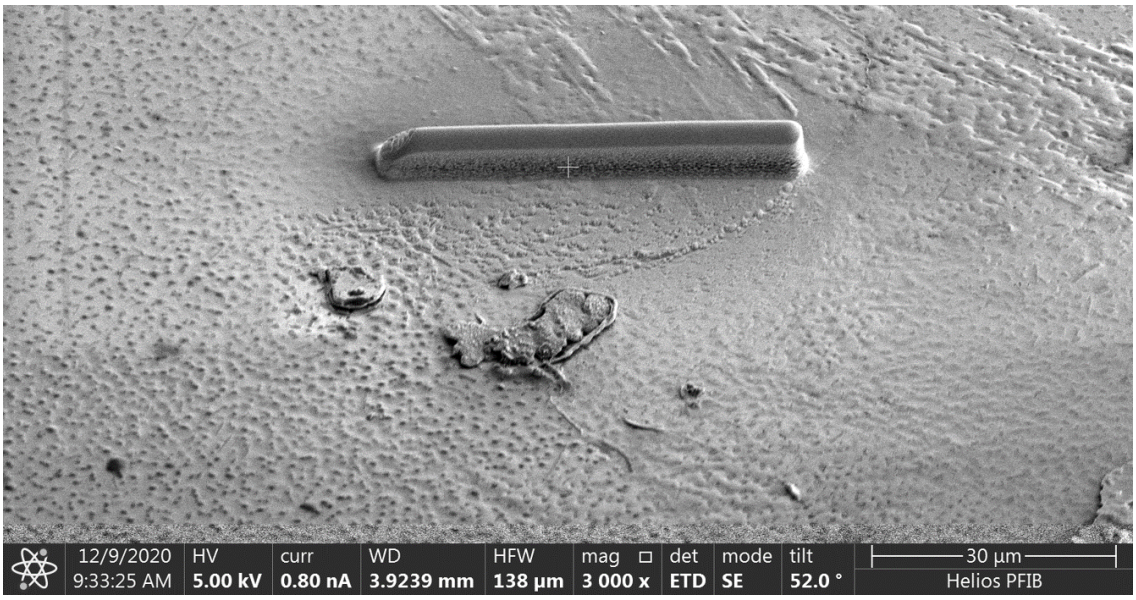

(b)

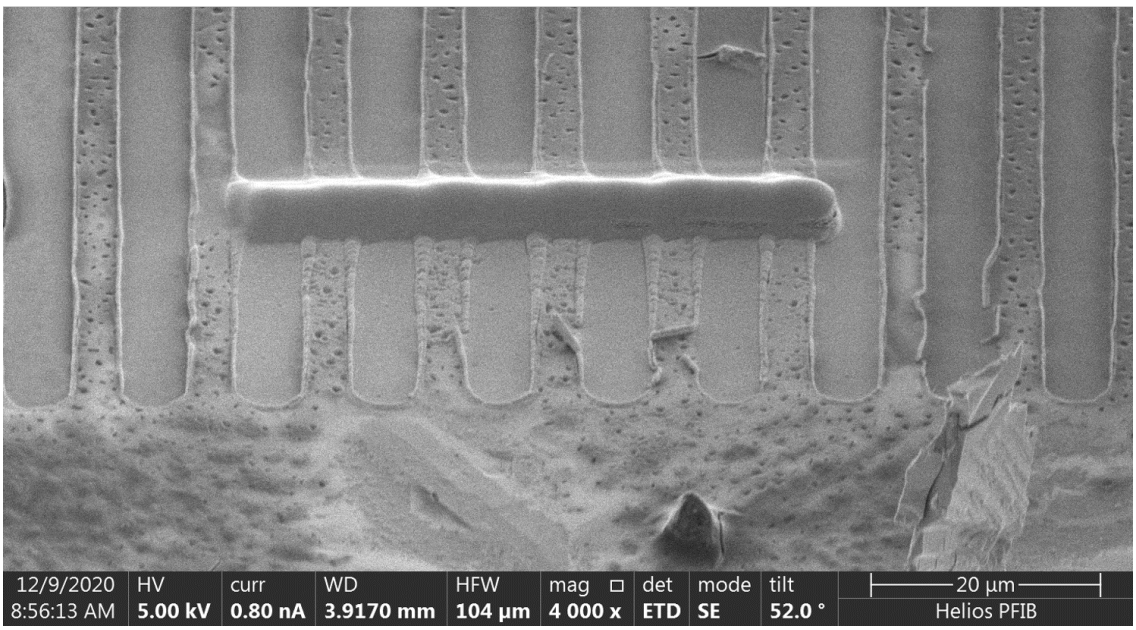

Figure 7.2: W476 FIB overview of the bulk (a) and the crenellations (b) near the edge of the ohmic contact. Both of these regions are littered with dark spot, which earlier SEM works [66] indicate is some type of Ni inclusion. The region covered by the horizontal bar is what will be extracted for TEM analysis. Note that these crenellations are typically included to improve the conduction to the 2DEG below, so it will be interesting to see if they have a different structure to the bulk of the contact. Credit for the images goes to Dr Gareth Hughes.

The cross-section of the W476 eutectic slug ohmic recipe is shown in Fig. 7.3. The width of this image is 4 μm. The ohmic contact is the central bar running down from left to right across the image and the TEM data has been taken in the region labelled 'Map data 2'. Since the 2DEG is only 90 nm deep then this means the data near the bottom of the region with TEM data is known GaAs, which is a useful reference. Next is the elemental analysis of this region, shown in Fig. 7.4, which shows As, Ga, Ni, Au, C, Ge, Al, and O. The bottom of the mapped region is confirmed to be GaAs as nothing else is present in a significant amount. Besides this the ohmic contact itself appears to be divided into two main regions. The first is a Ni and As region with a little bit of Ge which is seen towards the right of the figure. The second region is a Au/Ga/Al region which is near the left of the image. A smaller third region also appears between these two regions near the bottom of the ohmic contact, which is almost exclusively Ge.

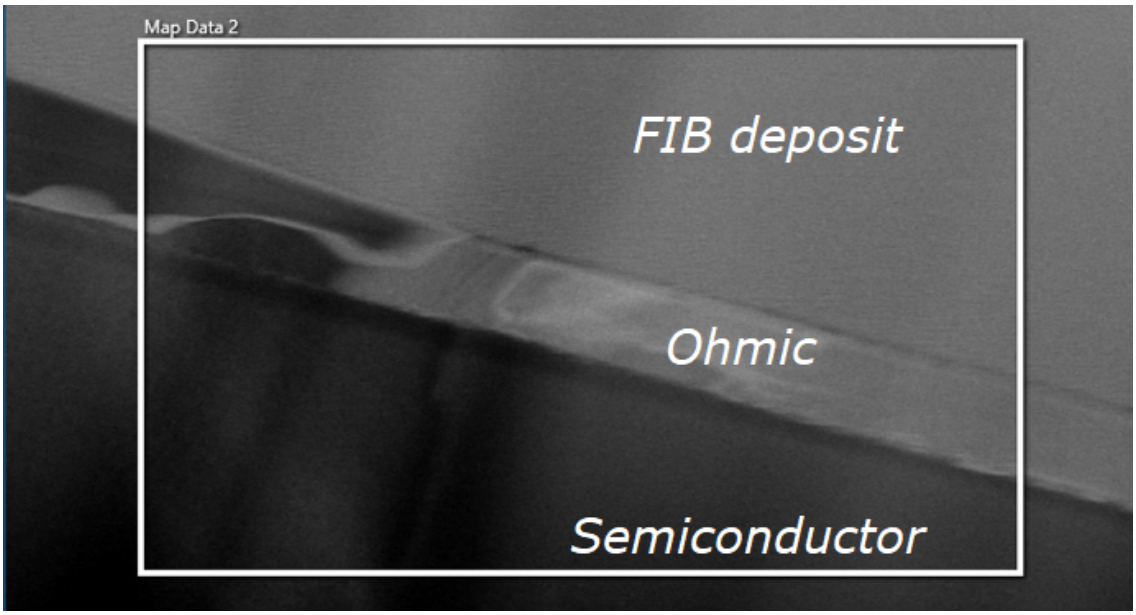

Figure 7.3: W476 bulk overview. The ohmic contact is the central bar running downwards from left to right across the image and the total width of the image is 4 μm. The TEM data has been taken in the rectangle labelled 'Map Data 2'. The region above is the adhesive metal used to extract the sample and the layer below is the semiconductor. Note that the 2DEG is only 90 nm below the surface so the composition near the bottom of the labelled region is known to be GaAs. Credit for the images goes to Dr Ian Griffiths.

(a)

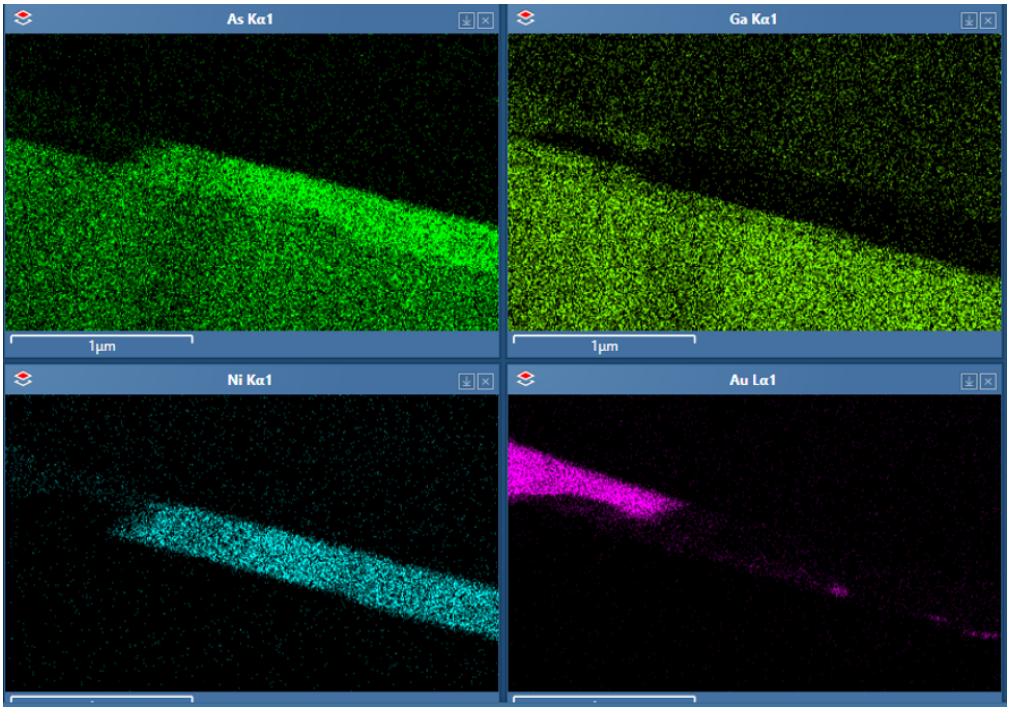

(b)

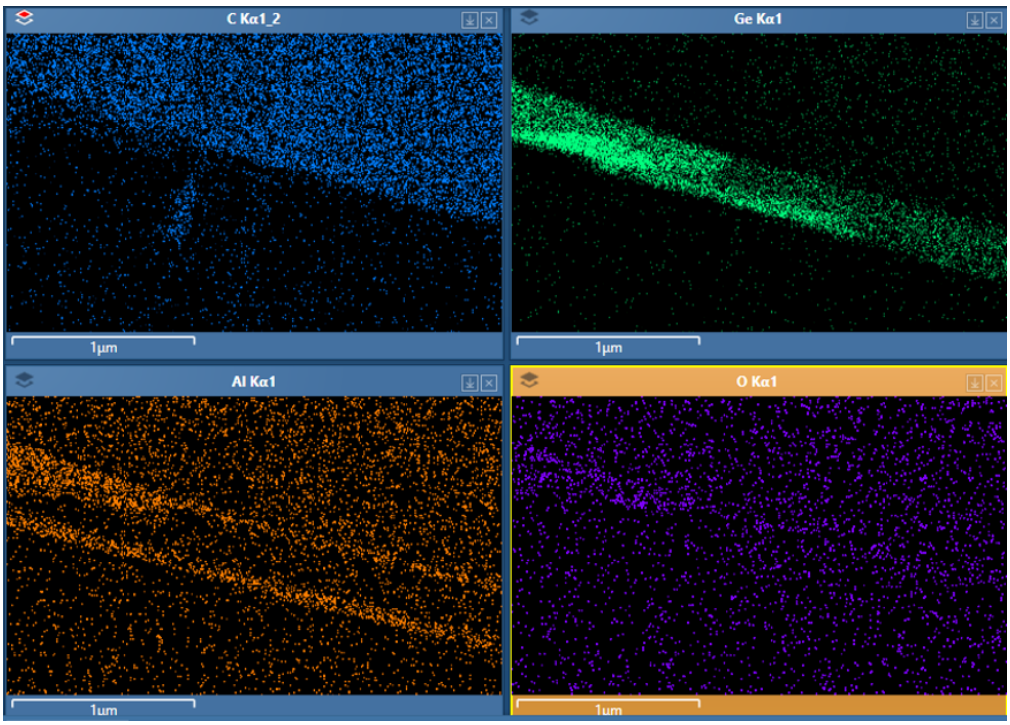

Figure 7.4: W476 bulk elemental overview for As, Ga, Ni, and Au in (a) and C, Ge, Al, and O in (b). Note that C and O are very common contaminants. Two main phases are observed, a AuGaAl phase toward the left of the ohmic, and a NiAsGe on the right of the ohmic. Note that there is a significant overlap in the energy spectrum of Au and Ge, meaning that any area which shows a large amount of Au and a little amount of Ge is unlikely to actually contain any significant amount of Ge. Credit for the images goes to Dr Ian Griffiths.

The images taken of the cross-section of the W476 crenellations, shown in Fig. 7.5, 7.6 and 7.7, shows a similar elemental composition and regions to the W476 bulk. There is a clear NiAsGe region and a AuGaAl region throughout the ohmic contact. In addition, there appears to a Ge-rich region exclusively near the bottom of the ohmic contact where it interfaces with the semiconductor.

The images taken at the crenellations also allow for the study of the effect of the ohmic contact on the semiconductor below. As previously seen As, Ga, and Al are being absorbed into the ohmic contact, meaning that the semiconductor below the contact is changing. Images taken near the edge of a crenellation, see Fig. 7.8, show that the ohmic contact is digging into the semiconductor below, as there is a clear step observed in the Ga of 70 nm. In addition significantly less Al is found right below the ohmic contact, raising doubts about the condition of the 2DEG.

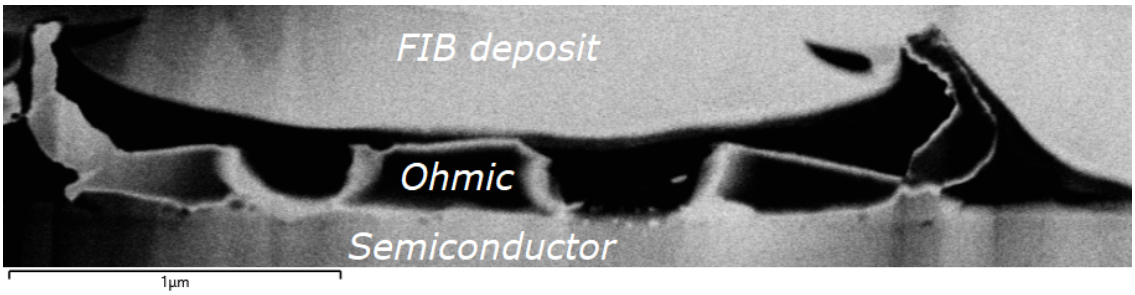

FA

Figure 7.5: W476 crenellations overview. Side view of a single crenellation. The ohmic contact itself is about 3 μm wide and has an apparent U shape. Three layers are present in this figure. The FIB deposit on top, the ohmic contact in the middle and the semiconductor below. The ohmic crenellation appears to be inhomogeneous with clear borders observed throughout. Credit for the images goes to Dr Ian Griffiths.

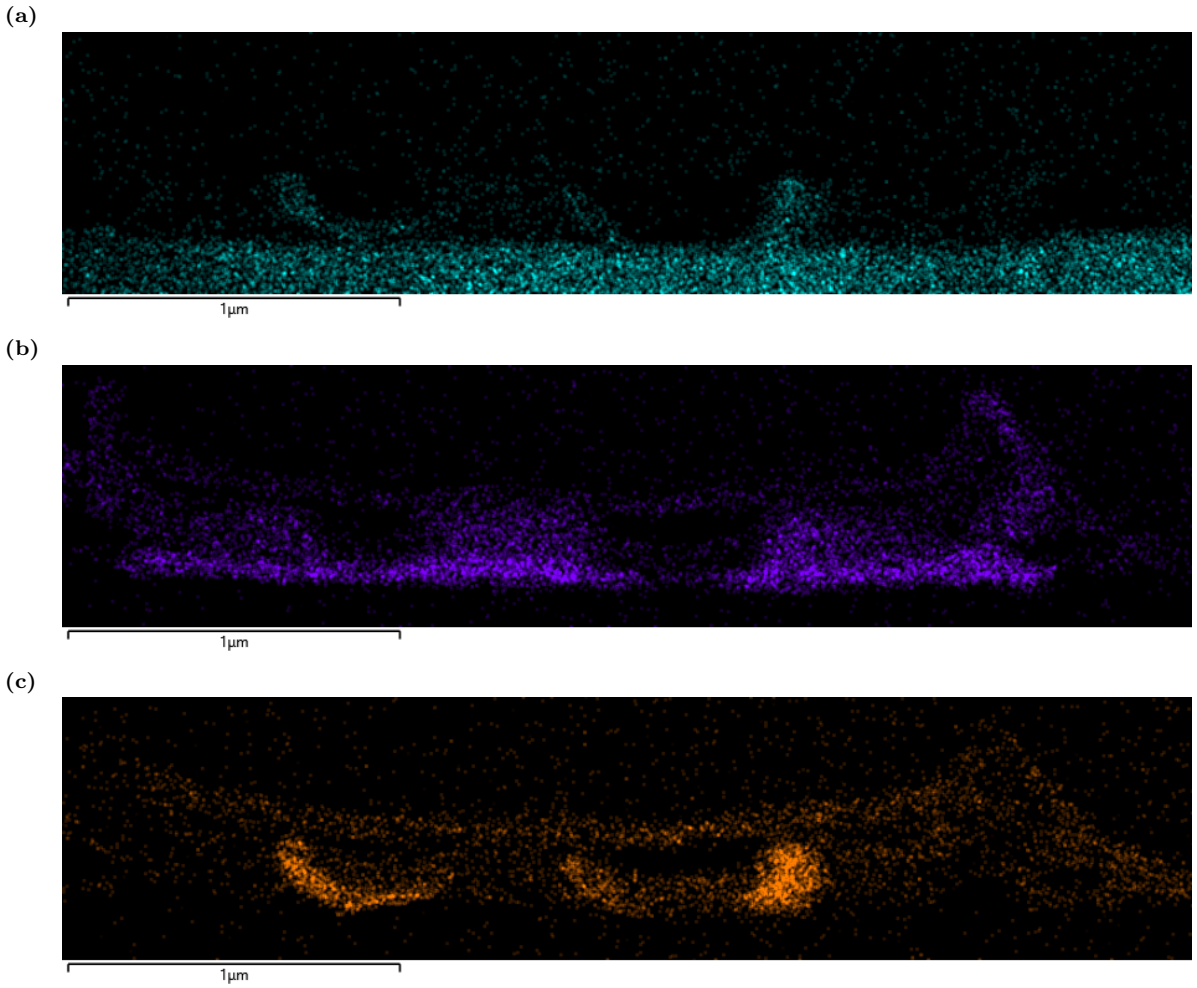

Figure 7.6: W476 crenellations elemental overview for (a) As, (b) Ge, and (c) Ni. Some As has moved into the ohmic contact and appears together with Ge and Ni. A significant amount of Ge is also found near the bottom of the ohmic contact close to the 2DEG. Some Ni appears throughout the crenellation, but the most concentrated regions are found where there is As and Ge. Since the Ni started off as a uniform layer, it appears that the annealing process is bunching it up together with As and Ge in order to form a stable phase. Credit for the images goes to Dr Ian Griffiths.

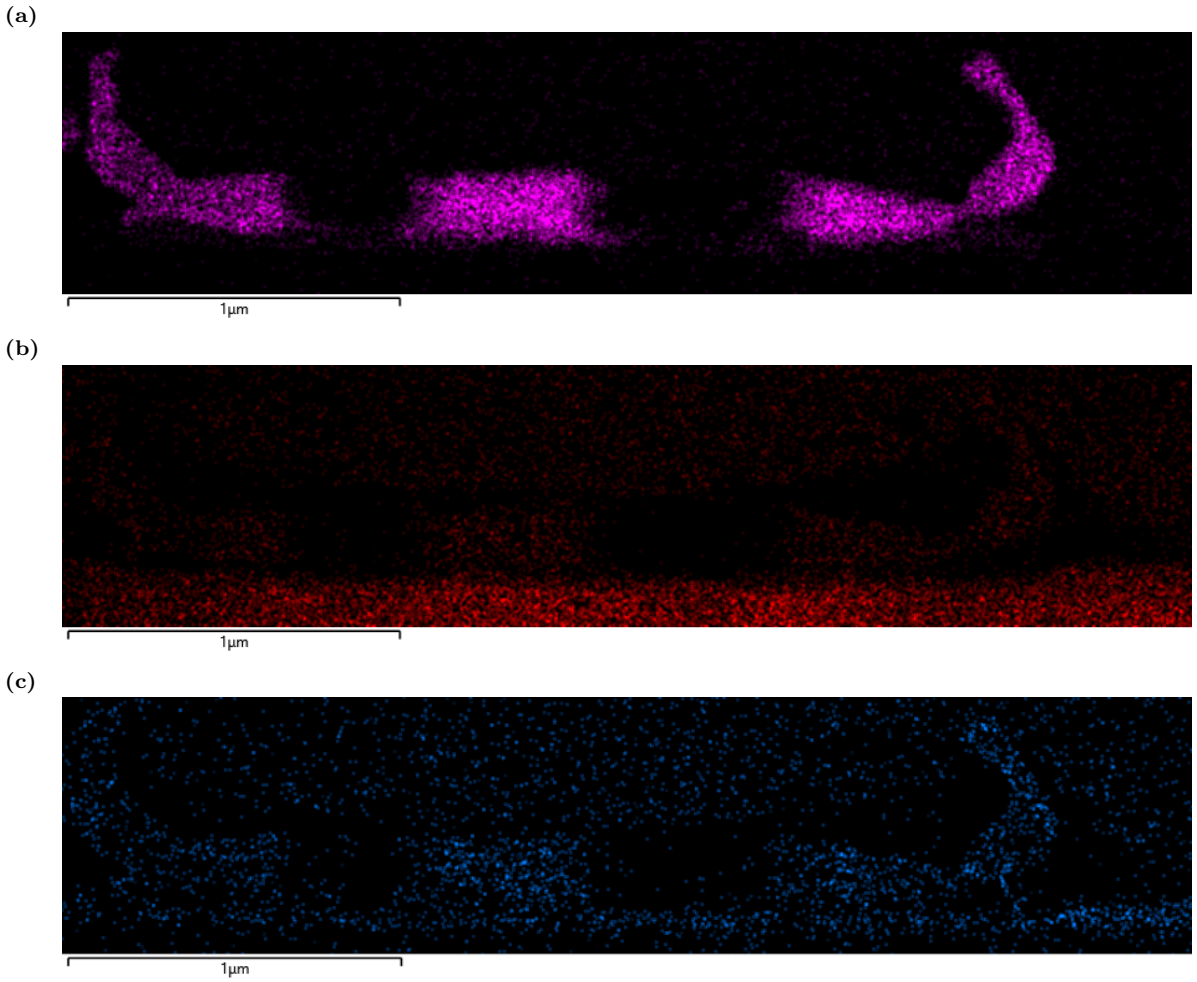

Figure 7.7: W476 crenellations elemental overview for (a) Au, (b) Ga, and (c) Al. Au is not uniformly found in the ohmic contact, but is instead found in concentrated regions where there is little to no Ni/As/Ge. Most of the Ga is found in the GaAs substrate, but some has made its way into the ohmic contact and is concentrated in the region with Au. Some Al has also found its way into the ohmic contact and is mostly found in the region with Ga and Au. It also appears that there is Al in the FIB deposit. This is not the case and could be the results of overlapping energy peaks or some Al in the system causing background noise. Credit for the images goes to Dr Ian Griffiths.

(a)

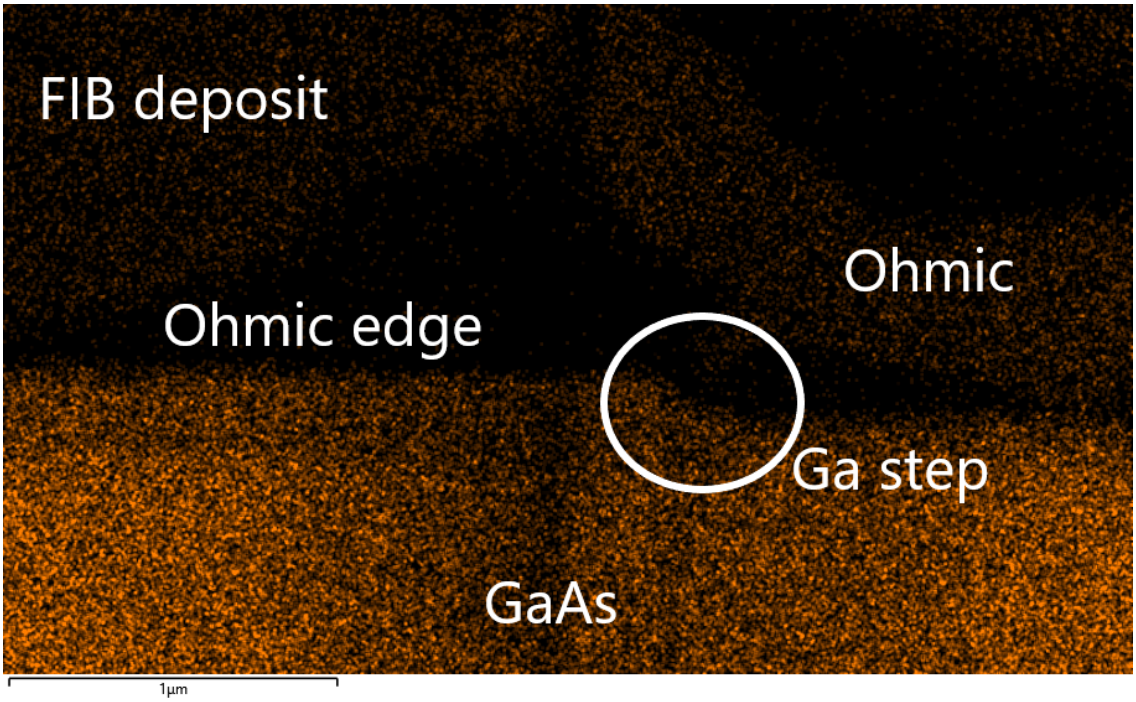

(b)

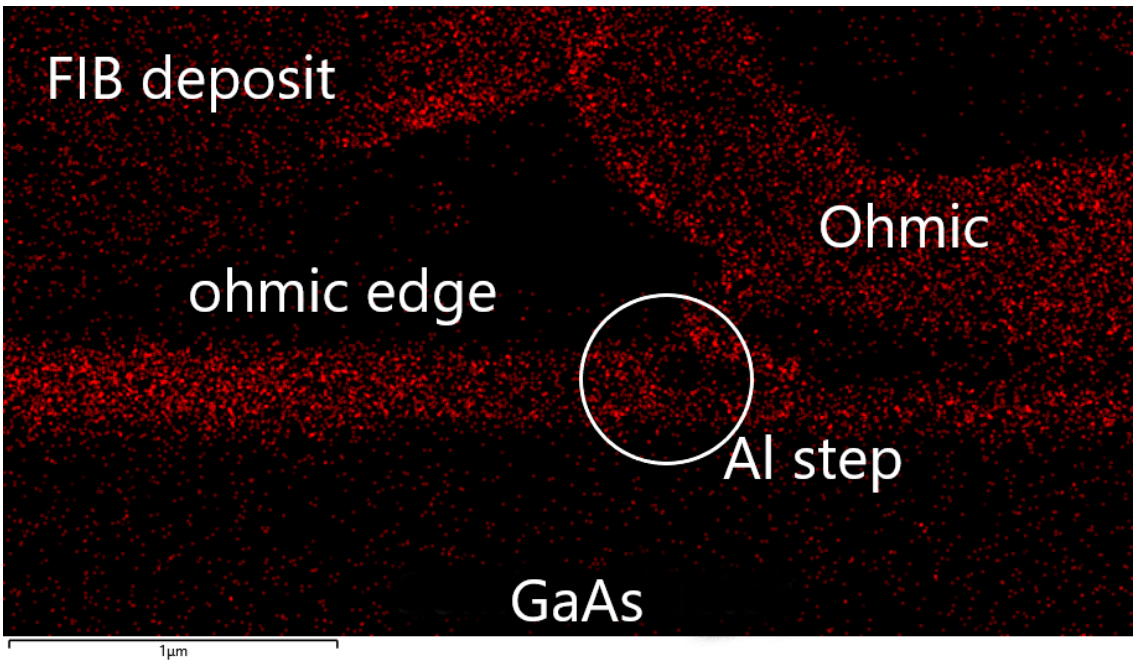

Figure 7.8: W476 crenellations edge image of (a) Ga and (b) Al. This data was taken on the far left of the same crenellations that have been shown previously. The Ga shows a clear step of approximately 70 nm as the semiconductor transitions from being directly below an ohmic contact to a region where it is not. The thickness of the Al seen in the semiconductor decreases as well. Credit for the images goes to Dr Ian Griffiths.

In summary, the images taken of the W476 bulk and crenellations show that the ohmic contact does not appear to be made up of a uniform region but rather a AuGaAl region, a NiAsGe region and an exclusive Ge region near the bottom of the ohmic contact. In addition, a clear step is observed in the semiconductor below the ohmic contact, which appears to be approximately 70 nm high. This is significant as originally the 2DEG was only 90 nm below the surface.

7.2.2 V834

The initial work carried out on the layered eutectic V834 sample was identical to that of the W476 eutectic slug sample. Two regions, one in the bulk of the ohmic contact and the other on the crenellations, were investigated.

The region of the bulk V834 sample investigated is shown in Fig. 7.9, which contains the interface between the ohmic contact and the semiconductor below. It can be seen that this interface contains deep grooves of depths greater than 100 nm on the far right and left of the image. The elemental composition can be seen in Fig. 7.10 and 7.11. The elemental composition can divided into three separate regions, just like the results for W476. One region for AuGaAl, one for NiAsGe, and an exclusive Ge region near the bottom of the ohmic contact. However there are some additional observations compared to the W476 results. Firstly, one of the inclusions seen in Fig. 7.10 appears to be attached to the semiconductor below. This same inclusion appears to not contain any As, whereas all other inclusions seen in the figure do. The second new observation, seen in Fig. 7.11, is that there appears to be almost no Al at all below the bulk of the ohmic contact. Only a small region appears towards the left in the figure of the semiconductor itself. The absence of Al raises some significant questions with respect to the existence of the 2DEG below the ohmic contact. In the W476 bulk sample there was a reduced amount of Al, but a continuous line was still observed.

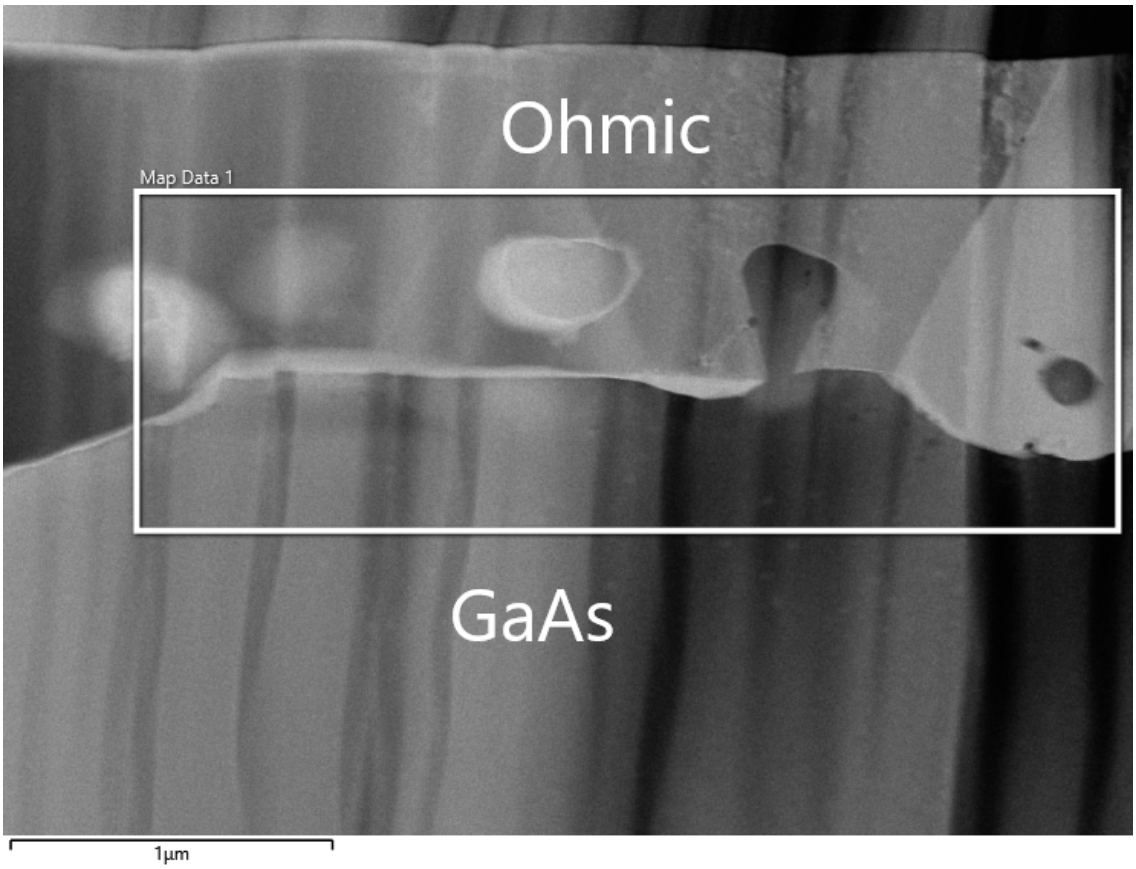

Figure 7.9: V834 bulk overview. The region for which there is elemental data is labelled as 'Map Data 1', which contains the bottom half of the ohmic contact as well as the top 300 nm of the semiconductor. One of the features that immediately stand out is how uneven the bottom of the ohmic contact is. At the far left and far right of the image deep grooves of depths greater than 100 nm are observed. Credit for the images goes to Dr Ian Griffiths.

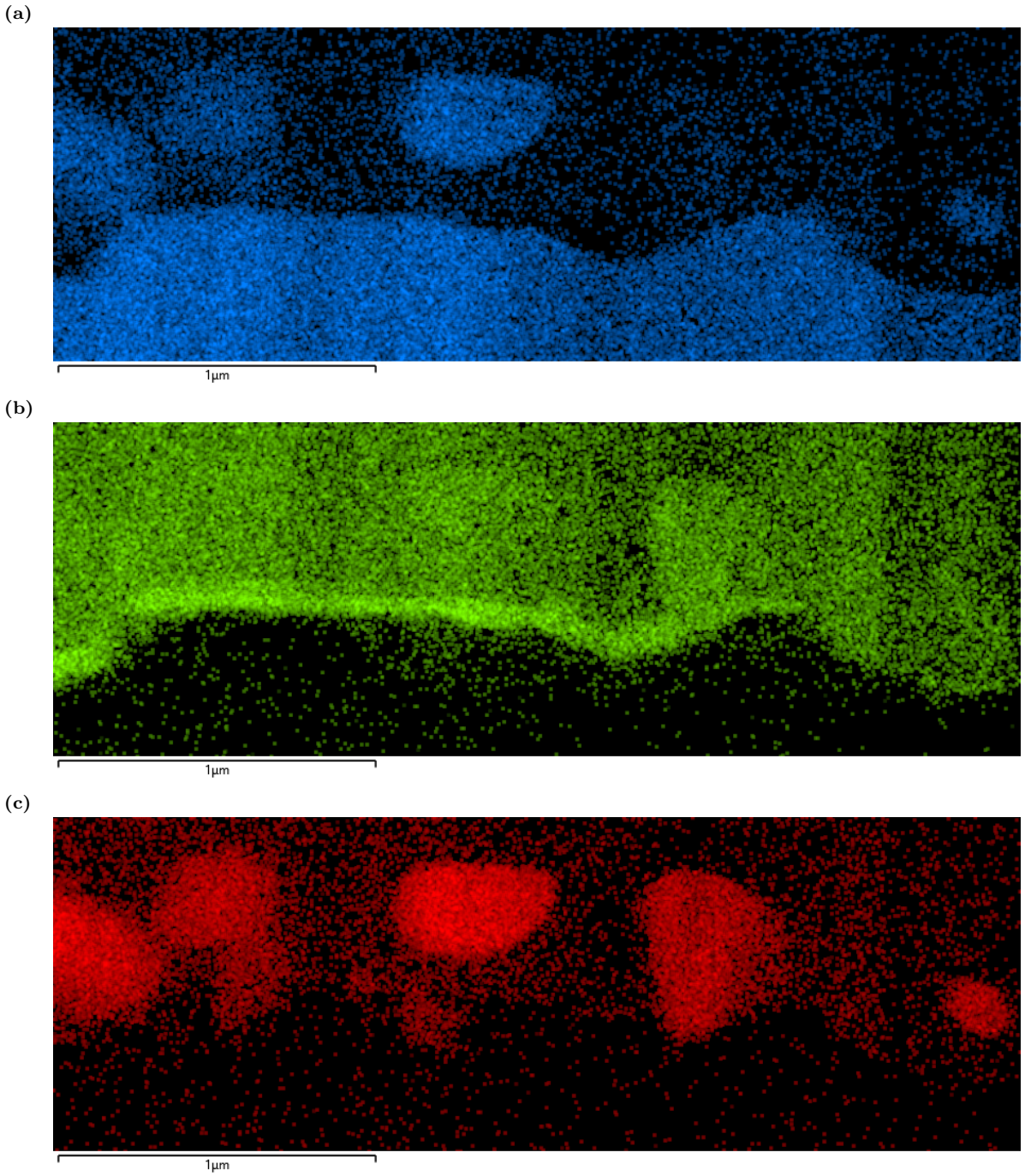

Figure 7.10: V834 bulk elemental overview for (a) As, (b) Ge, and (c) Ni. The interface between the semiconductor and the ohmic contact can be seen in the As-rich region running at the bottom of (a). A Ge-rich region is also seen at this interface. All the inclusions contain NiAsGe, except for one on the centre right which does not appear to contain any As, despite it being in contact with the As-rich semiconductor below. Credit for the images goes to Dr Ian Griffiths.

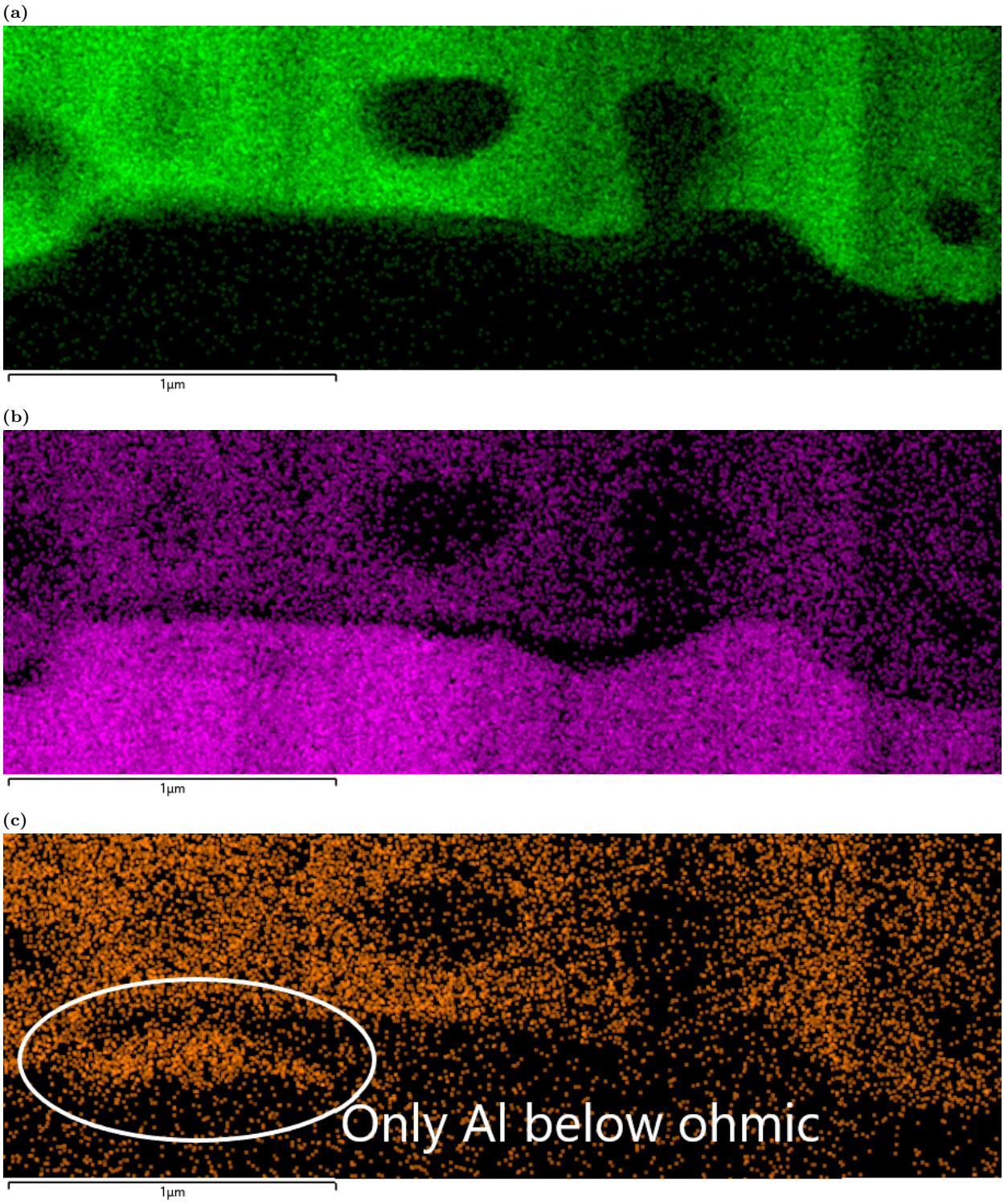

Figure 7.11: V834 bulk elemental overview for (a) Au, (b) Ga, and (c) Al. The interface between the ohmic contact and the semiconductor can be seen in (a) as there is no Au in the semiconductor. Throughout the ohmic contact there appears to be a very common AuGaAl phase. However, only a small amount of Al is observed in the semiconductor below the ohmic. This raises doubts about the existence of the 2DEG below the ohmic contact. Credit for the images goes to Dr Ian Griffiths.

Looking at the images of the V834 crenellations tells a similar story to W476. Figure 7.12 shows the overview image taken of one of the crenellations. The TEM data has been taken in the region labelled 'Map Data 3', which includes the ohmic contact on the left, a region without an ohmic contact on the top right, and the semiconductor below. The TEM data for Al and Ga can be seen in Fig. 7.13. As seen previously in the data for Ga there appears to be a 120 nm deep trench into the semiconductor where there is an ohmic contact annealed on top. These observations are even clearer when looking at the Al data as well where there is a distinct lack of concentrated Al below the ohmic contact, reinforcing the findings of the W476 crenellation data and the V834 bulk data.

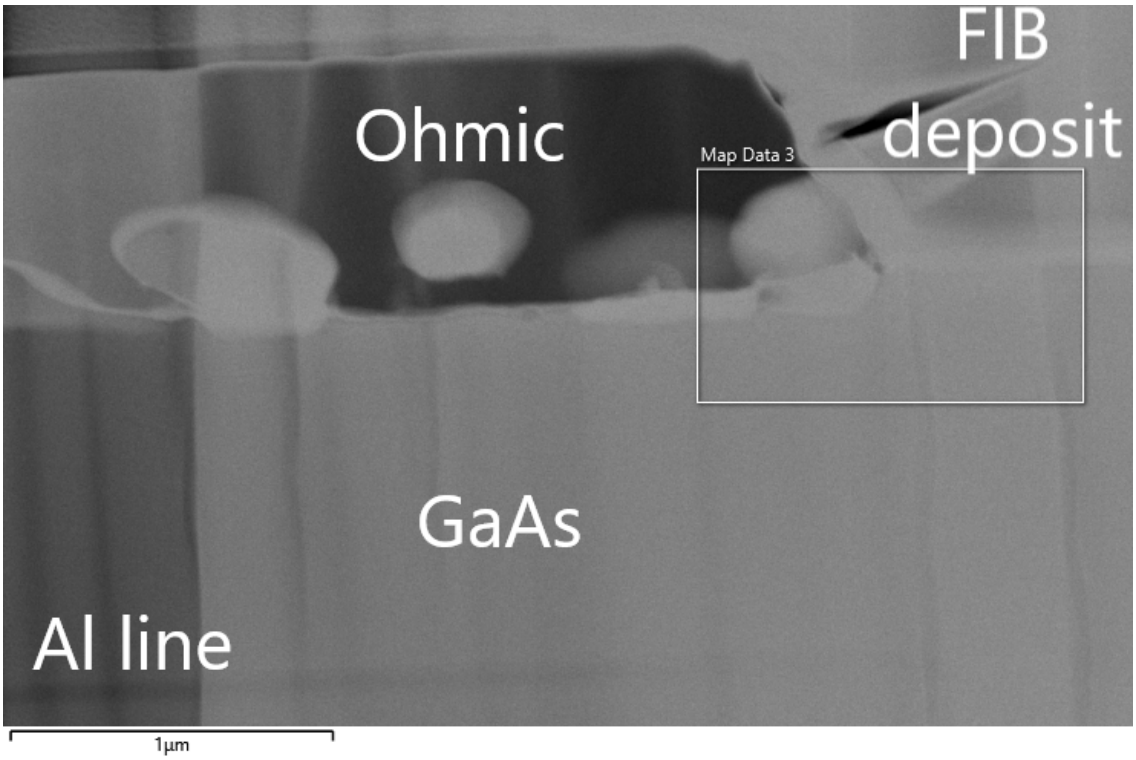

Figure 7.12: V834 crenellations overview. The TEM data was taken in the region labelled as 'Map Data 3', which covers a region of the semiconductor interface that has an ohmic contact on top (left) and not (right). Near the bottom of the picture there is a slightly darker horizontal line. This is the 50 nm AlAs line which is grown below the 1 μm GaAs layer. From left to right in the figure this line disappears. This is due to the sample getting thicker. Credit for the images goes to Dr Ian Griffiths.

(a)

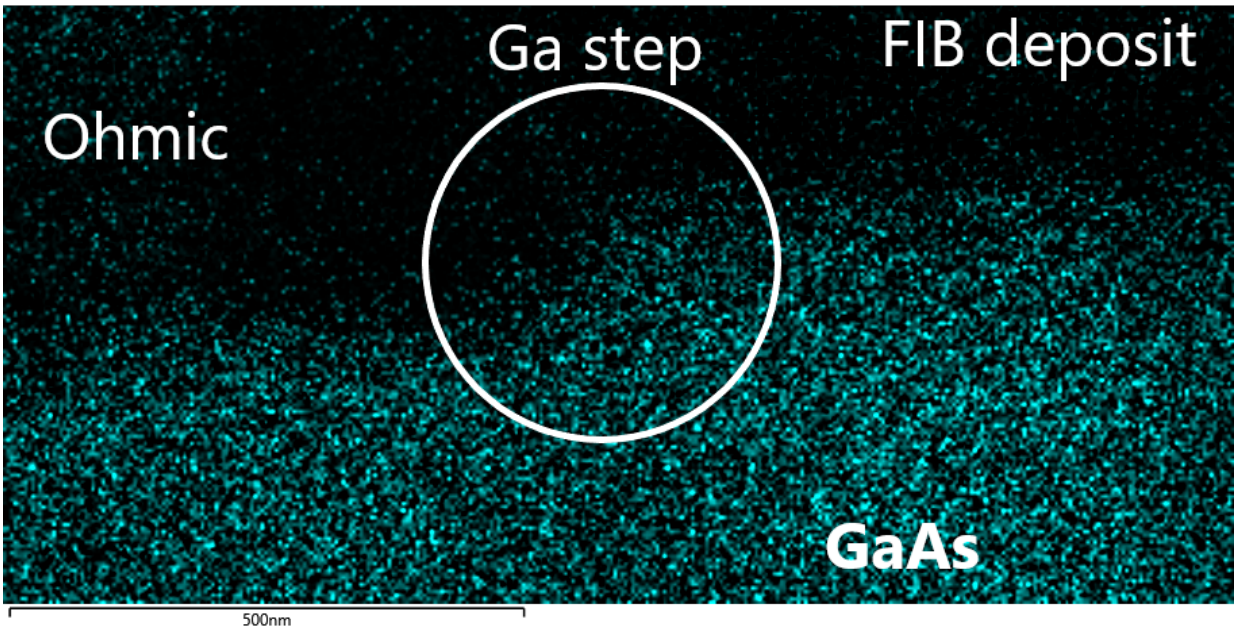

(b)

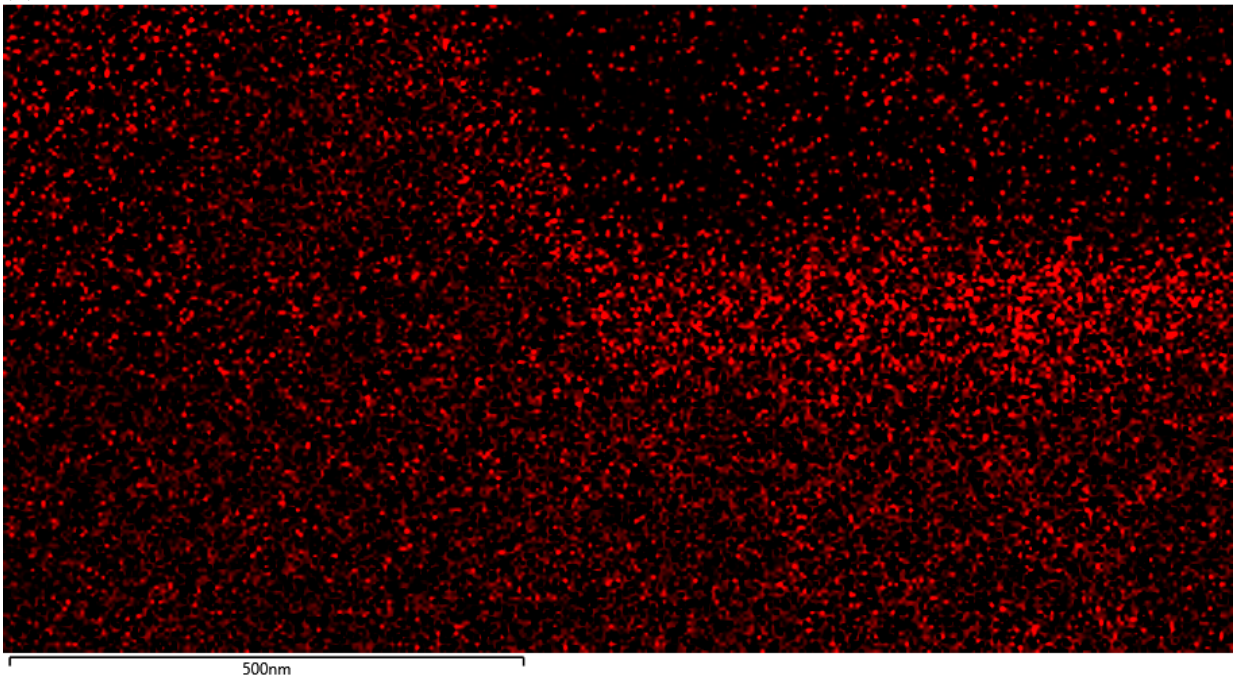

Figure 7.13: V834 crenellation elemental overview of Ga (a) and Al (b) of the same region outlined in the previous figure. The Ga view shows a clear step of about 120 nm from left to right where the left-hand side is below an ohmic contact and the right-hand side is not. The elemental overview for Al is similar, showing an increased concentration on the right-hand side as expected from the 80 nm layer, but not on the left-hand side. Credit for the images goes to Dr Ian Griffiths.

There are two main findings of these results. Firstly, after the annealing process, there appear to be 3 major groupings of elements in the ohmic contact itself. The first is a combination of NiAsGe, the second is a combination of AuGaAl, and the third is just Ge. The next step is to perform a structural analysis of these regions in order to find out which compounds these regions contain. The second finding of this section is the question of the existence of 2DEG below the ohmic contact. The data for W476 found some Al below the ohmic contact, but all the data for V834 indicates that the ohmic contact has eaten into the semiconductor by as much as 120 nm. This is problematic, as in both of these samples the 2DEG is only 90 nm deep.

7.3 Structural Analysis of V834

With the elemental composition of the samples it is now possible to perform a structural analysis of V834. The structural data was only taken for V834 for several reasons, these being that the sample was thinner and therefore more suitable for the equipment, and limited access to the required equipment. In order to carry out the structural analysis the program CrysTBox was used in conjunction with the TEM data, which includes estimated percentages of the included elements and crystallographic data. Note that the equipment used had not recently been calibrated and for the semiconductor GaAs region, which is known to be an even split between Ga and As, the TEM data found a 45/55 split between Ga and As. As a result, any estimation of the included elements have at least a 5% uncertainty.

To begin with, an analysis of the known GaAs structure was carried out in order to test the data as well as CrysTBox, as shown in Fig. 7.14. The CrysTBox program finds the zone axis, the miller indices for all the points and finds the data to be in good agreement with the expected results of a GaAs Zinc Blende structure.

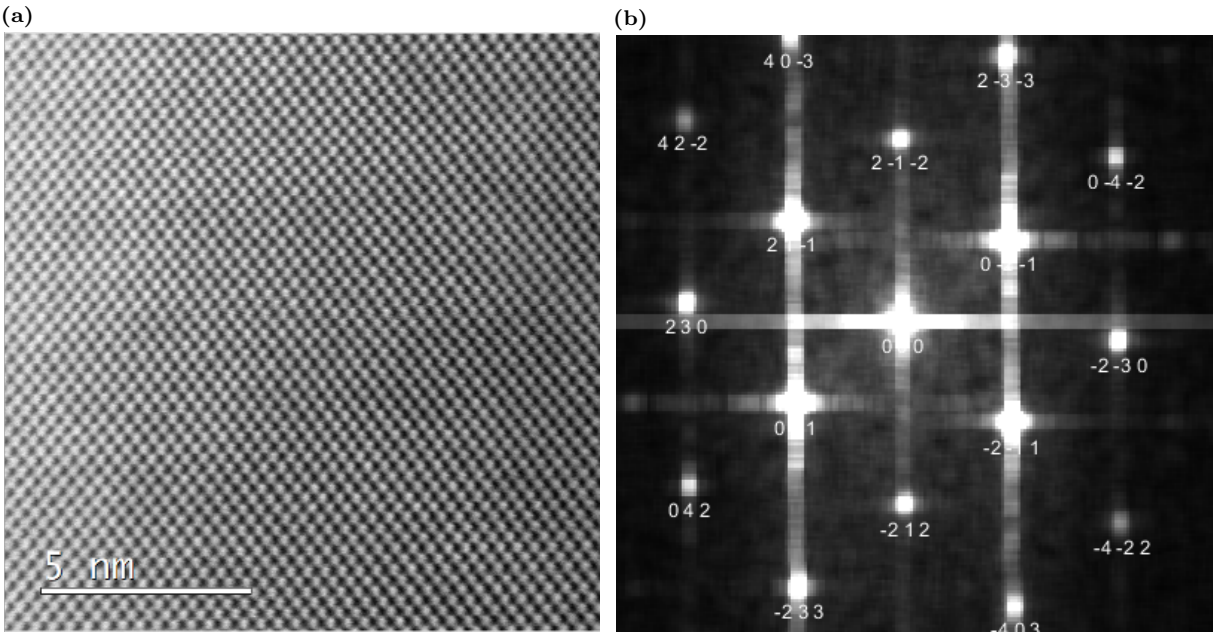

Figure 7.14: V834 GaAs layer with a 15 million x magnification in (a) and an FFT in (b). The CrysTBox program was able to find the zone axis of 3 -2 4, the miller indices of all the points, and finds the provided image to be in very good agreement with what is expected from a GaAs zinc blende structure.

The first region of interest is the AuGaAl region, which was found to be the dominant region throughout the ohmic contact. The following data is of the V834 bulk region, which

is shown in Fig. 7.15. The exact content of Au/Ga/Al varied throughout the system, but generally speaking the Au content was at minimum 80 %, with the remaining being split between Al and Ga. Regions 2 and 5 were found to have a good match with Au_7Ga_2, as shown in Fig. 7.16. The elemental composition of 80% and 15% for Au and Ga respectively is not a perfect match for this phase, but given the uncertainty of the composition it is entirely possible. Within this AuGaAl region only the top of the ohmic contact was found to have a large amount of Al, at approximately 10%.

The second region of interest is the Ge rich region near the bottom of the ohmic contact, which was found to have crystalline structure, shown via Kikuchi lines. Due to its very high Ge content of 90+% it is likely that this region is crystalline Ge with a few contaminants.

The third region is the NiAsGe inclusions, which appear throughout the ohmic contact. When investigating these Kikuchi lines were found alongside an elemental composition of about 50% Ni, 25% As, and 25% Ge, suggesting that the phase is Ni_2AsGe.

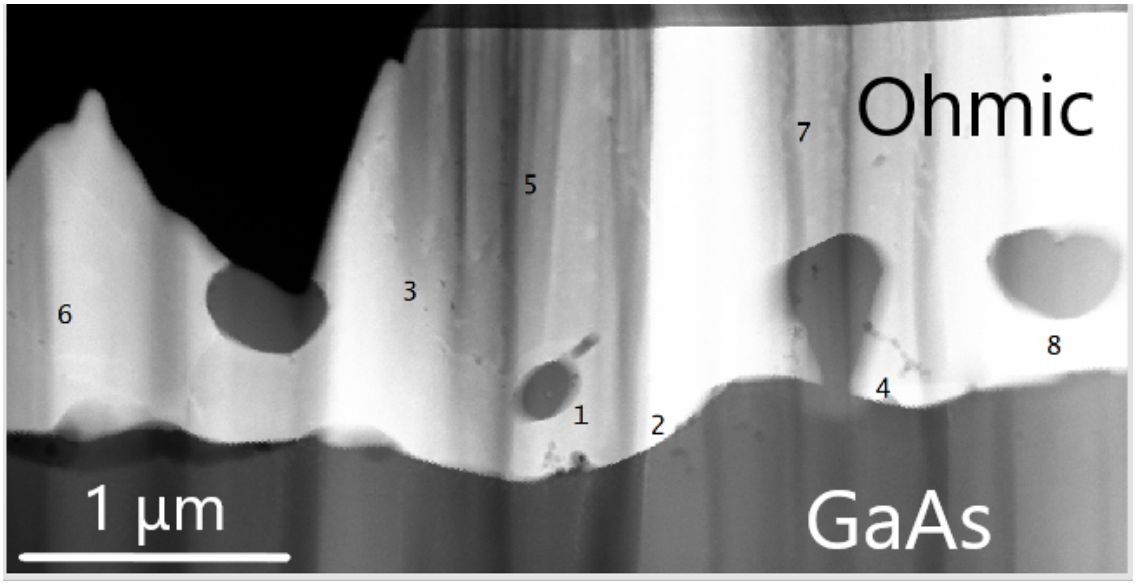

Figure 7.15: V834 crystalline structure AuGaAl overview. The labelled regions are different parts of the AuGaAl rich region of the ohmic contact that was investigated. All of these regions were found to have crystalline structure, but good data was only obtained for region 2 and 5. Region 2 and 5 were found to have a roughly 80/15/5 split of Au/Ga/Al. The region with the highest Al content was found right above the region labelled 7, where the split was 85/5/10 between Au/Ga/Al. All other labelled regions had values within ± 5% of region 2 and 5. Credit for the images goes to Dr Ian Griffiths.

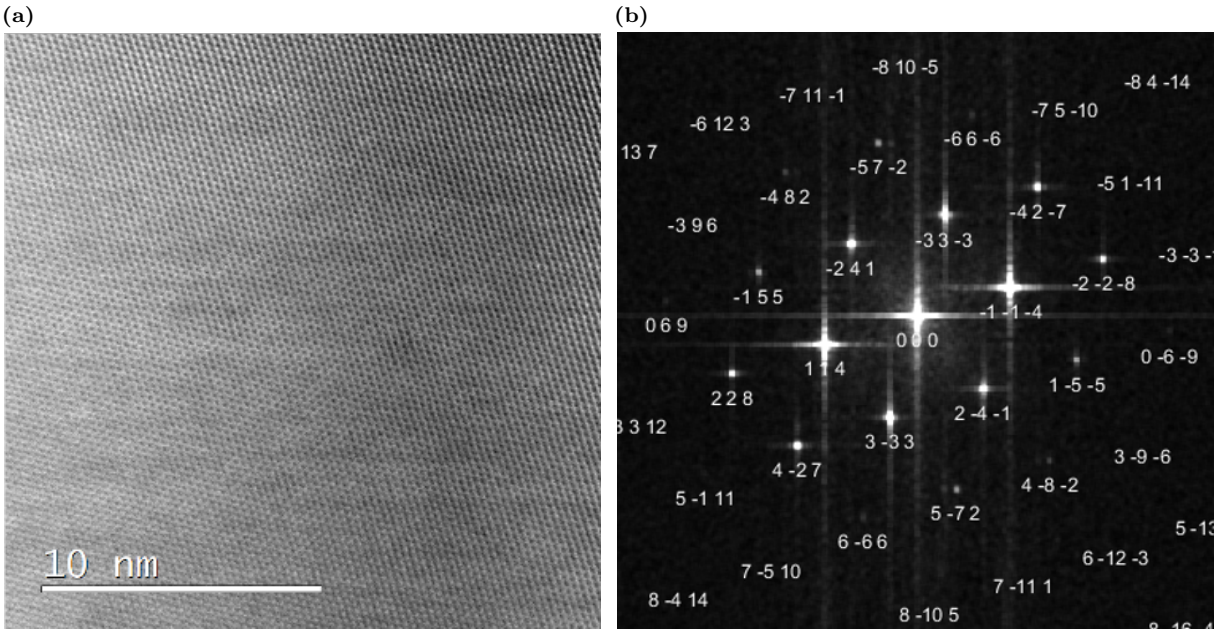

Figure 7.16: V834 Au_7Ga_2. (a) The crystal structure found in the ohmic contact of the layered eutectic V834 at a magnification of twelve million. A clear crystalline structure is shown allowing a FFT to be produced as seen in (b). This FFT is a great match for Au_7Ga_2, an observation which is further supported by elemental composition which was found to be 80% Au and 15% Ga given uncertainties of approximately 5 %. Credit for the images goes to Dr Ian Griffiths and CrysTBox.

7.4 Discussion

The aim of this chapter is to better understand the annealing process of Au/Ni/Ge-based ohmic contacts on AlGaAs 2DEGs and to uncover the phase(s) responsible for the superconductivity. From the TEM study done and the figures presented in this chapter it is shown that the ohmic contact at this stage develops into three separate regions. In addition, questions have been raised about the quality of the 2DEG beneath these ohmic contacts, giving credence to the idea that most of the conduction occurs near the edge of the contact. This section aims to further discuss what the superconductor could be and what the state of the 2DEG below the ohmic contact is.

7.4.1 Potential Superconductors

Three significant distinct regions were found in the ohmic contact. A Ge-rich region, a Au(Ga, Al)-rich region and a NiAsGe-rich region. A fourth region consisting of NiGe was also observed in the bulk V834 sample. All previous studies have found an Au-rich region with some amount of Ga and Al, but there is some disagreement on exactly what phase is observed, as is shown in Table 2.2. Similarly a NiAsGe region and a NiGe region have also been observed previously [63, 64, 61], however an exclusively Ge-rich region has not.

Finding the superconductor is further complicated by the possible existence of a percolating network. Reference [1] was still able to cool the electrons below 1 K, contributing to the ohmic contact being only partially superconducting. Because the main phase, Au_7Ga_2, found in the bulk of the ohmic contact is not supposed to be a superconductor, something else has to be, such as one of the other regions found or from a continuous interface between the regions found. A percolating network means that even a small region will at some point reach a critical fraction p_c where it is able to form a continuous phase throughout the structure without being the main phase [132, 133]. In this case it is uncertain whether the critical threshold is even required. A percolating network close to p_c could be sufficient as the resistance would be too low to measure.

Another complicating factor is the changes to superconductivity of a material depending on whether it exists in bulk, as a thin film, and what impurities are present. One example of this is Aluminium, where as a thin film or depending on the impurities present the T_c changes [134, 135]. The discussion here will mainly focus on the bulk properties of the various potential superconductors, but the presence of a thin film superconductor remains possible.

7.4.1.1 Ge related phases

The crystalline Ge phase appears to be one of the least likely candidates for the superconductivity in the ohmic contacts, due to it not forming a continuous phase throughout and because pure Ge is not typically a superconductor. However, Ge readily forms various superconductors together with other elements [136, 137]. There is also some literature [138] saying that Ge can under the right circumstances, with a small amount of Ga, which is present, form a superconductor with a critical temperature of around 1 K. The main Ge phase was not found to contain a significant amount of Ga, but the regions surrounding the Ge phase do. A critical temperature of around 1 K matches the observations made in Fig. 7.1, but the minimum annealing temperature used for this is about 700°C, which is significantly higher than what these ohmic contacts were exposed to. Another alternative for the superconductor is AuGe. Superconducting AuGe compounds exists, and have an appropriate critical temperature around 1 K [139], but this is contested [140]. There are also layered AuGe compounds [141], which could exist along the interface between the Au rich region and the Ge rich region. The main issue with AuGe however is that it is very difficult to quantify small amounts of Ge using TEM due to the set of elements present in the ohmic contact. The transmission energies of Ge are all weak and coincide with other much more abundant transmission energies. A paper by Wan et al. [142] did also observe superconductivity in their AlGaAs 2DEGs, but their ohmic contacts were made of AuGe and NbN instead of AuNiGe. Their superconductor had the same critical temperature as seen here, but a much higher critical field.

Ultimately the AuGe phase seems like a promising candidate for a superconductor, but its existence in the AuNiGe-based ohmic contact has not been proved and would be difficult to prove. In addition to the issue of being able to precisely measure the quantity present, there is also the issue of whether or not there is a sufficient amount of Ge present to form a continuous layer of AuGe throughout the ohmic contact. The initial layers of AuGe and Au were 130 and 164 nm respectively, resulting in a Au:Ge ratio that is at most 3:1, but is lowered further by the NiAsGe inclusions and the pure Ge phase.

7.4.1.2 NiAsGe related phases

Ni is essential in the formation of low-resistivity ohmic contacts [63]. The main Ni related phase found was Ni_2AsGe. However, the Ni_2AsGe phase is a poor candidate for superconductivity as it only exists as inclusions scattered throughout the ohmic contact and is not known to be a superconductor. There are related phases such as NiAs, NiAs(Ge), NiGe(As),

and NiGeAs, which other studies have found in ohmic contacts [143, 61, 144] and could potentially be present here, but none of these have been found to go superconducting.

7.4.1.3 AuGa related phases

The Au_7Ga_2 phase, also known as β-AuGa [145], was the only AuGa phase definitively found in the ohmic contacts studied. This phase has previously been found in AuNiGe-based ohmic contacts [64], but is not an established superconductor. There are however a myriad of different AuGa phases, which can be found in the literature [145, 146], but the main constraint for most of these is that the Au content is so high that the only other potential AuGa phase that could be present is α-AuGa, small amounts of Ga absorbed into Au, which has been found in AuNiGe-based ohmic contacts [62] and is a superconductor [147], but does not have the right critical temperature.

There are some other alternatives, but they remain speculative as they were not found in the ohmic contact. One possible candidate is α-Ga, which has been found in AuNiGe-based ohmic contacts [148], and has a close critical temperature, at 1.1 K, but a much lower critical field [149]. Some literature [150] also exists on the superconductivity of Ga in various confined geometries, but with too high a critical temperature to be a possible candidate.

7.4.1.4 AuAl related phases

As with AuGa related phases there are many different AuAl phases [151, 152], but the Al content found, even near the top of the ohmic contact, only got up to 10%. According to [131] Au can absorb up to 16% Al without altering its structure depending on the temperature. That being said, near the top of the ohmic contact there could locally be a higher Al content, sufficient to form an AuAl phase or potentially pure Al. Both of these are superconductors with critical temperatures of 0.3-0.7 K and 1.2 K for Au_4Al [153] and Al [154], respectively. However, the critical field of Al is about 10 mT which is too low for the observed superconductor.

It is possible to calculate a mean of the Au-to-Al ratio in the ohmic contact assuming that all of the Al below the contact is released. The original $Al_{0.33}Ga_{0.67}As$ layer in the semiconductor is 80 nm, whereas the Au consists of a 130 nm AuGe layer and a 164 nm layer of pure Au. Assuming the AuGe layer is exactly 50% Au then the real thickness of pure Au is functionally 229 nm. Similarly, 80 nm of $Al_{0.33}Ga_{0.67}A$ can be simplified to 26.7 nm of AlAs. Each unit cell of Au contains 1 Au atom and each unit cell of AlAs contains 4 Al atoms. Combining these numbers gives a mean ratio of a little over 2:1 for Au:Al. The high

ratio of Al:Au has two implications. Firstly there could still be significant amounts of Al left beneath the ohmic contact, and the sample investigated just happened to be in a region with little Al left. Secondly, there is theoretically enough Al to form the Au_4Al phase at the top of the ohmic contact, in fact, previous work claims to have found Au_2Al [155]. If the layer is thin enough then the calculated composition using the TEM could be thrown off due to an insufficient resolution. Ultimately, the Au_4Al phase remains a possible superconductor, but no direct evidence of it was found.

One issue with the measurement of Al in the ohmic contact is oxidation. Exposed Al in GaAs/AlGaAs will oxidise over time [156], meaning that any TEM samples exposed to oxygen may have an unreliable Al content that will vary depending on exposure time. For this thesis there were two separate TEM sessions of the same samples, which were separated by months. It was observed that the Al content dropped dramatically from the first round of TEM measurements to the second.

7.4.2 Existence of 2DEG below the ohmic contact

In both the W476 and the V834 samples there was a clear reduction of the Al in the semiconductor below the ohmic contact and the semiconductor in this area has a very inhomogeneous surface, as shown in Fig. 7.8, 7.11, and 7.13. This at the very least raises questions about the health of the 2DEG below the ohmic contact since Al is crucial with respect to creating the right energy-band conditions for a 2DEG as explained in Section 2.4. To add to this, the calculations in the previous section do suggest that not all the Al has left the superconductor and it could potentially be specific to the sample studied. Originally, crenellations were added to the edge of ohmic contacts because it was thought that the perimeter of the contact determined the contact resistance and not the area. This reinforces the idea that the 2DEG below the bulk of the ohmic is damaged and is therefore a poor conductor. A higher concentration of Ge was found near the edge of the crenellations as well, which is further evidence of this as Ge acts as a dopant that reduces the Schottky barrier [157].

7.5 Summary

The aim of the TEM study was to further narrow down the potential candidates for the superconductor in the ohmic contacts annealed with different recipes. In this context, the superconductivity is not desirable, as it reduces the ability of ohmic contacts to cool at lower temperatures.

The results have been unable to definitively narrow down the candidates, but there are still several promising ones. These are Au_4Al, α-Ga, and AuGe which all roughly have the right superconducting temperatures. Another alternative is that the superconductivity is caused by a combination of several different phases. Ultimately, in order to narrow down the alternatives further, a much more granular TEM study is required. This becomes even more important when considering that the superconductivity could be a thin film residing at the interfaces between the bulk materials. Besides imaging additional samples, which was not possible due to time constraints, certain areas of the ohmic contact where these compounds are more like to exist need to be carefully scrutinised. Lastly, it would also be of interest to investigate ohmic contacts of different sizes and in greater numbers. If some sort of percolating network is behind the superconductivity then when investigating a larger number of contacts some of them might not go superconducting. Ultimately, it is also possible that Au_7Ga_2 is actually a superconductor, but that nobody has observed/reported it, however unlikely this is.

An additional result of the work done was the questionable health of the 2DEG below the ohmic contact. This region was found to have a very inhomogeneous interface with the ohmic contact and very little Al was found left below. It is possible that more or less no 2DEG exists below the bulk of the 2DEG and that all the conduction occurs along the edge of the ohmic contact, however further measurements are required for a conclusive result. It is also important that any future TEM measurements minimise the exposure to air in order to reduce oxidation.

Chapter 8

Conclusions and further work

8.1 Introduction

This thesis has described the magnetohydrodynamics measurements performed in both narrow and wide GaAs/AlGaAs-based Hall bars, the study of AuNiGe based ohmic contacts based on different ohmic recipes, and the required background information in order to put the measurements into context. The aim of the final chapter is to briefly summarise the main findings and to comment on the potential future work, which has been divided into two main sections.

8.2 Summary of results

Chapters 2, 3, and 4 all provide the background information needed to carry out the research. Chapter 5 explains and develops a methodology for processing Johnson noise measurements seen in later chapters.

In Chapter 6, differential resistance measurements were performed on 10 μm wide narrow Hall bars at 4.2 K with the initial aim of trying to distinguish between suspended and non-suspended structures. From the initial results it was found that the interaction of the various length scales, the width of the Hall bar, the e-e scattering length, and the e-ph scattering length, resulted in a region of negative differential resistance in agreement with the literature [48]. Upon the application of a magnetic field another length scale was introduced: the cyclotron radius. At sufficiently strong magnetic fields the cyclotron radius became the shortest length scale, suppressing the interplay previously seen between the pseudo-ballistic and e-e scattering events. When performing differential resistance measurements with a constant magnetic field it was found that the previous results were replaced by an initial rapid increase in resistance as a function of the applied DC current I_{DC}, which slowed down significantly at higher I_{DC}. These results are consistent with the Bloch-Grüneisen transition [115, 116]. However this transition has never previously been observed in such narrow Hall bars. To better compare the results, similar differential resistance measurements were taken on 80 μm wide Hall bars with similar density n and mobility μ, where the same transition was observed. Previously it has been reported that, by applying a magnetic field to a narrow Hall bar, the bulk resistance, i.e., the resistance of an infinite width Hall bar, is recovered [38]. However, these results seem to imply that not only is the bulk resistance recovered, but additional properties are recovered. To confirm these findings, cross-correlated Johnson noise thermometry techniques [118] were used in order to measure the electron temperature T_e at a given I_{DC}, finding good agreement between the measured T_e and the observed transition.

Finally, some measurements were repeated on a narrow Hall bar using a fridge going down to 0.6 K; the results were consistent with those at 4.2 K. By extrapolating the data at these lower temperatures, it was found that the transition observed would disappear between 7.8 and 9.7 K, which is in good agreement with the Bloch-Grüneisen temperature of 9.12 K.

Chapter 7 presented a transmission electron microscopy study performed on two different types of AuNiGe based ohmic contacts on top of GaAs/AlGaAs two-dimensional electron gases (2DEG). Both the layered eutectic and eutectic slug sample have been shown to go superconducting at 1 K [1, 66], which has a negative impact on the ability to cool the samples below these temperatures. Initially, the elemental composition was measured using energy-dispersive X-ray spectroscopy of the various regions inside the ohmic contact. Three major regions were found; an AuGaAl-rich region ubiquitous throughout the ohmic contact, NiGeAs-rich inclusions spread throughout, and a pure Ge region near the bottom of the ohmic contact. It was also found that a significant amount of the Al required to create the 2DEG had been removed from the semiconductor below the ohmic contact. Originally, the depth of the Al layer was 80 nm and a step of 70 nm was found in the eutectic slug sample. The layered eutectic sample fared even worse and had 100+ nm deep trenches dug into the semiconductor. These observations raised serious questions about the health and existence of the 2DEG below the bulk of the ohmic contact. Secondly, a TEM structural analysis was performed. All regions had crystalline structure, but only part of the main AuGaAl phase was identified to be Au_7Ga_2 with a very small amount of Al spread throughout. The NiGeAs region was identified as Ni_2GeAs, as this matches the elemental composition; likewise the Ge-rich region was likely crystalline Ge. The main candidates for superconductivity could be an AuGe phase between the AuGaAl phase and the Ge-rich region, a thin layer of pure Al near the top of the ohmic contact, or α-Ga which was previously found in AuNiGe-based ohmic contacts [148].

8.3 Future work

In Chapter 6 only two suspended and non-suspended samples were studied, which is a limited sample size. Ideally more Hall bars should be investigated, going to even lower temperatures. Additionally studying samples of different widths would also be useful in order to study the impact of the width. Only 10 and 80 μm-wide samples were studied, and while the results could broadly be explained in terms of the relevant length scales, more widths would make for a stronger argument, especially with respect to the flat differential resistivity observed. Ultimately, no concrete difference was found between suspended and non-suspended Hall bars, but there were some potential leads which could be developed further, especially at lower temperatures.

There is a lot of future work with respect to the results from Chapter 7. A list of potential superconducting candidates was established and a much more granular study is now required in order to narrow the list down further. The main phase found throughout the ohmic contact, Au_7Ga_2, is not a superconductor and there are no major phases found which could be. As a result a lot more time is required in order to study much smaller parts of the ohmic contact in order to eliminate the possible candidates. However, the work presented here has been able to identify the areas which need to be scrutinised further. One region of interest is the region transitioning from the Ge region to the AuGaAl region, as there could be an AuGe superconductor present. The second region of interest is the very top of the ohmic contact, which found higher concentrations of Al. If the concentration near the top is sufficiently high then crystalline Al or Au_4Al could form. Another factor to keep in mind is oxidation. Originally, two sets of studies were done on the ohmic contacts, one several months after the other. In the second study the Al content was found to have dropped dramatically due to oxidation, and as a result the Al results presented in this thesis were purely based on the first study. There was, however, a period of a few days after the TEM sample was made before it was first studied and it is unknown how much this could have affected the Al content. Any future work performed on these types of ohmic contacts would ideally completely eliminate any contact with oxygen, but if that is not possible then the contact period should be minimised.

Bibliography

[1] Levitin LV, van der Vliet H, Theisen T, Dimitriadis S, Lucas M, Corcoles AD, et al. Cooling low-dimensional electron systems into the microkelvin regime. Nature Communications. 2022;13(1):1-8.

[2] Scherer H, Schumacher HW. Single-Electron Pumps and Quantum Current Metrology in the Revised SI. Annalen der Physik. 2019;531(5):1800371.

[3] Cronenwett SM, Oosterkamp TH, Kouwenhoven LP. A tunable Kondo effect in quantum dots. Science. 1998;281(5376):540-4.

[4] Jompol Y, Ford C, Griffiths J, Farrer I, Jones G, Anderson D, et al. Probing spin-charge separation in a Tomonaga-Luttinger liquid. Science. 2009;325(5940):597-601.

[5] Naumov V. Electron heat capacity and moments of the phonon density of states for metals and superconductors. Physical Review B. 1994;49(18):13247.

[6] Appleyard N, Nicholls J, Pepper M, Tribe W, Simmons M, Ritchie D. Direction-resolved transport and possible many-body effects in one-dimensional thermopower. Physical Review B. 2000;62(24):R16275.

[7] Jones A, Scheller C, Prance J, Kalyoncu Y, Zumbühl D, Haley R. Progress in cooling nanoelectronic devices to ultra-low temperatures. Journal of Low Temperature Physics. 2020;201:772-802.

[8] Jucknischke D, Buhlmann HJ, Ilegems M, Jeckelmann B, Schwitz W. Properties of alloyed AuGeNi-contacts on GaAs/GaAlAs-heterostructures. In: Conference on Precision Electromagnetic Measurements; 1990. p. 336-7.

[9] Shih YC, Wilkie E, Murakami M. Transmission electron microscopy studies of the microstructure of AuNiGe ohmic contact to n-type GaAs. American Vacuum Society. 1987.

[10] Murakami M, Shih YC, Price W, Wilkie E, Childs K, Parks C. Thermally stable ohmic contacts to n-type GaAs. III. GeInW and NiInW contact metals. Journal of Applied Physics. 1988;64(4):1974-82.

[11] Kittel C. Introduction to solid state physics Eighth edition; 2021.

[12] Ziman JM. Electrons and phonons: the theory of transport phenomena in solids. Oxford university press; 2001.

[13] Basko D, Aleiner I, Altshuler B. Possible experimental manifestations of the many-body localization. Physical Review B. 2007;76(5):052203.

[14] McArdle G, Lerner IV. Electron-phonon decoupling in two dimensions. Scientific Reports. 2021;11(1):1-8.

[15] Altshuler BL, Kravtsov VE, Lerner IV, Aleiner IL. Jumps in current-voltage characteristics in disordered films. Physical Review Letters. 2009;102(17):176803.

[16] Ovadia M, Sacépé B, Shahar D. Electron-phonon decoupling in disordered insulators. Physical Review Letters. 2009;102(17):176802.

[17] Ovadia M, Kalok D, Tamir I, Mitra S, Sacépé B, Shahar D. Evidence for a finite-temperature insulator. Scientific Reports. 2015;5(1):1-6.

[18] Chen C, Holmes S, Farrer I, Beere H, Ritchie D. Suspended two-dimensional electron gases in $In_{0.75}Ga_{0.25}As$ quantum wells. Applied Physics Letters. 2020;116(23):232106.

[19] Blick RH, Roukes M, Wegscheider W, Bichler M. Freely suspended two-dimensional electron gases. Physica B: Condensed Matter. 1998;249:784-7.

[20] Schmidt M, Schneider G, Heyn C, Stemmann A, Hansen W. Thermopower of a 2D electron gas in suspended AlGaAs/GaAs heterostructures. Journal of Electronic Materials. 2012;41(6):1286-9.

[21] Shevyrin A, Pogosov A, Budantsev M, Bakarov A, Toropov A, Ishutkin S, et al. The role of Euler buckling instability in the fabrication of nanoelectromechanical systems on the basis of GaAs/AlGaAs heterostructures. Applied Physics Letters. 2012;101(24):241916.

[22] Bockelmann U, Bastard G. Phonon scattering and energy relaxation in two-, one-, and zero-dimensional electron gases. Physical Review B. 1990;42(14):8947.

[23] Gupta A, Heremans J, Kataria G, Chandra M, Fallahi S, Gardner G, et al. Hydrodynamic and ballistic transport over large length scales in GaAs/AlGaAs. Physical Review Letters. 2021;126(7):076803.

[24] Samaraweera RL, Liu HC, Gunawardana B, Kriisa A, Reichl C, Wegscheider W, et al. Coherent backscattering in quasi-ballistic ultra-high mobility GaAs/AlGaAs 2DES. Scientific Reports. 2018;8(1):10061.

[25] Takagaki Y, Gamo K, Namba S, Ishida S, Takaoka S, Murase K, et al. Nonlocal quantum transport in narrow multibranched electron wave guide of GaAs-AlGaAs. Solid State Communications. 1988;68(12):1051-4.

[26] Shinohara M, Yokoyama H, Inoue N. Effects of interface flatness and abruptness on optical and electrical characteristics of GaAs/AlGaAs quantum structures grown by metalorganic vapor phase epitaxy. Journal of Vacuum Science & Technology B: Microelectronics and Nanometer Structures Processing, Measurement, and Phenomena. 1995;13(4):1773-9.

[27] Cho AY, Arthur J. Molecular beam epitaxy. Progress in Solid State Chemistry. 1975;10:157-91.

[28] Manfra MJ. Molecular beam epitaxy of ultra-high-quality AlGaAs/GaAs heterostructures: enabling physics in low-dimensional electronic systems. Annu Rev Condens Matter Phys. 2014;5(1):347-73.

[29] Kelly MJ. 5. In: Low-dimensional semiconductors: materials, physics, technology, devices. vol. 3. Clarendon Press; 1995. p. 104-6.

[30] Kopf R, Herman M, Schnoes ML, Perley A, Livescu G, Ohring M. Band offset determination in analog graded parabolic and triangular quantum wells of GaAs/AlGaAs and GaInAs/AlInAs. Journal of Applied Physics. 1992;71(10):5004-11.

[31] Gehrsitz S, Sigg H, Herres N, Bachem K, Köhler K, Reinhart F. Compositional dependence of the elastic constants and the lattice parameter of $Al_xGa_{1-x}As$. Physical Review B. 1999;60(16):11601.

[32] Yamada M, Ogita S, Yamagishi M, Tabata K. Anistropy and broadening of optical gain in a GaAs/AlGaAs multiquantum-well laser. IEEE journal of Quantum Electronics. 1985;21(6):640-5.

[33] Ochalski T, Żuk J, Regiński K, Bugajski M. Photoreflectance studies of InGaAs/GaAs/AlGaAs single quantum well laser structures. Acta Physica Polonica A. 1998;94(3):463-7.

[34] Mizuta M, Tachikawa M, Kukimoto H, Minomura S. Direct evidence for the DX center being a substitutional donor in AlGaAs alloy system. Japanese Journal of Applied Physics. 1985;24:L143-6.

[35] Yamagiwa M, Sumita N, Minami F, Koguchi N. Confined electronic structure in GaAs quantum dots. Journal of Luminescence. 2004;108(1-4):379-83.

[36] Drummond T, Kopp W, Fischer R, Morkoç H, Thorne R, Cho A. Photoconductivity effects in extremely high mobility modulation-doped (Al, Ga) As/GaAs heterostructures. Journal of Applied Physics. 1982;53(2):1238-40.

[37] Smith C. Low-dimensional quantum devices. Reports on Progress in Physics. 1996;59(2):235.

[38] Thornton T. Ballistic transport in GaAs quantum wires—A short history. Superlattices and Microstructures. 1998;23(3-4):601-10.

[39] Kawamura T, Sarma SD. Phonon-scattering-limited electron mobilities in $Al_xGa_{1-x}As$/GaAs heterojunctions. Physical Review B. 1992;45(7):3612.

[40] Kaasbjerg K, Thygesen KS, Jauho AP. Acoustic phonon limited mobility in two-dimensional semiconductors: Deformation potential and piezoelectric scattering in monolayer MoS_2 from first principles. Physical Review B. 2013;87(23):235312.

[41] Shah J, Leite R. Radiative recombination from photoexcited hot carriers in GaAs. Physical Review Letters. 1969;22(24):1304.

[42] Molenkamp L, De Jong M. Electron-electron scattering induced size effects in a two-dimensional wire. Physical Review B. 1994;49(7):5038.

[43] Giuliani GF, Quinn JJ. Lifetime of a quasiparticle in a two-dimensional electron gas. Physical Review B. 1982;26(8):4421.

[44] Murphy S, Eisenstein J, Pfeiffer L, West K. Lifetime of two-dimensional electrons measured by tunneling spectroscopy. Physical Review B. 1995;52(20):14825.

[45] Turner N, Nicholls J, Linfield E, Brown K, Jones G, Ritchie D. Tunneling between parallel two-dimensional electron gases. Physical Review B. 1996;54(15):10614.

[46] Zheng L, Sarma SD. Coulomb scattering lifetime of a two-dimensional electron gas. Physical Review B. 1996;53(15):9964.

[47] Gurzhi R. Minimum of resistance in impurity-free conductors. Sov Phys JETP. 1963;44:771.

[48] De Jong M, Molenkamp L. Hydrodynamic electron flow in high-mobility wires. Physical Review B. 1995;51(19):13389.

[49] Chabasseur-Molyneux V, Dzurak A, Kozorezov A, Wigmore J, Ritchie D, Churchill A, et al. Observation of the effect of electron-electron scattering on the impurity-limited resistivity of a two-dimensional electron gas. Physical Review B. 1995;51(19):13793.

[50] Thornton T, Roukes M, Scherer A, Van de Gaag B. Boundary scattering in quantum wires. Physical Review Letters. 1989;63(19):2128.

[51] Alekseev P. Negative magnetoresistance in viscous flow of two-dimensional electrons. Physical Review Letters. 2016;117(16):166601.

[52] Scaffidi T, Nandi N, Schmidt B, Mackenzie AP, Moore JE. Hydrodynamic electron flow and Hall viscosity. Physical Review Letters. 2017;118(22):226601.

[53] Gusev G, Levin A, Levinson E, Bakarov A. Viscous electron flow in mesoscopic two-dimensional electron gas. AIP Advances. 2018;8(2):025318.

[54] Gusev G, Jaroshevich A, Levin A, Kvon Z, Bakarov A. Stokes flow around an obstacle in viscous two-dimensional electron liquid. Scientific Reports. 2020;10(1):1-9.

[55] Keser AC, Wang DQ, Klochan O, Ho DY, Tkachenko OA, Tkachenko VA, et al. Geometric control of universal hydrodynamic flow in a two-dimensional electron fluid. Physical Review X. 2021;11(3):031030.

[56] Ahn S, Sarma SD. Hydrodynamics, viscous electron fluid, and Wiedeman-Franz law in two-dimensional semiconductors. Physical Review B. 2022;106(8):L081303.

[57] Braslau N, Gunn JB, Staples J. Metal-semiconductor contacts for GaAs bulk effect devices. Solid-State Electronics. 1967;10(5):381-3.

[58] Gunn J. Solid State Comm. 1, 88 (1963). IBM J Res and Develop. 1964;8:141.

[59] Auvray P, Guivarc'h A, L'haridon H, Mercier J, Henoc P. Formation, microstructure et résistances des contacts Au Ge/n-GaAs, Au Ge/n-InP, Au Zn/p-InP et Au Be/p-InP. Thin Solid Films. 1985;127(1-2):39-68.

[60] Heiblum M, Nathan MI, Chang CA. Characteristics of AuGeNi ohmic contacts to GaAs. Solid-State Electronics. 1982;25(3):185-95.

[61] Kuan T, Batson P, Jackson TN, Rupprecht H, Wilkie E. Electron microscope studies of an alloyed Au/Ni/Au-Ge ohmic contact to GaAs. Journal of Applied Physics. 1983;54(12):6952-7.

[62] Murakami M, Childs K, Baker JM, Callegari A. Microstructure studies of AuNiGe Ohmic contacts to n-type GaAs. Journal of Vacuum Science & Technology B: Microelectronics Processing and Phenomena. 1986;4(4):903-11.

[63] Lumpkin NE, Lumpkin GR, Blackford MG. The Role of Ni in the Formation of Low Resistance Ni–Ge–Au Ohmic Contacts to n+ GaAs Heterostructures. Journal of Materials Research. 1999;14(4):1261-71.

[64] Baranska A, Szerling A, Karbownik P, Hejduk K, Bugajski M, Laszcz A, et al. Ohmic contacts for room-temperature AlGaAs/GaAs quantum cascade lasers (QCL). Optica Applicata. 2013;43(1).

[65] Christou A, Papanicolaou N. Redistribution of aluminum in MODFET ohmic contacts. Solid-state electronics. 1986;29(2):189-92.

[66] Beauchamp CB, Dimitriadis S, Nicholls J, Levitin L, Casey A, See P, et al. Superconductivity in AuNiGe ohmic contacts to a GaAs-based high mobility two-dimensional electron gas. Applied Physics Letters. 2020;117(16):162104.

[67] Reyntjens S, Puers R. A review of focused ion beam applications in microsystem technology. Journal of Micromechanics and Microengineering. 2001;11(4):287.

[68] Munroe PR. The application of focused ion beam microscopy in the material sciences. Materials Characterization. 2009;60(1):2-13.

[69] Tao T, Wilkinson W, Melngailis J. Focused ion beam induced deposition of platinum for repair processes. Journal of Vacuum Science & Technology B: Microelectronics and Nanometer Structures Processing, Measurement, and Phenomena. 1991;9(1):162-4.

[70] Giannuzzi LA, Stevie FA. A review of focused ion beam milling techniques for TEM specimen preparation. Micron. 1999;30(3):197-204.

[71] Vernon-Parry K. Scanning electron microscopy: an introduction. III-Vs Review. 2000;13(4):40-4.

[72] Klein T, Buhr E, Frase CG. TSEM: A review of scanning electron microscopy in transmission mode and its applications. Advances in Imaging and Electron Physics. 2012;171:297-356.

[73] Von Heimendahl M, Bell W, Thomas G. Applications of Kikuchi line analyses in electron microscopy. Journal of Applied Physics. 1964;35(12):3614-6.

[74] Joy DC, Pawley JB. High-resolution scanning electron microscopy. Ultramicroscopy. 1992;47(1-3):80-100.

[75] Hodoroaba VD. Energy-dispersive X-ray spectroscopy (EDS). In: Characterization of Nanoparticles. Elsevier; 2020. p. 397-417.

[76] Goodhew PJ, Humphreys J, Beanland R. In: Electron Microscopy and Analysis. 3rd ed. CRC Press; 2000. p. 169-82.

[77] Sahin Y, Karabulut A, Budak G. A practical method for the analysis of overlapped peaks in energy dispersive X-ray spectra. Applied Spectroscopy Reviews. 1996;31(3):333-45.

[78] Schagrin ML. Resistance to Ohm's law. American Journal of Physics. 1963;31(7):536-47.

[79] de Picciotto R, Stormer H, Pfeiffer L, Baldwin K, West K. Four-terminal resistance of a ballistic quantum wire. Nature. 2001;411(6833):51-4.

[80] NI. PXI-5922 Specifications;. Available from: https://www.ni.com/docs/en-US/bundle/pxi-5922-specs/page/specs.html.

[81] NF. Model LI-75A;. Available from: https://collab.phys.unsw.edu.au:4431/pub/QED/Li75A/LI-7576PS70A.pdf.

[82] NF. Multi-channel Low Noise Amplifier;. Available from: https://www.nfcorp.co.jp/english/special/low_noise/multi_amp/index.html.

[83] McMahon H, Gifford W. A New Low-Temperature Gas Expansion Cycle: Part I. In: Advances in Cryogenic Engineering: Proceedings of the 1959 Cryogenic Engineering Conference University of California, Berkeley, California September 2–4, 1959. Springer; 1960. p. 354-67.

[84] De Klerk D. Adiabatic demagnetization. Low Temperature Physics I/Kältephysik I. 1956:376-547.

[85] Courts S, Krause J. A commercial ruthenium oxide thermometer for use to 20 milliKelvin. In: AIP Conference Proceedings. vol. 985. American Institute of Physics; 2008. p. 947-54.

[86] Myers SA, Li H, Csáthy GA. A ruthenium oxide thermometer for dilution refrigerators operating down to 5 mK. Cryogenics. 2021;119:103367.

[87] Barone C, Galdi A, Pagano S, Quaranta O, Méchin L, Routoure JM, et al. Experimental technique for reducing contact and background noise in voltage spectral density measurements. Review of Scientific Instruments. 2007;78(9):093905.

[88] Barone C, Romeo F, Pagano S, Attanasio C, Carapella G, Cirillo C, et al. Nonequilibrium fluctuations as a distinctive feature of weak localization. Scientific Reports. 2015;5(1):10705.

[89] Konczakowska A, Wilamowski BM. Noise in semiconductor devices. In: Fundamentals of Industrial Electronics. CRC Press; 2018. p. 11-1.

[90] Raychaudhuri A. Measurement of 1/f noise and its application in materials science. Current Opinion in Solid State and Materials Science. 2002;6(1):67-85.

[91] Van der Ziel A. Flicker noise in electronic devices. In: Advances in electronics and electron physics. vol. 49. Elsevier; 1979. p. 225-97.

[92] Zimmerman NM, Scofield JH, Mantese JV, Webb WW. Volume versus surface origin of 1/f noise in metals. Physical Review B. 1986;34(2):773.

[93] Qu J, Benz S, Rogalla H, Tew W, White D, Zhou K. Johnson noise thermometry. Measurement Science and Technology. 2019;30(11):112001.

[94] Abbott D, Davis BR, Phillips NJ, Eshraghian K. Simple derivation of the thermal noise formula using window-limited Fourier transforms and other conundrums. IEEE Transactions on Education. 1996;39(1):1-13.

[95] Kobayashi K, Hashisaka M. Shot noise in mesoscopic systems: From single particles to quantum liquids. Journal of the Physical Society of Japan. 2021;90(10):102001.

[96] Lee P. Low noise amplifier selection guide for optimal noise performance. Analog Devices Application Note, AN-940. 2009.

[97] Blanter YM, Büttiker M. Shot noise in mesoscopic conductors. Physics Reports. 2000;336(1-2):1-166.

[98] Cochran WT, Cooley JW, Favin DL, Helms HD, Kaenel RA, Lang WW, et al. What is the fast Fourier transform? Proceedings of the IEEE. 1967;55(10):1664-74.

[99] Laroche J. Autocorrelation method for high-quality time/pitch-scaling. In: Proceedings of IEEE Workshop on Applications of Signal Processing to Audio and Acoustics. IEEE; 1993. p. 131-4.

[100] Stoica P, Moses RL, et al. Spectral analysis of signals. vol. 452. Pearson Prentice Hall Upper Saddle River, NJ; 2005.

[101] Rayleigh L. LIII. On the character of the complete radiation at a given temperature. The London, Edinburgh, and Dublin Philosophical Magazine and Journal of Science. 1889;27(169):460-9.

[102] Cohen L. The generalization of the Wiener-Khinchin theorem. In: Proceedings of the 1998 IEEE International Conference on Acoustics, Speech and Signal Processing, ICASSP'98 (Cat. No. 98CH36181). vol. 3. IEEE; 1998. p. 1577-80.

[103] Zucker S. Cross-correlation and maximum-likelihood analysis: a new approach to combining cross-correlation functions. Monthly Notices of the Royal Astronomical Society. 2003;342(4):1291-8.

[104] Tristram M, Macías-Pérez J, Renault C, Santos D. XSPECT, estimation of the angular power spectrum by computing cross-power spectra with analytical error bars. Monthly Notices of the Royal Astronomical Society. 2005;358(3):833-42.

[105] Solomon Jr OM. PSD computations using Welch's method. NASA STI/Recon Technical Report N. 1991;92:23584.

[106] Rahi PK, Mehra R, et al. Analysis of power spectrum estimation using welch method for various window techniques. International Journal of Emerging Technologies and Engineering. 2014;2(6):106-9.

[107] Rossler C, Bichler M, Schuh D, Wegscheider W, Ludwig S. Laterally defined freely suspended quantum dots in GaAs/AlGaAs heterostructures. Nanotechnology. 2008;19(16):165201.

[108] Stanisic Z. Method for static and dynamic resistance measurements of HV circuit breaker. In: 2011 2nd IEEE PES International Conference and Exhibition on Innovative Smart Grid Technologies. IEEE; 2011. p. 1-5.

[109] Lin Z, Zhigilei LV, Celli V. Electron-phonon coupling and electron heat capacity of metals under conditions of strong electron-phonon nonequilibrium. Physical Review B. 2008;77(7):075133.

[110] Gurzhi R, Kalinenko A, Kopeliovich A. Electron-electron collisions and a new hydrodynamic effect in two-dimensional electron gas. Physical Review Letters. 1995;74(19):3872.

[111] Kato M, Sakairi M, Endo A, Katsumoto S, Iye Y. Electron-electron scattering in two-dimensional electron gas under a controllable spatially modulated magnetic field. Physica E: Low-dimensional Systems and Nanostructures. 2000;6(1-4):735-7.

[112] McArdle G, Lerner IV. Electron-phonon decoupling in two dimensions. Scientific Reports. 2021;11(1):24293.

[113] Crook R, Smith C, Simmons M, Ritchie D. Imaging cyclotron orbits and scattering sites in a high-mobility two-dimensional electron gas. Physical Review B. 2000;62(8):5174.

[114] Takagaki Y, Kosugi T, Gamo K, Namba S, Murase K. Effect of low-temperature photoconduction on the depletion width in GaAs-AlGaAs wire. Semiconductor Science and Technology. 1990;5(6):634.

[115] Raichev O, Hatke A, Zudov M, Reno J. Bloch-Grüneisen nonlinearity of electron transport in GaAs/AlGaAs heterostructures. Physical Review B. 2017;96(8):081407.

[116] Stormer H, Pfeiffer L, Baldwin K, West K. Observation of a Bloch-Grüneisen regime in two-dimensional electron transport. Physical Review B. 1990;41(2):1278.

[117] Kumar A, Saminadayar L, Glattli D, Jin Y, Etienne B. Experimental test of the quantum shot noise reduction theory. Physical Review Letters. 1996;76(15):2778.

[118] Sampietro M, Fasoli L, Ferrari G. Spectrum analyzer with noise reduction by cross-correlation technique on two channels. Review of Scientific Instruments. 1999;70(5):2520-5.

[119] Schmidt M, Schneider G, Heyn C, Stemmann A, Hansen W. Thermopower of a 2D electron gas in suspended AlGaAs/GaAs heterostructures. Journal of Electronic Materials. 2012;41(6):1286-9.

[120] Blakemore J. Semiconducting and other major properties of gallium arsenide. Journal of Applied Physics. 1982;53(10):R123-81.

[121] Kelly MJ. In: Low-dimensional semiconductors: materials, physics, technology, devices. vol. 3. Clarendon Press; 1995. p. 16.

[122] Lin B, Tsui D, Weimann G. Mobility transition in the two-dimensional electron gas in GaAs-AlGaAs heterostructures. Solid State Communications. 1985;56(3):287-90.

[123] Pipa V, Vagidov N, Mitin V, Stroscio M. Momentum relaxation of 2D electron gas due to near-surface acoustic phonon scattering. Physica B: Condensed Matter. 1999;270(3-4):280-8.

[124] Mendez E, Price P, Heiblum M. Temperature dependence of the electron mobility in GaAs-GaAlAs heterostructures. Applied Physics Letters. 1984;45(3):294-6.

[125] Kalra R, Laucht A, Dehollain JP, Bar D, Freer S, Simmons S, et al. Vibration-induced electrical noise in a cryogen-free dilution refrigerator: Characterization, mitigation, and impact on qubit coherence. Review of Scientific Instruments. 2016;87(7):073905.

[126] Kurdak C, Tsui D, Parihar S, Lyon S, Shayegan M. Electron temperature in low-dimensional wires using thermal noise measurements. Applied Physics Letters. 1995;67(3):386-8.

[127] Sampietro N, Accomando G, Fasoli LG, Ferrari G, Gatti EC. High sensitivity noise measurement with a correlation spectrum analyzer. IEEE Transactions on Instrumentation and Measurement. 2000;49(4):820-2.

[128] Eckhause T, Süzer Ö, Kurdak C, Yun F, Morkoç H. Electric-field-induced heating and energy relaxation in GaN. Applied Physics Letters. 2003;82(18):3035-7.

[129] Davisson CJ, Germer LH. Reflection and Refraction of Electrons by a Crystal of Nickel. Proceedings of the National Academy of Sciences. 1928;14(8):619-27.

[130] Muller DA. Structure and bonding at the atomic scale by scanning transmission electron microscopy. Nature Materials. 2009;8(4):263-70.

[131] Murray J, Okamoto H, Massalski T. The Al- Au (aluminum-gold) system. Bulletin of Alloy Phase Diagrams. 1987;8(1):20-30.

[132] Essam JW. Percolation theory. Reports on Progress in Physics. 1980;43(7):833.

[133] Saberi AA. Recent advances in percolation theory and its applications. Physics Reports. 2015;578:1-32.

[134] Cherney OAE, Shewchun J. Enhancement of superconductivity in thin aluminium films. Canadian Journal of Physics. 1969;47(10):1101-6.

[135] Lamoise A, Chaumont J, Meunier F, Bernas H. Superconducting properties of aluminium thin films after ion implantation at liquid helium temperatures. Journal de Physique Lettres. 1975;36(11):271-3.

[136] Esfahani MMD, Oganov AR, Niu H, Zhang J. Superconductivity and unexpected chemistry of germanium hydrides under pressure. Physical Review B. 2017;95(13):134506.

[137] Oya Gi, Saur E. Preparation of Nb_3Ge films by chemical transport reaction and their critical properties. Journal of Low Temperature Physics. 1979;34(5):569-83.

[138] Herrmannsdörfer T, Skrotzki R, Heera V, Ignatchik O, Uhlarz M, Mücklich A, et al. Superconductivity in thin-film germanium in the temperature regime around 1 K. Superconductor Science and Technology. 2010;23(3):034007.

[139] Luo H, Merriam M, Hamilton D. Superconducting metastable compounds. Science. 1964;145(3632):581-3.

[140] Granqvist C, Claeson T. The superconducting energy gap measured by tunneling into quench-condensed germanium-gold. Physics Letters A. 1972;39(4):271-2.

[141] Seguchi Y, Tsuboi T, Suzuki T. Magnetic-Field-Enhanced Superconductivity in Alloy Films of Au–Ge. Journal of the Physical Society of Japan. 1993;62(8):2564-7.

[142] Wan Z, Kazakov A, Manfra MJ, Pfeiffer LN, West KW, Rokhinson LP. Induced superconductivity in high-mobility two-dimensional electron gas in gallium arsenide heterostructures. Nature Communications. 2015;6(1):1-5.

[143] Ball R. Improvements in the topography of AuGeNi-based ohmic contacts to n-GaAs. Thin Solid Films. 1989;176(1):55-68.

[144] Goronkin H, Tehrani S, Remmel T, Fejes PL, Johnston K. Ohmic contact penetration and encroachment in GaAs/AlGaAs and GaAs FETs. IEEE Transactions on Electron Devices. 1989;36(2):281-8.

[145] Elliott RP, Shunk FA. The Au- Ga (Gold-Gallium) system. Bulletin of Alloy Phase Diagrams. 1981;2(3):356-8.

[146] Khan HR. Superconducting gold alloys. Gold Bulletin. 1984;17(3):94-100.

[147] Hoyt R, Mota A. Superconductivity in α-phase alloys of Cu, Ag and Au. Solid State Communications. 1976;18(1):139-42.

[148] Madams C, Morgan D, Howes M. Outmigration of gallium from Au-GaAs interfaces. Electronics Letters. 1975;24(11):574-5.

[149] Chen B, Duan X, Wang H, Du J, Zhou Y, Xu C, et al. Large magnetoresistance and superconductivity in α-gallium single crystals. npj Quantum Materials. 2018;3(1):1-8.

[150] Charnaya E, Tien C, Lin K, Wur C, Kumzerov YA. Superconductivity of gallium in various confined geometries. Physical Review B. 1998;58(1):467.

[151] Palade P, Wagner F, Jianu A, Filoti G. Electronic properties of gold–aluminium intermetallic compounds. Journal of Alloys and Compounds. 2003;353(1-2):23-32.

[152] Philofsky E. Intermetallic formation in gold-aluminum systems. Solid-State Electronics. 1970;13(10):1391-4.

[153] Hamilton D, Raub CJ, Matthias B, Corenzwit E, Hull Jr G. Some new superconducting compounds. Journal of Physics and Chemistry of Solids. 1965;26(3):665-7.

[154] Cochran JF, Mapother D. Superconducting transition in aluminum. Physical Review. 1958;111(1):132.

[155] Lee JL, Kim YT, Yoo HM, Lee GY. Au/Ge-based ohmic contact to an AlGaAs/InGaAs pseudomorphic high electron mobility transistor with an undoped cap layer. Journal of Vacuum Science & Technology B: Microelectronics and Nanometer Structures Processing, Measurement, and Phenomena. 1999;17(3):1034-9.

[156] Reinhardt F, Dwir B, Kapon E. Oxidation of GaAs/AlGaAs heterostructures studied by atomic force microscopy in air. Applied Physics Letters. 1996;68(22):3168-70.

[157] Higman T, Emanuel M, Coleman J, Jeng S, Wayman C. Structural analysis of Au-Ni-Ge and Au-Ag-Ge alloyed ohmic contacts on modulation-doped AlGaAs-GaAs heterostructures. Journal of Applied Physics. 1986;60(2):677-80.